

# Origins of the macroscopic symmetry breaking in centrosymmetric phases of perovskite oxides

THÈSE N° 8026 (2017)

PRÉSENTÉE LE 13 OCTOBRE 2017  
À LA FACULTÉ DES SCIENCES ET TECHNIQUES DE L'INGÉNIEUR  
GROUPE SCI STI DD  
PROGRAMME DOCTORAL EN SCIENCE ET GÉNIE DES MATÉRIAUX

ÉCOLE POLYTECHNIQUE FÉDÉRALE DE LAUSANNE

POUR L'OBTENTION DU GRADE DE DOCTEUR ÈS SCIENCES

PAR

Sina HASHEMI ZADEH

acceptée sur proposition du jury:

Dr L. Weber, président du jury  
Prof. D. Damjanovic, directeur de thèse  
Prof. H. Simons, rapporteur  
Dr G. Picht, rapporteur  
Prof. P. Murali, rapporteur



ÉCOLE POLYTECHNIQUE  
FÉDÉRALE DE LAUSANNE

Suisse  
2017



*“Beliefs do not change facts. Facts, if you are reasonable,  
should change your beliefs.”*

To my parents...





## Acknowledgments

Foremost, I would like to express my sincere gratitude to my thesis advisor Prof. Dragan Damjanovic for the opportunity that he gave me to join his group. I am greatly indebted to him for his continues support, for his patience and for his immense knowledge. He has inspired me since my first days at EPFL 7 years ago with his superior knowledge and moral traits, and I am extremely delighted that I can count myself as one of his students.

I am grateful to Prof. Paul Muralt, Prof. Hugh Simons, Dr. Gunnar Picht and Dr. Ludger Weber for accepting to be members of the jury of my doctoral exam. I would also like to acknowledge Prof. Francesco Stellacci and Prof. Véronique Michaud for attending my candidacy exam and annual presentations and for their constructive comments which helped to improve the quality of my work.

I am very thankful to our collaborators for their scientific contribution to my thesis: Prof. Andreja Bencan and Prof. Tadej Rojac from Jozef Stefan Institute, Dr. Goran Drazic from National Institute of Chemistry Ljubljana, Prof. Takuya Hoshina from Tokyo Institue of Technology, and Dr. Emad Oveisi from CIME EPFL.

I was delighted for working in a lab with a friendly atmosphere, among great colleagues who are always ready to share their knowledge and experience. I would like to acknowledge Prof. Paul Muralt, Prof. Nava Setter, Prof. Aleksander Tagantsev, Dr. Igor Stolichnoc and Dr. Enrico Colla for their usefull comments during seminars and group meetings. Huge thank for all the technical and administrative support that I got from, Lino, Yuko, Erika, Chrystelle and Anne. I would like to thank Alberto for his kindness and help at the earlier stage of my Ph.D. I want to acknowledge all the previous and current members of LC, DD and PM groups who I met during my work, especially Tomas, Alex, Barbara, Arnaud, Leo, Davide, Kaushik, Nachi, Petr Y, Thibaut, Yasu, Xiao, Stefan, Cosmin, Vladimir, Mahmoud and Fazel. Special thanks to Ramin and Robin for their friendship, help and having endless fruitful discussions.

My gretaest appreciation to all my amazing frineds inside and outside of EPFL for the memories that we share and the joyfull time that we spent together, Koosha, Babak, Ramin, Emad, Sohrab, Dara, Nima, Iman, Kasra, Zohreh, Maryam, Elmira, Mahmoud, Fazel, Sareh, Payam, Baharak, Mohammad, Ali and Hanif. If unknowingly I have not mentioned your name, rest assured that I greatly appreciated your assistance.

At last but not the least, my deepest gratitude goes to my parents Mahboubeh and Mohammad, and my sister Shiva for their unconditional love and continues support. I would not have made it this far without them. All I have achieved in my life is because of them.

Sina

September 2017  
Lausanne



## Abstract

Many perovskite materials experience a temperature-driven phase transition at the Curie temperature from a non-centrosymmetric polar ferroelectric phase to a paraelectric phase, where the polarization is lost. The paraelectric phase is usually centrosymmetric (often cubic) and therefore non-piezoelectric. Despite being centrosymmetric, ferroelectrics still show some forms of electro-mechanical coupling in their paraelectric phase. One is electrostriction, which relates strain and the square of polarization, and the other is flexoelectricity. Both of these properties are not symmetry limited and are practically strong in ferroelectrics. However, it has been shown that the flexoelectric coefficient of perovskite  $(\text{Ba}_{0.67}\text{Sr}_{0.33})\text{TiO}_3$  in its centrosymmetric paraelectric state at room temperature, is up to three to four orders of magnitude larger than its theoretically predicted values. Experimental data cannot be easily reconciled with theoretical predictions and such enormous discrepancy demonstrates that either the theory is unable to fully explain the flexoelectric response, or another electro-mechanical mechanism is playing a role (partially or completely) in the apparently large flexoelectric response of the material.

It has been shown that  $\text{Ba}_{0.60}\text{Sr}_{0.40}\text{TiO}_3$  with apparently large flexoelectric coefficient exhibit symmetry breaking and consequently exhibits forbidden piezoelectric- and pyroelectric-like behavior in its paraelectric phase. In this thesis work, our interest lies in describing and interpreting the conditions where breaking of the symmetry is not associated with the external field and the flexoelectricity but is proper to the material. Origins and mechanisms of the symmetry breaking were investigated in two different cases: i) local breaking of centrosymmetry; and ii) macroscopic (or bulk) symmetry breaking. The local breaking of the centrosymmetry may refer to the existence of microscopic polar entities and/or disordered displacement of ions in the unit cell. Global symmetry breaking could be associated with non-uniform distribution of charged defects and/or the coupling of polar nano-regions with the strain gradient in the sample.

We compared dielectric, elastic, and pyroelectric properties of the  $\text{Ba}_{1-x}\text{Sr}_x\text{TiO}_3$  (BST) family, pure  $\text{BaTiO}_3$  in perovskite (p-BTO) and hexagonal (h-BTO) forms, and  $\text{SrTiO}_3$  to study the possible governing mechanisms of symmetry breaking. In addition, the atomic structure of  $\text{Ba}_{0.6}\text{Sr}_{0.4}\text{TiO}_3$  (BST6040) was studied by high resolution scanning transmission electron microscopy (STEM) to look for direct evidence of polar regions and understand their exact nature and origin.

According to experimental data, the paraelectric phase of p-BTO shows local and global breaking of nominal centrosymmetry and possesses microscopic and macroscopic polarizations. These polarizations are likely associated with polar regions (precursors of the ferroelectric phase) ordered by strain gradient in the sample. On the other hand, h-BTO does not exhibit the macroscopic pyroelectric response at room temperature due to the non-polar nature of paraelectric-ferroelastic precursors. However, TSC measurements have shown that the macroscopic centric symmetry is also broken in h-BTO.

Presence of the macroscopic symmetry breaking in other compositions such as  $\text{Pb}(\text{Mg}_{1/3}\text{Nb}_{2/3})\text{O}_3$  ceramics, single crystals of  $\text{K}(\text{Ta,Nb})\text{O}_3$  and also BST samples prepared with very different techniques indicate that the symmetry breaking in the paraelectric phase of ferroelectrics is not only limited to one specific material or preparation procedure and is generally encountered in perovskite materials and broader.

Suppression of the pyroelectric response in BST6040 doped samples with higher concentration of charged defects supports the idea that point defects are not the principal entities responsible for symmetry breaking. If it was the case we should have larger response for aliovalently doped and nonstoichiometric samples. The most likely origin of the global symmetry breaking is thus the alignment of polar regions.

Studying the material response to dynamic electric field could provide significant information on the nature of polar entities and could clarify the mechanisms governing the dynamics of polar regions. It was believed that polar nano regions in relaxor ferroelectric materials contribute to dielectric nonlinearity and show dynamics similar to that observed by domain walls in ferroelectrics. Our results showed that Rayleigh-like relation, which describes dynamics of domain walls in a random pinning environment, cannot describe the dynamics of polar entities in these materials.

High resolution atomic studies were carried out to search for the direct evidence of polar entities in the paraelectric phase of BST6040. Our images showed distinct static clusters with the average size of few nanometers where A-site, B-site and O ions are displaced from their ideal cubic positions. Studying Ti and O atoms displacements regarding both A- and B-site sublattices demonstrate that the gravity centers of positive ( $\text{Ti}^{+4}$ ) and negative ( $\text{O}^{2-}$ ) charges do not coincide with each other and most likely form nonzero dipole moment in the lattice. The presence of larger ionic displacement for Sr-rich regions compared to Ba-rich regions is an additional evidence to support that the local polarity does not originate only from the chemical inhomogeneity and the crystal structure of Ba-rich ferroelectric (Ba,Sr)TiO<sub>3</sub> pockets in the material.

We believe that all presented experimental data can be consistently explained by the presence of microscopic precursors of the ferroelectric state and their interaction with the strain gradient in the material.

**Keywords:** symmetry breaking, flexoelectricity, ferroelectrics, perovskite material, polar entities, polar regions

## Résumé

De nombreux pérovskites possèdent une transition de phase à la température de Curie, entre une phase polaire, ferroélectrique et non-centrosymétrique (à basse température) et une phase paraélectrique où la polarisation disparaît (à haute température). La phase paraélectrique est en général centrosymétrique (le plus souvent cubique) et par conséquent, n'est pas piézoélectrique. Cependant, malgré la symétrie centrale, les matériaux ferroélectriques conservent, dans la phase paraélectrique, certaines formes de couplage électromécanique. L'une d'elle est l'électrostriction, qui relie la déformation au carré de la polarisation, et l'autre est la flexoélectricité. Ces deux propriétés ne sont pas limitées par la symétrie du cristal, elles existent dans tous les groupes de symétrie et sont en pratique particulièrement marquées chez les matériaux ferroélectriques. Cependant, il a été démontré que le coefficient flexoélectrique du pérovskite  $(\text{Ba}_{0.67}\text{Sr}_{0.33})\text{TiO}_3$ , dans sa phase paraélectrique (qui est centrosymétrique) à température ambiante, est de 3 à 4 ordres de grandeur plus élevé que les valeurs prédites par la théorie. Les données expérimentales sont donc difficilement compatibles avec les prédictions théoriques, et une telle divergence démontre soit que la théorie actuelle n'est pas capable de décrire pleinement la réponse flexoélectrique du matériau, soit qu'un autre mécanisme provoquant un couplage électromécanique contribue, partiellement ou complètement, à la réponse flexoélectrique apparente du matériau.

Il a été démontré que le  $\text{Ba}_{1-x}\text{Sr}_x\text{TiO}_3$  possédant un grand coefficient flexoélectrique apparent possède également une brisure de symétrie, et par conséquent un comportement du type piézoélectrique et pyroélectrique dans la phase paraélectrique, ce qui est habituellement interdit. Dans ce travail de thèse, nous nous sommes intéressés à la description et à l'interprétation des conditions dans lesquelles les brisures de symétrie ne sont associées ni à des champs externes, ni à l'effet flexoélectrique, mais sont intrinsèques au matériau. Les origines et les mécanismes de brisure de symétrie ont été étudiés dans deux cas différents : i) brisure locale de la centrosymétrie ; et ii) brisure de symétrie macroscopique ou dans la masse du matériau. La brisure locale de la centrosymétrie peut faire référence à l'existence d'entités polaires microscopiques et/ou à des déplacements désordonnés d'ions par rapport à leur position d'équilibre dans la maille élémentaire. Les brisures globales de symétrie peuvent être associées avec des distributions non uniformes de défauts chargés et/ou avec un couplage entre des nano-régions polaires et le gradient de déformation au sein du matériau.

Nous avons comparé les propriétés diélectriques, élastiques et pyroélectriques des matériaux de la famille  $\text{Ba}_{1-x}\text{Sr}_x\text{TiO}_3$  (BST), du  $\text{BaTiO}_3$  pur dans ses formes pérovskite (p-BTO) et hexagonale (h-BTO) ainsi que du  $\text{SrTiO}_3$  pour étudier les mécanismes pouvant gouverner les brisures de symétrie. De plus, nous avons étudié en haute résolution la structure atomique du  $\text{Ba}_{0.6}\text{Sr}_{0.4}\text{TiO}_3$  (BST6040) par microscopie électronique à balayage en transmission, dans le but de démontrer l'existence de nano-régions polaires par observation directe, et de comprendre leur nature et leur origine exactes.

D'après nos données expérimentales, la phase paraélectrique du p-BTO possède des brisures locales et globales de la centrosymétrie nominale, ainsi qu'une polarisation microscopique et macroscopique. Ces deux types de polarisations sont vraisemblablement associés avec des régions polaires (précurseurs de la phase ferroélectrique) ordonnées par le gradient de déformation au sein de l'échantillon. Au contraire, le h-BTO ne montre aucune réponse pyroélectrique

macroscopique, ce qui est cohérent avec la présence de précurseurs non polaires, paraélectriques et ferroélastiques, à température ambiante. Cependant, des mesures de courant thermiquement stimulé ont démontré que la symétrie centrale macroscopique est aussi brisée dans le h-BTO.

La présence de brisures macroscopiques de symétrie dans d'autres compositions telles que les céramiques de  $\text{Pb}(\text{Mg}_{1/3}\text{Nb}_{2/3})\text{O}_3$ , les monocristaux de  $\text{K}(\text{Ta,Nb})\text{O}_3$ , et des échantillons de BST, tous préparés avec des techniques très différentes, indique que les brisures de symétrie dans la phase paraélectrique des matériaux ferroélectriques ne sont pas limitées à un matériau ou à une procédure de préparation en particulier, mais sont rencontrées de manière générale dans les matériaux de structure pérovskite ou autre.

La disparition de la réponse pyroélectrique dans les échantillons dopés de BST6040, qui possèdent une concentration de défauts chargés plus élevée, étaye l'idée que les défauts cristallins ponctuels ne sont pas les entités principalement responsables des brisures de symétrie. Si cela était le cas, la réponse pyroélectrique devrait être plus élevée dans les échantillons non stœchiométriques ou dopés avec des éléments aliovalents. L'origine la plus vraisemblable des brisures de symétrie globales est donc l'alignement des régions polaires selon une même direction.

L'étude de la réponse du matériau à l'application de champs électriques dynamiques pourrait fournir des informations significatives quant à la nature des entités polaires, et clarifier les mécanismes gouvernant la dynamique des régions polaires. Une opinion voudrait que ces nano-régions polaires contribuent, dans les matériaux ferroélectriques relaxors, au caractère non-linéaire de la réponse diélectrique et présentent une dynamique semblable à celle observée pour les parois de domaine des matériaux ferroélectriques. Nos résultats démontrent que les équations de Rayleigh, qui décrivent la dynamique des parois de domaine se déplaçant dans un paysage énergétique aléatoire, ne rendent pas compte de la dynamique des entités polaires dans ces matériaux.

Nous avons procédé à des études atomiques en haute résolution dans le but de vérifier, par une observation directe, l'existence d'entités polaires dans la phase paraélectrique du  $(\text{Ba,Sr})\text{TiO}_3$ . Les images ainsi obtenues montrent des groupements distincts et statiques, dont la taille moyenne est de quelques nanomètres, au sein desquels les ions des sites A et B ainsi que les ions O sont décalés par rapport à leur position d'équilibre dans un réseau cubique idéal. L'étude du décalage des atomes de Ti et d'O par rapport aux sous-réseaux des sites A et B démontre que les barycentres des charges positives ( $\text{Ti}^{+4}$ ) et négatives ( $\text{O}^{2-}$ ) ne coïncident pas, et par conséquent constituent un moment dipolaire non nul au sein du réseau cristallin. Le fait que le décalage ionique dans les zones riches en Sr est plus élevé que dans celles riches en Ba est une preuve supplémentaire au crédit de l'idée que l'état de polarisation locale ne provient pas seulement d'inhomogénéités chimiques ou de la structure cristalline des zones localement plus riches en Ba au sein du matériau.

Nous croyons que la somme des données expérimentales présentées ici peut être expliquée de manière cohérente par la présence de précurseurs microscopiques à la phase ferroélectrique et par leur interaction avec le gradient de déformation au sein du matériau.

**Mots-clés:** brisure de symétrie, flexoélectricité, matériau ferroélectrique, matériau pérovskite, entités polaires, régions polaires

## Contents

<b>Abstract .....</b>	<b>i</b>
<b>Résumé .....</b>	<b>iii</b>
<b>Chapter 1. Background, thesis objective and outline .....</b>	<b>1</b>
1.1 Introduction.....	1
1.2 Symmetry and physical properties.....	1
1.3 Piezoelectricity .....	1
1.4 Pyroelectricity .....	2
1.5 Flexoelectricity .....	3
1.6 Ferroelectricity.....	4
1.7 Symmetry breaking in paraelectric phase of ferroelectrics above $T_C$ .....	7
1.8 Context and outline .....	10
Bibliography .....	12
<b>Chapter 2. Material processing and characterization .....</b>	<b>15</b>
2.1 Introduction.....	15
2.2 Barium Titanate .....	15
2.3 Compositional modification of barium titanate .....	17
2.4 Material selection.....	18
2.5 Ceramic processing.....	19
2.6 Density measurement.....	23
2.7 X-Ray diffraction and compositional analysis .....	24
2.8 Scanning electron microscopy .....	26
2.9 Dielectric properties measurements.....	28
2.10 Summary .....	31
Bibliography .....	32
<b>Chapter 3. Experimental techniques .....</b>	<b>35</b>
3.1 Introduction.....	35
3.2 Dynamic mechanical analysis.....	35
3.3 Dielectric nonlinear harmonic analysis .....	37
3.4 Pyroelectric measurement.....	39
3.5 Thermally stimulated current measurement .....	43
Bibliography .....	46
<b>Chapter 4. Symmetry breaking in hexagonal and cubic polymorphs of BaTiO<sub>3</sub> .....</b>	<b>49</b>
4.1 Introduction.....	49
4.2 Crystal structure of hexagonal and perovskite BaTiO <sub>3</sub> .....	49
4.3 Synthesis of apparently pure (single phase) hexagonal barium titanate .....	51
4.4 Dielectric permittivity as a function of temperature .....	57
4.5 Elastic properties of p- and h-BTO as a function of temperature .....	58
4.6 Dielectric Nonlinearity measurement .....	59
4.7 Pyroelectric measurement.....	60

4.8	Macroscopic symmetry breaking revealed by Thermally Stimulated Currents .....	62
4.9	Discussion and conclusion .....	65
	Bibliography .....	68
<b>Chapter 5. Origins of symmetry breaking in (Ba,Sr)TiO<sub>3</sub> system: processing issues</b>		<b>73</b>
5.1	Introduction .....	73
5.2	Effect of processing conditions on pyroelectric response of BST6040 .....	73
5.3	Effect of grain size on pyroelectric response of BST6040 .....	75
5.4	Effect of point defects on pyroelectric response of BST6040 .....	79
5.5	Summary .....	81
	Bibliography .....	82
<b>Chapter 6. Nonlinear behavior of polar entities.....</b>		<b>85</b>
6.1	Introduction .....	85
6.2	Polar entities .....	85
6.3	Rayleigh law .....	86
6.4	Higher harmonics analysis of dielectric polarization .....	88
6.5	Results and discussion .....	89
6.6	Summary .....	97
	Bibliography .....	98
<b>Chapter 7. Direct observation of polar entities in paraelectric phase of BST6040...103</b>		
7.1	Introduction .....	103
7.2	STEM investigation of BST6040 .....	104
7.3	Summary and conclusion .....	111
	Bibliography .....	112
<b>Chapter 8. Conclusions and perspectives .....</b>		<b>115</b>
8.1.	Symmetry breaking in hexagonal and cubic polymorphs of BaTiO <sub>3</sub> .....	115
8.2	Origins of the symmetry breaking in (Ba,Sr)TiO <sub>3</sub> system .....	116
8.3	Nonlinear behavior of polar entities in BST system .....	116
8.4	Direct observation of polar entities in paraelectric phase of BST6040 .....	118
8.5	Suggestions for future work .....	119
	Bibliography .....	120
Appendix A. Symmetry elements and point groups .....		121
Appendix B. HAADF-STEM image of Ba <sub>0.6</sub> Sr <sub>0.4</sub> TiO <sub>3</sub> .....		122
Appendix C. XRD patterns for h-BTO, p-BTO and BST6040 .....		123
<i>Curriculum vitae</i> .....		125



## Chapter 1. Background, thesis objective and outline

### 1.1 Introduction

In this chapter, a short overview is given on the relation between physical properties and the symmetry of materials. Principal electro-mechanical and electro-thermal coupling properties and their symmetry limitations are introduced in more details (piezoelectric, pyroelectric, flexoelectric, and ferroelectric effects). Next, a short review from early observations of symmetry breaking and the emergence of forbidden properties in the centrosymmetric paraelectric state of perovskite ferroelectrics in the literature is discussed. The thesis objective and outline are then presented at the end of the chapter.

### 1.2 Symmetry and physical properties

Relations between measurable quantities define physical properties of a material. Mathematically, physical properties are described by tensors ranked from zero to four. Symmetry arguments are used to determine the presence or the absence of physical properties. The question is how to relate these properties to the symmetry. Different symmetry elements and point groups are presented in Appendix A.

Four factors should be considered in studying effects of the symmetry on physical properties: i) the material symmetry, ii) the symmetry of external force, iii) the symmetry of material response to applied force and iv) the symmetry of physical property that relates the material response and the external force.

Neumann's principle [1, 2] is the key to relate the symmetry and physical properties and it could be stated as:

*"The symmetry element of any physical property of a crystal must include the symmetry elements of the point group of the crystal."*

This principle does not mean that symmetry elements of a point group and a physical property are the same. It just states that the symmetry elements of a physical property must include those of the point group. Often the physical property has more symmetry than the point group. Considering Neumann's principle and applying symmetry elements of each point group, it's possible to simplify the description of any rank tensor property by eliminating some coefficients and equalizing others [1, 2].

In the following sections piezoelectricity, pyroelectricity, flexoelectricity and ferroelectricity are described in more details, including their relation to the symmetry.

### 1.3 Piezoelectricity

The linear relationship between the applied stress  $\sigma_{jk}$  (N) and the resulting charge density  $D_i$  (C) is known as the direct piezoelectric effect (C/N) and is written as:

$$D_i = d_{ijk}\sigma_{jk} \tag{1.1}$$

## 1.4 Pyroelectricity

The charge density is a vector (first rank tensor) and the applied stress is a second rank tensor, so the physical property relating these two variables should be a third rank tensor.

Piezoelectric materials also change their dimensions (contraction or expansion) when an electric field  $E$  is applied. This property is known as the converse piezoelectric effect, and it describes the strain  $x_{ij}$  (m) that is developed in a material by applying electric field  $E_k$  (V). The unit of the converse piezoelectric coefficient is m/V.

$$x_{ij} = d_{kij} E_k \quad 1.2$$

Direct and converse piezoelectric coefficients are equal, which can be shown using thermodynamic relations. In following lines we show how symmetry affects the piezoelectricity.

To start, there are  $3^3 = 27$  components in the piezoelectric coefficient tensor, as mentioned in the previous section, the symmetry of external force also modifies the property tensor. Since the stress tensor is symmetrical, then  $\sigma_{ij} = \sigma_{ji}$  and 18 components of  $d_{kij}$  are independent. Using Neumann's principle for all crystallographic and Curie point groups shows that 11 crystal classes and four Curie groups are nonpiezoelectric. All but two of them are centrosymmetric. In general the presence of the center of symmetry eliminates all piezoelectric coefficients (Figure 1.1). To explain in more details, suppose for example, that a centrosymmetric material could produce a charge due to the application of stress; inverting the material would lead to a change in the charge sign, but this is not possible because the material is exactly the same after the inversion, due to its centrosymmetric characteristics. Because centrosymmetric fields and centrosymmetric materials cannot give polar responses, a centrosymmetric material cannot produce charge when stress is applied [1, 2].

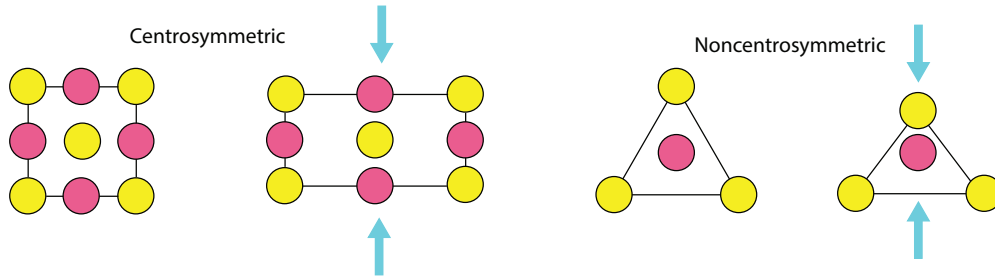


Figure 1.1 Piezoelectricity in centrosymmetric and noncentrosymmetric materials.

## 1.4 Pyroelectricity

Pyroelectricity is a physical property that relates polarization  $P_i$  or charge density  $D_i$  (in absence of electric field) to temperature change  $\delta T$ . Pyroelectric coefficient  $p_i$  is defined with a first rank tensor.

$$P_i = D_i = p_i \delta T \quad 1.3$$

In analogy to the discussion of piezoelectricity, it is possible to predict the presence of pyroelectricity just by using Neumann's principle.  $p_i$  is zero for all materials with a center of symmetry (same as the piezoelectric coefficient). Pyroelectric coefficient is nonzero only in crystals that have a polar direction. The two ends of a polar direction should not be related with each other by any symmetry elements of the point group. Thus all pyroelectric materials are piezoelectric but not vice versa. Out of 32 crystal classes and seven Curie groups, only 10 may theoretically show pyroelectricity and they are called polar classes: 1, 2, 3, 4, 6, m, mm2, 3m, 4mm, 6mm [1, 2].

## 1.5 Flexoelectricity

Flexoelectricity is a property that relates polarization to strain gradient for the direct effect. The thermodynamically equivalent converse effect describes the generation of elastic stress by an electric field gradient. Equation 1.4 describes the direct effect where  $P_i$  is the polarization induced by the elastic strain gradient  $X_{ij}$  in the direction of  $x_k$ .

$$P_i = \mu_{ijkl} \frac{\partial X_{ij}}{\partial x_k} \quad 1.4$$

Mathematically, the flexoelectric coefficient  $\mu_{ijkl}$  is a fourth rank tensor and is allowed in all symmetry groups. From a symmetry point of view, the inhomogeneous strain is the key point to understand this property [3]. The strain gradient may be induced by bending a sample or by application of a homogeneous stress on a sample with asymmetrical geometry like trapezoid or pyramid [4].

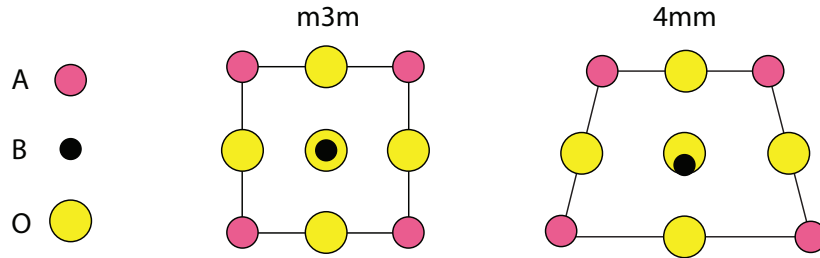


Figure 1.2 Symmetry change of a m3m lattice to 4mm due to strain gradient [5].

As explained in the section 1.3 when a material is centrosymmetric, it will continue to be so under a homogeneous deformation. As a result, there is no preferred direction for the polarization (no piezoelectricity in centrosymmetric materials). However, the strain gradient itself does break the center of the symmetry even in centrosymmetric materials so there is no symmetry limitation for the flexoelectricity. As illustrated in Figure 1.2, an unloaded lattice that belongs to m3m point group, is centrosymmetric and non-piezoelectric. But a strain gradient changes the symmetry point group to 4mm, which allows the sample to exhibit polarization.

Bursian [6] was one of the first who reported flexoelectricity in ferroelectric materials, without giving it a deeper theoretical explanation. It was Kogan [7] who proposed the first phenomenological model to define flexoelectricity. Tagantsev [8] expanded and generalized

Kogan's theory starting from the theory of the lattice dynamics. The flexoelectric coefficient is negligibly small for many materials, and Tagantsev suggested that this value should be multiplied by the relative permittivity in the case of high permittivity materials, including ferroelectrics. Based on Tagantsev, the flexoelectric coefficient in solid dielectrics can be written as

$$\mu_{ijkl} = \chi_{ij} Y_{kl} \left( \frac{e}{a} \right) \quad 1.5$$

Where  $\chi_{ij}$  is the dielectric susceptibility,  $Y_{kl}$  is the material flexoelectric tensor,  $a$  is the lattice parameter of the dielectric material, and  $e$  is the charge of the electron.

At first, the flexoelectric effect has attracted very small attention because it was expected to be very small in bulk materials. With the development of ferroelectric materials and also micro and nano-fabrication techniques, interests in flexoelectricity has started to grow mainly because of two factors: (a) it scales with the dielectric constant; materials with high value of permittivity such as relaxors and ferroelectrics could have large flexoelectric coefficients; (b) flexoelectricity can be huge in the nanoscale because it is proportional to the strain gradient and strain relaxation over a few nanometers in thin layers results in a much bigger gradient compared to relaxation over bulk scale. Flexoelectricity is apt to have a large effect on the function of nano-ferroelectric memory elements such as thin films, nanowires and nanotubes due to either extrinsic causes such as epitaxial strain relaxation or intrinsic causes such as surface tension and curvature [9].

## 1.6 Ferroelectricity

Ferroelectric materials are a subgroup of pyroelectrics. Like pyroelectrics, they have spontaneous polarization but it has more than one equilibrium orientation at zero electric field. In addition, the polarization in ferroelectrics can be switched from one direction to the another equilibrium direction by the application of an electric field. From a symmetry point of view, ferroelectrics belong to polar classes (same as pyroelectrics). However, it's not possible to determine their ability to reverse polarization only by symmetry investigation [10]. There are different functional and structural definitions for ferroelectrics, which are out of scope of this thesis, for more details read Ref. [11]. Whether or not a material is ferroelectric needs experimental validation. In other words, ferroelectricity is an empirical distinction between different types of pyroelectric crystals on the basis of experimental observation [12].

Most ferroelectrics experience a structural phase transition from a high-temperature non-polar (paraelectric) phase into a low-temperature ferroelectric phase with a lower symmetry compared to paraelectric phase. The phase transition temperature is called Curie temperature,  $T_C$ . Some ferroelectrics like  $\text{PbTiO}_3$  experience only one phase transition from the paraelectric to the ferroelectric phase (cubic to tetragonal for  $\text{PbTiO}_3$ ) while others also experience different ferroelectric to ferroelectric transitions. For instance, perovskite barium titanate ( $\text{BaTiO}_3$ ) transforms from cubic to tetragonal to orthorhombic to rhombohedral phases on cooling from high temperature [12]. Only the first phase transition from paraelectric to ferroelectric phase is called Curie point. Transition at  $T_C$  usually causes strong anomalies in physical properties of the material and also changes the crystal unit cell dimensions.

Most of ferroelectric materials with practical interest have perovskite structure, such as barium titanate, lead titanate and their different solid solutions. As illustrated in Figure 1.3 perovskite crystals have the general formula  $\text{ABO}_3$ , the valence of A cations can be from +1 to +3

and B cations from +3 to +6. Perovskites may also be viewed as  $\text{BO}_6$  octahedra surrounded by A site cations. The spontaneous polarization forms along  $C_T$  axis of the tetragonal unit cell as a result of relative B and O atomic shifts with respect to A site cations. When crystal goes through Curie phase transition from cubic to tetragonal phase, there are six possible directions for the spontaneous polarization formation (all directions along the  $a_C$  axes of the cubic cell including positive and negative orientation are equivalent and polarization can develop along all of them). The direction and orientation of the polarization across the sample depends on the electrical and mechanical boundary conditions of the sample [13].

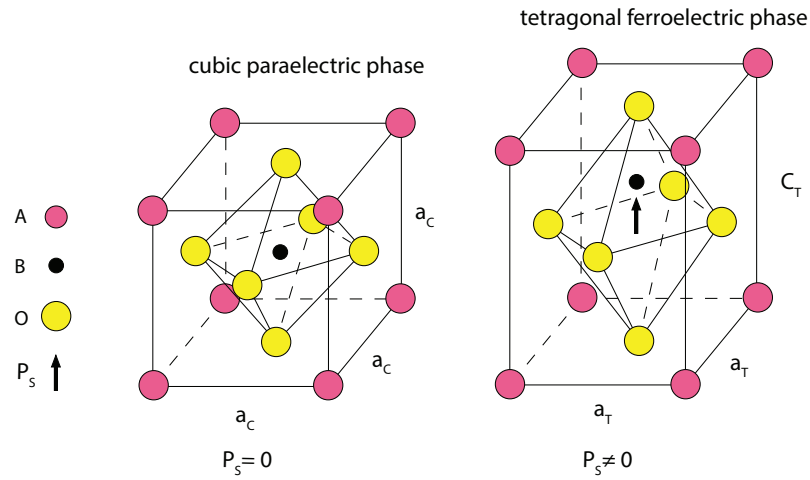


Figure 1.3 Cubic and tetragonal structures in a perovskite crystal.

Ferroelectric domains are the regions with uniformly oriented spontaneous polarizations and domain walls are regions that separate two neighboring domains. The reason for the domain formation is minimizing the electrostatic energy of the depolarizing field and the elastic energy related with mechanical constraints due to the paraelectric-ferroelectric phase transition. The spontaneous polarization  $P_s$  at  $T_C$  produces surface charges, which results in an electric field with opposite direction from  $P_s$  known as the depolarizing field  $E_d$ . The strong depolarizing field in case of a single domain state makes it energetically unfavorable. The formation of ferroelectric domains with the opposite orientation (so called  $180^\circ$  domains) minimizes the electrostatic energy associated with the depolarizing field. Domain formation in ferroelectrics could also be affected by the mechanical stress. To minimize energy, the long axis of the tetragonal phase develops perpendicular to the stress whilst in the unstressed parts of the crystal the polarization may remain parallel to the stress direction. As a result, domain walls separate regions in which the polarization direction is perpendicular to each other (known as  $90^\circ$  domain walls) [13]. Mechanisms for  $90^\circ$  and  $180^\circ$  domain wall formation are shown in Figure 1.4.

## 1.6 Ferroelectricity

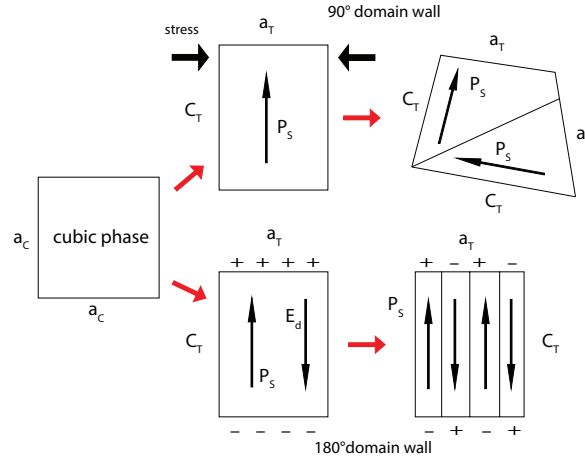


Figure 1.4 The schematic formation of 90° and 180° domain walls for cubic paraelectric to tetragonal ferroelectric phase transition [13].

Ferroelectric ceramics are always multi domain because of their complex elastic and electric boundary conditions. If the direction of spontaneous polarization is random in each domain, they cancel each other leading to zero net polarization. So the whole material does not show any piezoelectricity or pyroelectricity. Also from a symmetrical point of view, polycrystalline materials belong to  $\infty\infty m$  centrosymmetric point group and piezoelectricity or pyroelectricity are forbidden due to symmetry limitations.

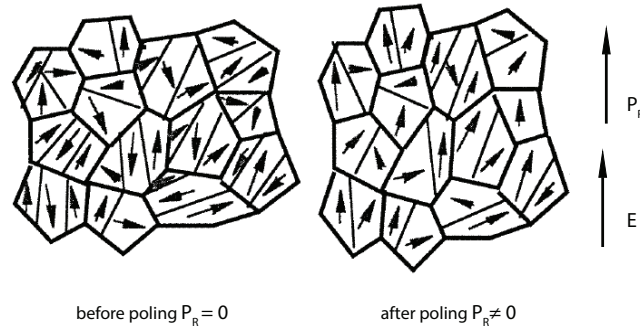


Figure 1.5 Ferroelectric polycrystalline ceramic before and after poling process [13].

However, because ferroelectrics possess more than one polar orientation their polycrystalline ceramics may be brought into a polar state by the poling process. It is defined as the application of an electric field (10-100 kV/cm) to the sample, usually at high temperatures. After the poling, the symmetry changes from  $\infty\infty m$  to  $\infty m$ , which is noncentrosymmetric and is able to show polar behavior [13]. Figure 1.5 shows a ferroelectric polycrystalline ceramic before and after the poling process.

## 1.7 Symmetry breaking in paraelectric phase of ferroelectrics above $T_C$

As mentioned in the previous section, ferroelectrics undergo a temperature-driven phase transition at  $T_C$  to a paraelectric phase, where polarization is lost. Moreover, they are mostly centrosymmetric (often cubic) and as a result are non-piezoelectric in their paraelectric state. Nevertheless, the effects that are forbidden by a centric symmetry have been reported in paraelectric phases of several ferroelectric materials [6, 14-17].

Despite being centrosymmetric, ferroelectrics still show some interesting forms of electro-mechanical coupling in their paraelectric phase. One is electrostriction, which relates strain and the square of the polarization, and the other is flexoelectricity (see section 1.5). Both of these properties exist in all symmetry groups and are practically strong in ferroelectrics. While electrostriction is a well-understood effect, there are lots of arguments around flexoelectricity. For instance, Cross [4] has shown that the flexoelectric coefficient of  $(\text{Ba}_{0.67}\text{Sr}_{0.33})\text{TiO}_3$  in its centrosymmetric paraelectric state at room temperature, is up to three to four orders of magnitude larger than its theoretically predicted value [18]. This result attracted attention of the many researchers and initiated studies to explain the difference between the theoretical and experimental results [19, 20]. Experimental data cannot be easily reconciled with theoretical predictions and such enormous controversy between these values demonstrates that either the theory is unable to fully explain the flexoelectric response, or another electro-mechanical mechanism is playing a role (partially or completely) in large apparent flexoelectric response of the material [4].

It has been shown [17] that ferroelectric materials with apparently large flexoelectric coefficient in the paraelectric phase exhibit symmetry breaking and consequently piezoelectric- and pyroelectric-like behavior. As shown in Figure 1.6, it was discovered that the paraelectric  $(\text{Ba,Sr})\text{TiO}_3$  trapezoid-shaped samples show polarization even if the stress is applied on the surfaces where no strain gradient should be generated. The order of magnitude of the generated charge was the same along directions where the shape-induced gradient was present and where it was absent [21].

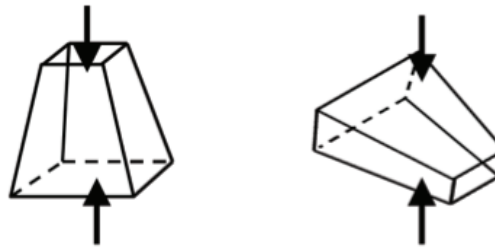


Figure 1.6 Schematic of experiment done by Biancoli that led to discovery of the symmetry breaking in  $(\text{Ba,Sr})\text{TiO}_3$  [21].

Thus, this experiment indicates that the centric symmetry of the material is broken, and illustrates that the non-flexoelectric type of electro-mechanical coupling increases or dominates the flexoelectric effect. Moreover, pyroelectric measurement done on the disk shape samples

## 1.7 Symmetry breaking in paraelectric phase of ferroelectrics above TC

(where no strain gradient is imposed by the sample shape and measurements) showed that material is not only noncentrosymmetric but is also polar. The discovered piezoelectric-like coupling could explain the large apparent flexoelectric coefficient. The authors also raised the question of the origins of the symmetry breaking and studied the possible mechanisms of polar behavior in the paraelectric phase of ferroelectric perovskites [21].

In this thesis work, our interest lies in describing and interpreting the conditions where breaking of the symmetry is not associated with the external field but is proper to the material and is not related to the flexoelectricity. By excluding the flexoelectricity as the origin of symmetry breaking due to reasons mentioned above, it is convenient to investigate the origins and mechanisms of symmetry breaking in three different cases: i) the local breaking of centrosymmetry; ii) the apparent symmetry breaking due to surface effects; and iii) the macroscopic (or bulk) symmetry breaking.

Local breaking of the centrosymmetry is the most investigated type of symmetry breaking in ferroelectric and related materials. It may refer to the existence of microscopic polar entities like polar nano-regions (PNR), polar clusters or tweed structures within the paraelectric material matrix and are sometimes assumed to be the precursors of the ferroelectric phase [16, 22-24]. The microscopic symmetry breaking may be due to the disordered displacement of ions in the unit cell (as observed in lead zirconate titanate PZT). In this case, polar nano regions could be formed by local clusters of correlated polar displacements of ions [25]. As another example, in (Ba,Sr)TiO<sub>3</sub> solid solution, the Sr/Ba ratio could displace Ti atom from its ideal cubic position in the paraelectric phase [26].

The polar nano regions form at certain temperatures called the Burns temperature [16]. Their presence is reported in paraelectric phase of many ferroelectrics sometimes up to hundreds of degree above  $T_C$  [25, 27-29]. Polar nano-regions are mostly studied systematically in relaxor ferroelectrics. PNR size is on the order of 2-3 nm and their dynamic is responsible for the particular properties of relaxor ferroelectrics like frequency dispersion and frequency dependence of the maximum value for the elastic compliance and the dielectric permittivity [22, 30]. The exact nature and formation mechanism of polar nano-regions are still not well understood after many years of investigation [31]. Narvaez and Catalan [32] proposed that the coupling between ferroelastically active polar nano-regions and bending strain gives an extrinsic contribution to the flexoelectric effect below a certain critical temperature. That work presents the first indirect evidence of a possible extrinsic contribution to the large apparent flexoelectric response in ferroelectrics.

Surface effects could be considered as obvious candidates for the breaking of the sample's symmetry [10]. In a parallel plate capacitor of any given material two surfaces are rarely identical, for instance in the case of a single crystal material, two surfaces may not terminate on the same plane of atoms [33]. Of course, this atomic-layer asymmetry could be easily compensated by charges from the electrode or environment and may not be detected by electrical measurements. On the other hand, it is reported that applying bending stress to the parallel plate capacitor with non-identical surfaces shows macroscopic piezoelectric-like response that is not flexoelectric in nature [34]. Also surface and bulk of material have different properties. There are different studies reporting appearance of ferroelectricity at the surface of BaTiO<sub>3</sub> crystals above Curie temperature while the bulk is paraelectric [10, 35]. The flexoelectric-related breaking of the centrosymmetry was also observed at the surface of the incipient ferroelectric SrTiO<sub>3</sub> [36, 37]. However, Biancoli et al. [17] have shown that surface-related phenomena are not the dominant origin of the built-in



polarization in perovskite ferroelectrics that they have investigated (see chapter 5). They studied electro-mechanical and pyroelectric responses in samples with different surface conditions: polished and as-sintered, electroded and non-electroded (in both polished and as-sintered state), and samples with different types of electrodes (Au, Au/Cr, Pt and silver paste). Based on their results, the polarization direction and magnitude is independent from surface conditions. Also removal of about half of the thickness of sample did not affect the magnitude of the response significantly nor its direction.

The mechanisms leading to macroscopic symmetry breaking are still unknown and there are few topics in the literature on this subject. Narvaez [32] has proposed that the electric field produced by flexoelectric effect itself can pole the material. However, it is not clear how flexoelectricity is able to create a field that give rise to an effect which is 2-3 orders of magnitude higher than the original flexoelectric response. Some have reported that symmetry breaking and polar properties in doped materials which experienced Curie phase transition could be related to the trapping of the residual polarization by defects [15, 38]; others studied symmetry breaking by the application of an electric field where the field itself could induce polarity [39]. On the other hand, there were studies considering the coupling of strain with charge entities [40] as the responsible mechanism of the macroscopic symmetry breaking. There are two different scenarios about strain-charge entities coupling. The first is associated with chemical expansivity and nonuniform distribution of charged defects [41] (oxygen or cation vacancies, aliovalent ions [42]). Defects distort the lattice of the material and give rise to microstrain. Conversely, the presence of appropriate strain decreases the activation energy of the defect formation as shown by the ab-initio calculations [43]. In some perovskite manganates, the formation of oxygen and cation vacancies is more probable by tensile and compressive strains, respectively [43]. Considering chemical expansivity, possible nonhomogeneous distribution of strain in the material results in a non-uniform concentration of the charge defects and consequently leads to macroscopic breaking of the sample's symmetry. The second scenario discusses the relation of polar nano-regions and strain. First principle calculations in  $\text{Ba}(\text{Zr,Ti})\text{O}_3$  thin films has shown that the polar nano-regions adopt preferential orientation (although not in the same direction) in presence of tensile strain [43]. As mentioned before, the macroscopic breaking of the centric symmetry due to polar nano-regions, clusters or precursors, would imply that a majority of those polar nano-entities are oriented in the same direction and in the same sense in the bulk of the material. Thus the symmetry is broken twice; first locally within the nano regions and then those regions adopt overall the same direction and break the symmetry globally. Schematic of such alignment is presented in Figure 1.7. In the left sample macroscopic polarization is zero because the summation of microscopic polarization cancels out each other, which, is not the case in the right sample.

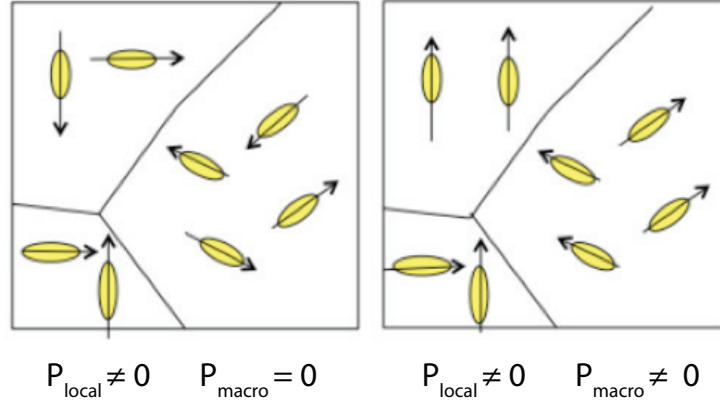


Figure 1.7 Schematic of local and macroscopic breaking of centric symmetry. Sample in right of figure represents both microscopic and macroscopic symmetry breaking.

## 1.8 Context and outline

To highlight the essential points mentioned in previous sections and also determine the objective of this thesis, it is possible to state that:

Perovskite ferroelectrics are non-centrosymmetric and polar below Curie Temperature ( $T_C$ ) and experience a temperature-driven phase transition at  $T_C$  to a paraelectric phase, where polarization is lost. The paraelectric phase of the most ferroelectrics is centrosymmetric (often cubic) and therefore non-piezoelectric. However, even in a centrosymmetric paraelectric phase, ferroelectrics exhibit large apparent flexoelectric coefficient and also interesting types of electro-mechanical and electro-thermal couplings that are forbidden by centric symmetry. The breaking of centric symmetry, and ensuing contribution to the large flexoelectric response of the material are of fundamental and possibly also practical interests. The size of the effects generated by symmetry breaking varies by a few orders of magnitude [17, 44] and while the total macroscopic effect is often, but not always, small, large effects may be expected at a small scale, and thus be of interest for nanoelectronics and nanomechanics [9, 45]. On the fundamental side, understanding mechanisms by which polar regions, nonhomogeneous distribution of charged defects and surface states give rise to the symmetry breaking is expected to give a deeper insight into the physics governing their origins.

This brings us to a very critical point. For presence of macroscopic polar response there should be a mechanism to align the microscopic symmetry breaking, otherwise the material does not show any polarity in bulk scale. Details of such mechanism are not clear yet. Surprisingly Salje et al. [46] by using molecular dynamics simulations have shown that a nonzero net macroscopic polarization could emerge in the sample where neither the original sample nor the applied perturbation breaks center of symmetry by itself. To put it in another word they proposed that if there is a collection of polar entities in the sample, these polar entities do not adopt perfect random distribution even in absence of external aligning mechanism like strain gradient.

The objective of this work is to investigate the origins and mechanism of symmetry breaking in paraelectric phase of ferroelectrics. To achieve our goal, ceramics of different

## Chapter 1. Background, thesis objective and outline

ferroelectrics (prepared by various processing techniques and conditions) were studied. The thesis is organized according to the following outline:

Chapter 2 explains different processing methods that have been used for sample fabrication. Also microstructural characterization techniques and dielectric measurement is discussed in this chapter.

Chapter 3 discusses the principles and set-ups of techniques that used for pyroelectric, elastic, and thermally stimulated current measurements, including their limits, advantages and disadvantages.

In chapter 4 the symmetry breaking is studied for barium titanate as an archetypal ferroelectric in its two different crystallographic structures (hexagonal and tetragonal). Through systematic studies and employing advanced dielectric, anelastic, pyroelectric and structural characterization we intend to achieve a deeper understanding of emergent electro-mechanical coupling in perovskite materials, especially in barium titanate.

Chapter 5 discusses evolution of the asymmetry in the samples with respect to different preparation parameters in (Ba,Sr)TiO<sub>3</sub> system which is a highly process-dependent material. By studying the material synthesized from different methods and also samples fabricated by other researchers we show the global nature of symmetry breaking for ferroelectrics above their Curie point. Moreover, such study enables us to enlighten the possible origin of the symmetry breaking.

Chapter 6 concerns the subject of nonlinearity and symmetry breaking. It is known that polar nano regions in relaxor ferroelectric materials contribute to dielectric nonlinearity and show dynamics similar to that observed by domain walls in ferroelectrics. The dielectric nonlinearity may thus be used as an indirect evidence of presence of polar regions in the paraelectric phase of a ferroelectric. We have shown that nonlinearity could be used to infer presence or absence of polar precursors in hexagonal and cubic polymorphs of BaTiO<sub>3</sub> [47]. In this chapter, dielectric nonlinearity of different compositions of Ba<sub>1-x</sub>Sr<sub>x</sub>TiO<sub>3</sub> (BST) solid solution (0 ≤ x ≤ 0.6) was investigated above T<sub>C</sub>.

The objective of Chapter 7 is to find direct evidence of polar regions presence above T<sub>C</sub> and understand their nature by high resolution transmission electron microscopy (HRTEM) study for Ba<sub>0.6</sub>Sr<sub>0.4</sub>TiO<sub>3</sub> (BST60-40) ceramics at room temperature. The Curie temperature of BST60-40 is 273K, and at room temperature, material is in its paraelectric phase. We investigated the direction and magnitude of A- and B-site atoms' displacement to visualize local atomic displacements and departure from the perfect cubic structure in the BST60-40 sample.

Chapter 8 concludes the results of previous chapters on the origins of symmetry breaking in paraelectric phase of ferroelectrics and also presents possible perspectives and suggestions for future work.

## Bibliography

- [1] R. E. Newnham, *Properties of Materials: Anisotropy, Symmetry, Structure*: OUP Oxford, 2005.
- [2] J. F. Nye, *Physical properties of crystals: their representation by tensors and matrices*: Oxford university press, 1985.
- [3] P. Zubko, G. Catalan, and A. K. Tagantsev, "Flexoelectric effect in solids," *Annual Review of Materials Research*, vol. 43, pp. 387-421, 2013.
- [4] L. E. Cross, "Flexoelectric effects: Charge separation in insulating solids subjected to elastic strain gradients," in *Frontiers of Ferroelectricity*, ed: Springer, 2006, pp. 53-63.
- [5] W. Ma, "Flexoelectric charge separation and size dependent piezoelectricity in dielectric solids," *physica status solidi (b)*, vol. 247, pp. 213-218, 2010.
- [6] E. V. Bursian and O. I. Zaikovski, "Changes in the curvare of a ferroelectric film due to polarization," *Sov. Phys.-Solid State*, vol. 10, pp. 1121-1124 1968.
- [7] S. M. Kogan and F. T. Tela, *Sov. Phys. Sohd State*, vol. 5, p. 2829, 1963.
- [8] A. Tagantsev, "Piezoelectricity and flexoelectricity in crystalline dielectrics," *Physical Review B*, vol. 34, p. 5883, 1986.
- [9] M. Majdoub, P. Sharma, and T. Cagin, "Enhanced size-dependent piezoelectricity and elasticity in nanostructures due to the flexoelectric effect," *Physical Review B*, vol. 77, p. 125424, 2008.
- [10] M. E. Lines and A. M. Glass, *Principles and Applications of Ferroelectrics and Related Materials*: OUP Oxford, 1977.
- [11] N. Setter, "What is a ferroelectric—a materials designer perspective," *Ferroelectrics*, vol. 500, pp. 164-182, 2016.
- [12] B. Jaffe, H. L. C. Jaffé, and W. R. Cook, *Piezoelectric Ceramics*, by Bernard Jaffe and William R. Cook Jr. and Hans Jaffe, 1971.
- [13] D. Damjanovic, "Ferroelectric, dielectric and piezoelectric properties of ferroelectric thin films and ceramics," *Reports on Progress in Physics*, vol. 61, p. 1267, 1998.
- [14] E.-M. Anton, W. Jo, D. Damjanovic, and J. Rödel, "Determination of depolarization temperature of (Bi1/2Na1/2) TiO3-based lead-free piezoceramics," *Journal of Applied Physics*, vol. 110, p. 094108, 2011.
- [15] C. Darlington and R. Cernik, "The ferroelectric phase transition in pure and lightly doped barium titanate," *Journal of Physics: Condensed Matter*, vol. 3, p. 4555, 1991.
- [16] G. Burns and F. Dacol, "Crystalline ferroelectrics with glassy polarization behavior," *Physical Review B*, vol. 28, p. 2527, 1983.
- [17] A. Biancoli, C. M. Fancher, J. L. Jones, and D. Damjanovic, "Breaking of macroscopic centric symmetry in paraelectric phases of ferroelectric materials and implications for flexoelectricity," *Nature materials*, vol. 14, pp. 224-229, 2015.
- [18] W. Ma and L. E. Cross, "Flexoelectric polarization of barium strontium titanate in the paraelectric state," *Applied Physics Letters*, vol. 81, pp. 3440-3442, 2002.
- [19] P. Yudin, R. Ahluwalia, and A. Tagantsev, "Upper bounds for flexoelectric coefficients in ferroelectrics," *Applied Physics Letters*, vol. 104, p. 082913, 2014.

- [20] P. Yudin and A. Tagantsev, "Fundamentals of flexoelectricity in solids," *Nanotechnology*, vol. 24, p. 432001, 2013.
- [21] A. Biancoli, "Breaking of the macroscopic centric symmetry in  $\text{Ba}_{1-x}\text{Sr}_x\text{TiO}_3$  ceramics and single crystals," 2014.
- [22] L. E. Cross, "Relaxor ferroelectrics," *Ferroelectrics*, vol. 76, pp. 241-267, 1987.
- [23] O. Aktas, M. A. Carpenter, and E. K. Salje, "Polar precursor ordering in  $\text{BaTiO}_3$  detected by resonant piezoelectric spectroscopy," *Applied Physics Letters*, vol. 103, p. 142902, 2013.
- [24] A. Bussmann-Holder, H. Beige, and G. Völkel, "Precursor effects, broken local symmetry, and coexistence of order-disorder and displacive dynamics in perovskite ferroelectrics," *Physical Review B*, vol. 79, p. 184111, 2009.
- [25] Y. Kuroiwa, Y. Terado, S. J. Kim, A. Sawada, Y. Yamamura, S. Aoyagi, *et al.*, "High-energy SR powder diffraction evidence of multisite disorder of Pb atom in cubic phase of  $\text{PbZr}_{1-x}\text{Ti}_x\text{O}_3$ ," *Japanese journal of applied physics*, vol. 44, p. 7151, 2005.
- [26] I. Levin, V. Krayzman, and J. C. Woicik, "Local structure in perovskite (Ba, Sr)  $\text{TiO}_3$ : Reverse Monte Carlo refinements from multiple measurement techniques," *Physical Review B*, vol. 89, p. 024106, 2014.
- [27] R. Comes, M. Lambert, and A. Guinier, "The chain structure of  $\text{BaTiO}_3$  and  $\text{KNbO}_3$ ," *Solid State Communications*, vol. 6, pp. 715-719, 1968.
- [28] W. Kleemann, F. Schäfer, and M. Fontana, "Crystal optical studies of spontaneous and precursor polarization in  $\text{KNbO}_3$ ," *Physical Review B*, vol. 30, p. 1148, 1984.
- [29] W. Kleemann, F. Schäfer, and D. Rytz, "Crystal optical studies of precursor and spontaneous polarization in  $\text{PbTiO}_3$ ," *Physical Review B*, vol. 34, p. 7873, 1986.
- [30] H. Uršič and D. Damjanovic, "Anelastic relaxor behavior of  $\text{Pb}(\text{Mg}_{1/3}\text{Nb}_{2/3})\text{O}_3$ ," *Applied Physics Letters*, vol. 103, p. 072904, 2013.
- [31] M. E. Manley, J. Lynn, D. Abernathy, E. Specht, O. Delaire, A. Bishop, *et al.*, "Phonon localization drives polar nanoregions in a relaxor ferroelectric," *Nature communications*, vol. 5, 2014.
- [32] J. Narvaez and G. Catalan, "Origin of the enhanced flexoelectricity of relaxor ferroelectrics," *Applied Physics Letters*, vol. 104, p. 162903, 2014.
- [33] A. K. Tagantsev, "Electric polarization in crystals and its response to thermal and elastic perturbations," *Phase Transitions: A Multinational Journal*, vol. 35, pp. 119-203, 1991.
- [34] A. K. Tagantsev and A. S. Yurkov, "Flexoelectric effect in finite samples," *Journal of Applied Physics*, vol. 112, p. 044103, 2012.
- [35] v. M. Anliker, H. Brugger, and W. Kanzig, "DAS VERHALTEN VON KOLLOIDALEN SEIGNETTEELEKTRIKA. 3. BARIUMTITANAT  $\text{BaTiO}_3$ ," *Helvetica Physica Acta*, vol. 27, pp. 99-124, 1954.
- [36] A. Kholkin, I. Bdikin, T. Ostapchuk, and J. Petzelt, "Room temperature surface piezoelectricity in  $\text{SrTiO}_3$  ceramics via piezoresponse force microscopy," *Applied Physics Letters*, vol. 93, p. 222905, 2008.
- [37] I. Bdikin, B. Singh, J. S. Kumar, M. Graca, A. Balbashov, J. Grácio, *et al.*, "Nanoindentation induced piezoelectricity in  $\text{SrTiO}_3$  single crystals," *Scripta Materialia*, vol. 74, pp. 76-79, 2014.

- [38] H. Beige and G. Schmidt, "Electromechanical resonances for investigating linear and nonlinear properties of dielectrics," *Ferroelectrics*, vol. 41, pp. 39-49, 1982.
- [39] K. Rusek, J. Kruczek, K. Szot, D. Rytz, M. Gorny, and K. Roleder, "Non-Linear Properties of BaTiO<sub>3</sub> above T<sub>C</sub>," *Ferroelectrics*, vol. 375, pp. 165-169, 2008.
- [40] X. Chen, Y. Zou, G. Yuan, M. Zeng, J. Liu, J. Yin, *et al.*, "Temperature Gradient Introduced Ferroelectric Self - Poling in BiFeO<sub>3</sub> Ceramics," *Journal of the American Ceramic Society*, vol. 96, pp. 3788-3792, 2013.
- [41] Z. Kighelman, D. Damjanovic, and N. Setter, "Electromechanical properties and self-polarization in relaxor Pb (Mg<sub>1/3</sub>Nb<sub>2/3</sub>) O<sub>3</sub> thin films," *Journal of Applied Physics*, 2000.
- [42] S. B. Adler, "Chemical expansivity of electrochemical ceramics," *Journal of the American Ceramic Society*, vol. 84, pp. 2117-2119, 2001.
- [43] U. Aschauer, R. Pfenninger, S. M. Selbach, T. Grande, and N. A. Spaldin, "Strain-controlled oxygen vacancy formation and ordering in CaMnO<sub>3</sub>," *Physical Review B*, vol. 88, p. 054111, 2013.
- [44] W. Zhou, P. Chen, Q. Pan, X. Zhang, and B. Chu, "Lead - Free Metamaterials with Enormous Apparent Piezoelectric Response," *Advanced Materials*, vol. 27, pp. 6349-6355, 2015.
- [45] G. Catalan, J. Seidel, R. Ramesh, and J. F. Scott, "Domain wall nanoelectronics," *Reviews of Modern Physics*, vol. 84, p. 119, 2012.
- [46] E. K. Salje, S. Li, M. Stengel, P. Gumbsch, and X. Ding, "Flexoelectricity and the polarity of complex ferroelastic twin patterns," *Physical Review B*, vol. 94, p. 024114, 2016.
- [47] S. Hashemizadeh, A. Biancoli, and D. Damjanovic, "Symmetry breaking in hexagonal and cubic polymorphs of BaTiO<sub>3</sub>," *Journal of Applied Physics*, vol. 119, p. 094105, 2016.

## Chapter 2. Material processing and characterization

### 2.1 Introduction

In this chapter we start with a brief introduction on barium titanate and its compositional modification with focus on barium strontium titanate. Next, different processing methods (solid-state and sol-gel) for processing of the  $\text{Ba}_{1-x}\text{Sr}_x\text{TiO}_3$  ceramics are discussed. Different processing conditions and starting powders result in large differences of physical and dielectric properties in BST system and many other ceramics. Our objective was to process high density, homogeneous samples with different processing routes to show that symmetry breaking is not only limited to samples processed with one specific method and is a general and global phenomenon. The solid-state route was already optimized in our laboratory and sol-gel method was optimized in this research. After preparation of the samples, their structural and compositional properties were analyzed with density measurements, X-ray diffraction method and Scanning Electron Microscopy (SEM). Dielectric properties were measured and considered as figure of merit to confirm the quality of processed ceramics.

### 2.2 Barium Titanate

Barium titanate  $\text{BaTiO}_3$  (referred as BTO in this text) was the first inorganic piezoelectric ceramic developed [1]. It is considered as the cornerstone of the electroceramics market with applications in capacitors, thermistors and piezoelectric devices [2]. Barium titanate possesses two basic structures, a perovskite one (referred as p-BTO in this text) and a hexagonal form (h-BTO in text) which both become ferroelectric at certain temperatures. According to the  $\text{BaO-TiO}_2$  phase diagram shown in Figure 2.1, the hexagonal polymorph is only stable above 1733 K (see chapter 4 for more discussion). The cubic polymorph is the usual ceramic product of barium titanate. At 130°C centrosymmetric cubic BTO elongates along one edge of its unit cell and becomes tetragonal and ferroelectric. Upon further cooling two other polymorphic phase transitions occur.

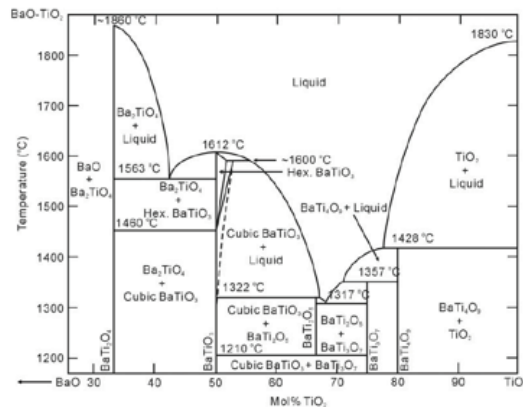


Figure 2.1 Phase equilibrium in the  $\text{BaO-TiO}_2$  system [3].

## 2.2 Barium Titanate

Large anomalies are observed in the dielectric permittivity of BTO at each phase transition as shown in Figure 2.2 [4]. Figure 2.3 explains in more details the structure and unit cell characteristics of each BTO polymorphs. Cubic BTO undergoes a sequence of phase transitions from the high temperature centrosymmetric paraelectric-paraelastic cubic phase to a tetragonal phase at  $T_C \approx 473$  K, orthorhombic phase at  $\approx 278$  K and rhombohedral phase at  $\approx 183$  K, all of which are ferroelectric-ferroelastic, with polarization as the order parameter [5]. Hexagonal BTO (h-BTO) transforms at  $T_{\text{trans}} \approx 222$  K from the high temperature centrosymmetric paraelectric-paraelastic hexagonal phase to an orthorhombic noncentrosymmetric (i.e., piezoelectric) paraelectric-ferroelastic phase. h-BTO becomes ferroelectric-ferroelastic below  $T_C \approx 60$ -74 K [6-8].

In BTO phase transitions show thermal hysteresis between cooling and heating because of their first-order nature [9]. There are different parameters that affect transition temperatures and the amount of thermal hysteresis such as crystal/grain size [10, 11], cooling/heating rate, stress condition and purity of sample [12].

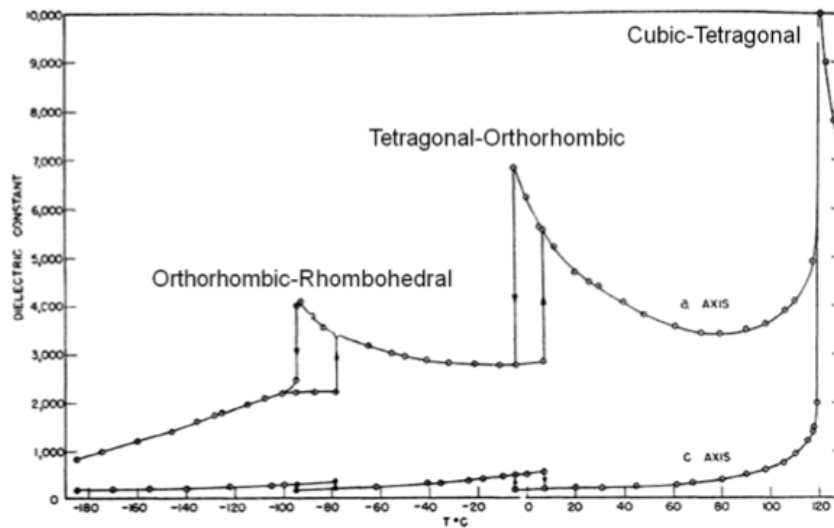


Figure 2.2 Dielectric constant of single crystal  $\text{BaTiO}_3$  as a function of temperature along the a and c axis [4].



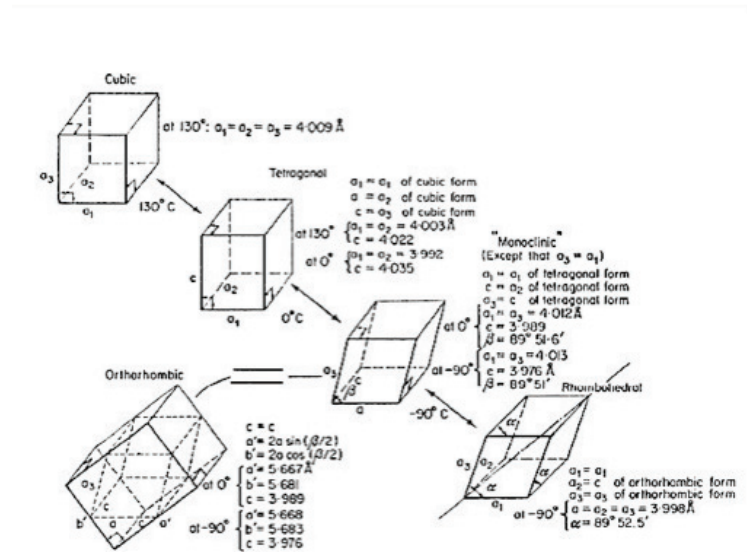


Figure 2.3 Phase transitions in perovskite barium titanate [1].

## 2.3 Compositional modification of barium titanate

As mentioned before barium titanate undergoes several polymorphic phase transitions in cooling through the Curie point, which are accompanied with drastic structural and properties variations. Due to this reason the operation of BTO devices over extended temperature ranges is unsatisfactory in many cases [13]. As a result compositional modification of Barium titanate attracted a lot of interest since its discovery. The purpose of such modifications is to stabilize the dielectric, piezoelectric and elastic properties of BTO by decreasing or increasing the Curie temperature or to acquire different polymorphs of BTO at desired temperatures.  $\text{BaTiO}_3$  can be modified by substitution of both  $\text{Ba}^{2+}$  and  $\text{Ti}^{4+}$  by either cations with same valence (isovalent substitution) or different one (aliovalent substitution). These cations could substitute A-position, B-position and/or simultaneously both positions [1]. For instance  $\text{Ca}^{2+}$  replaces  $\text{Ba}^{2+}$  and strongly lowers the tetragonal-orthorhombic transition temperature while it does not change  $T_C$ . Substitution of  $\text{Pb}^{2+}$  with  $\text{Ba}^{2+}$  raises the Curie point monotonically from  $120^\circ\text{C}$  for BTO to  $490^\circ\text{C}$  for pure  $\text{PbTiO}_3$ . It also decreases the temperature of two other phase transitions.  $T_C$  decreases linearly with  $\text{Sr}^{+2}$  substitution in A-site and  $(\text{Ba},\text{Sr})\text{TiO}_3$  has higher dielectric peak values than pure  $\text{BaTiO}_3$ . In metatitanates, replacement of  $\text{Ti}^{+4}$  by  $\text{Zr}^{+4}$ ,  $\text{Sn}^{+4}$  or  $\text{Hf}^{+4}$  shift the Curie point below room temperature and minor replacement (under 10 atomic %) increase the orthorhombic-tetragonal transition temperature in a way that orthorhombic phase become stable at room temperature. Such modification leads to an increase in ferroelectric polarization maintaining the piezoelectric coefficient high and also decrease in dielectric constant at room temperature [1]. Figure 2.4 shows the effect of typical isovalent substitutions for A- and B-site of BTO.

## 2.4 Material selection

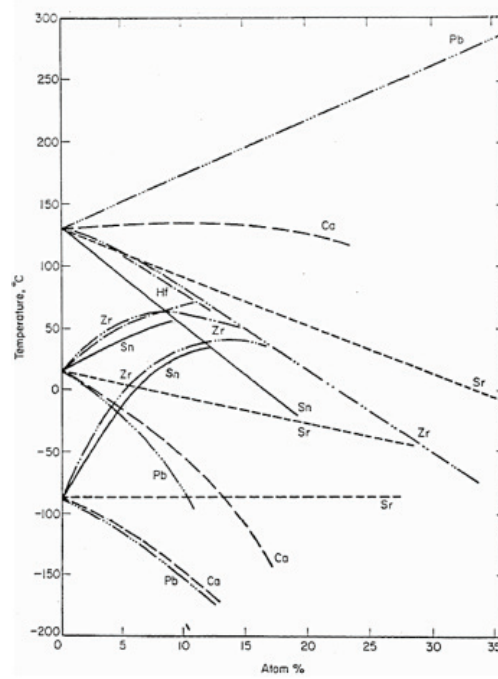


Figure 2.4 Effect of different isovalent substitutions on Barium titanate transition temperatures [1].

## 2.4 Material selection

Perovskite oxides with  $ABO_3$  as their general chemical formula are among the most versatile and interesting functional materials from both scientific and technological point of view [14]. Different types of perovskites show large dielectric permittivity ( $BaTiO_3$ ), strong piezoelectric coefficient and switchable polarization ( $Pb(Zr,Ti)O_3$ ), multiferroic and magnetoelectric effects ( $BiFeO_3$ ), magneto resistive effect ( $La_{0.7}Ca_{0.3}MnO_3$ ), and emergent properties like superconductivity at the interface between two insulating perovskite materials ( $LaAlO_3/SrTiO_3$ ). Mentioned functionalities are employed in sensors, capacitors, transducers, actuators, and recently in solar cells.

$Ba_{1-x}Sr_xTiO_3$  (BST) solid solution has been considered as an important family of perovskite materials. The research on BST started more than 50 years ago and since then different studies were carried out on BST powder processing, ceramic, single crystal, thin film fabrication and properties [15-20]. BST has numerous applications in different devices like radio frequency and microwave capacitors [21, 22], infrared pyroelectric sensors [23] and dynamic random access memories (DRAMs) [24]. In addition, recent discovery of large flexoelectric coefficient in BST composition [25] has attracted attention of many scientists and opened an entirely new research direction.

Dr. Alberto Biancoli [26] the former Ph. D student of our laboratory started his research to study the origin and mechanism of reported large flexoelectric polarization in perovskite  $Ba_{1-x}Sr_xTiO_3$  (BST) solid solutions. However, the systematical investigations carried out in that work led to uncovering the nominally forbidden, macroscopic polar character of the paraelectric

phase in unpoled barium strontium titanate ceramics. As the continuation of his research our goal is to establish the origins of the symmetry-breaking for the BST system.

BST family represents an ideal system to study the symmetry breaking of ferroelectrics in their paraelectric phase for different reasons. First, complete solubility of barium and strontium would enable us to stabilize ferroelectric and paraelectric phase of the material at different temperatures just by small changes in stoichiometry whilst all other processing parameters are kept constant. Second, BST system with strontium content higher than 80% changes from ferroelectric to relaxor, offering us the possibility to compare material's polar response in paraelectric phase of ferroelectrics and the ergodic phase of relaxors without variation of the chemical background. Third, two ends of BST system (pure barium titanate BTO and strontium titanate STO) give us opportunity to study the symmetry breaking in chemically simpler materials. Finally by varying Sr content from 0 to 1 the relative dielectric permittivity of samples changes by two orders of magnitude, which makes it feasible to verify any possible relation between material permittivity and emergent symmetry breaking.

In addition to perovskite BTO, we were able to stabilize pure hexagonal BTO at room temperature [27], which was a great asset to study the origin of symmetry breaking in pure BTO (for detailed discussion see chapter 4).

Several compositions of BST were processed in addition to pure BTO and STO in order to cover the entire range of the solid solution. All the ceramics were synthesized from the same starting powders with similar processing conditions. For simplicity a nomenclature is used for labeling the  $\text{Ba}_{1-x}\text{Sr}_x\text{TiO}_3$  system. For instance,  $\text{Ba}_{60}\text{Sr}_{40}\text{TiO}_3$  is labeled as BST6040. All the compositions that are processed in our lab are listed in Table 2.1.

Table 2.1 Compositions of  $\text{Ba}_{1-x}\text{Sr}_x\text{TiO}_3$  solid solution investigated in this study and their main dielectric properties

Composition	Label	$T_C$ on cooling	Permittivity at room temperature
$\text{BaTiO}_3$	p-BTO	403 K	1960
	h-BTO	60 K	120
$\text{Ba}_{60}\text{Sr}_{40}\text{TiO}_3$	BST6040	273 K	6000
$\text{Ba}_{50}\text{Sr}_{50}\text{TiO}_3$	BST5050	237 K	1800
$\text{Ba}_{33}\text{Sr}_{67}\text{TiO}_3$	BST3367	170 K	700
$\text{Ba}_{10}\text{Sr}_{90}\text{TiO}_3$	BST1090	65 K	300
$\text{SrTiO}_3$	STO	-	260

## 2.5 Ceramic processing

The primary method for preparing BST ceramics was classical solid-state reaction method. BST6040 (main composition) was also processed by sol-gel rout because using two different processing paths helped us to study their effect on chemical order and homogeneity of the material and consequently on its macroscopic properties. In addition, it is interesting to see whether the preparation method has an influence on appearance of symmetry breaking above Curie temperature. Chemical purity, very fine particle size and better homogeneity are some of expected

## 2.5 Ceramic processing

advantages of sol-gel over solid-state route. Pure BTO and STO ceramics were processed from commercially acquired powders.

We used the route provided in Ref. [28] for processing BST6040 sol-gel powder. All the precursors and solvents are shown in Table 2.2. The Titanium precursor was Titanium (IV) butoxide, stabilized with acetylacetone in a two molar ratio  $[\text{Ti}(\text{OBU})_2(\text{acac})_2]$ . Barium and strontium acetate were used as Ba and Sr precursors. To obtain the BST solution, stoichiometric amounts of barium and strontium acetate were dissolved in acetic acid in separate containers at room temperature, then mixed with stoichiometric amount of Ti compound and diluted with 2-methoxyethanol (parent alcohol of acetate solutions) to reach 0.3 M molarity for final solution. In the next step, the obtained solution was heated at 373 K overnight with continuous stirring for gel formation. The resultant dried gel was grounded to powder by a mortar and pestle. The obtained powder was calcined in a covered high purity alumina crucible at different temperatures. The optimized calcination condition was 1423 K for two hours with a heating and cooling rate of 5 K/min. Processing steps after calcination is the same for both solid-state and sol-gel powder and will be explained at the end of this section.

Table 2.2 Precursors used for sol-gel synthesis of BST6040

Precursor/solvent	Supplier	Form	Purity	Impurities
Titanium (IV) butoxide	Sigma-Aldrich	Liquid	$\geq 97\%$	
Barium acetate	Sigma-Aldrich	Powder	$\geq 99\%$	$\leq 0.0005\%$ heavy metals
Strontium acetate	Sigma-Aldrich	Powder		
Acetic acid	Sigma-Aldrich	Liquid	$\geq 99.7\%$	
Acetylacetone	Sigma-Aldrich	Liquid	$\geq 99\%$	
2-Methoxyethanol	Sigma-Aldrich	Liquid	99.8%	$< 0.0005\%$ water

Figure 2.5 represent the flow chart of sol-gel process for BST sample processing.

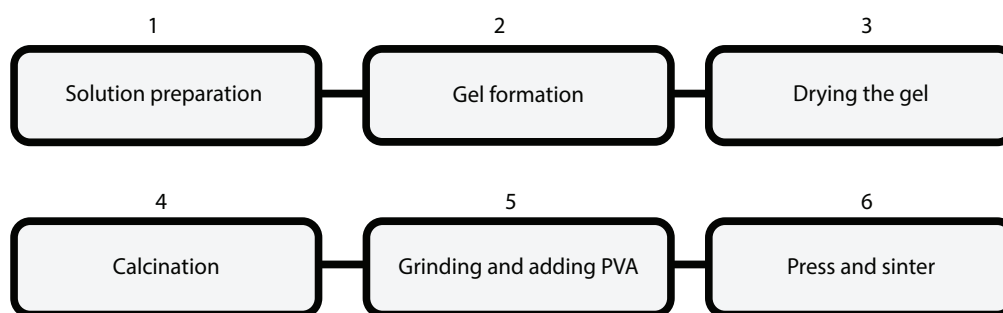


Figure 2.5 Process flow chart of the sol-gel method .

Solid-state method to fabricate BST was already optimized by Biancoli [26] (Figure 2.6). In this method already reacted commercially acquired barium and strontium titanate powders with

high purity and fine grain size were used as precursors (Table 2.3). The starting powders were dispersed in isopropanol according to stoichiometric amount needed for each composition then the obtained slurry was mixed and milled by  $\text{ZrO}_2$  balls (5 mm diameter) for 24 hours using a planetary milling machine. Typically there were 70 g of powders, 80 ml of isopropanol and 550 g of  $\text{ZrO}_2$  balls. The purpose of milling is to achieve proper homogeneity of the mixture to avoid formation of secondary phase during calcination.

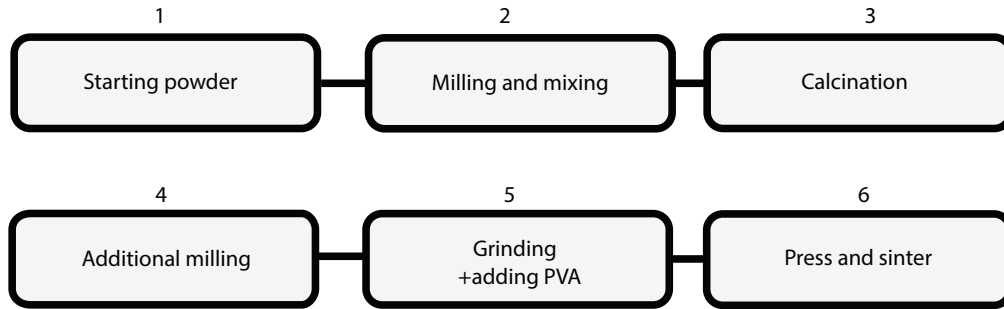


Figure 2.6 Process flow chart for the solid state processing of BST ceramics.

Table 2.3 Starting powders used for solid-state processing of BST system.

Powder	Supplier	Particle size	Purity	Impurities
Barium titanate	Inframat Advanced materials	200 nm	99.95 %	Ca<0.001 % Fe<0.001 % K<0.001 % Mg<0.001 % Na<0.001 % Sr<0.0015 %
Strontium titanate	Inframat Advanced materials	100 nm	99.95 %	Ca<0.008 % Fe<0.006 % K<0.005 % Mg<0.002 % Na<0.006 %

Short mixing time could lead to nonhomogeneous distribution of  $\text{Ba}^{+2}$  and  $\text{Sr}^{+2}$  and results in the broadening of the dielectric constant peak at the Curie point [29]. After milling, the mixture was dried in a glass beaker on a hot plate at 358 K. Simultaneously the slurry was placed under an IR lamp to increase the rate of isopropanol evaporation. The whole drying process took around 4 hours. Calcination of dried powder was performed in same conditions as sol-gel powder.

In this part we discuss the processing steps after calcination. The granulometry was performed at Institute Josef Stefan (IJS) in Ljubljana, Slovenia, to investigate the particle size distribution for calcined BST6040 sol-gel powder. As shown in the Figure 2.7 calcined sol-gel powder has very coarse agglomerates. Another wet milling step was necessary to break the large agglomerates formed during calcination. The coarse particle size is undesired because it could

## 2.5 Ceramic processing

interrupt the sintering process and results in inhomogeneous reaction, compositional variation and secondary phase formation. According to Biancoli [26] calcined solid-state powders has the same conditions as sol-gel powders after calcination and extra milling was mandatory.

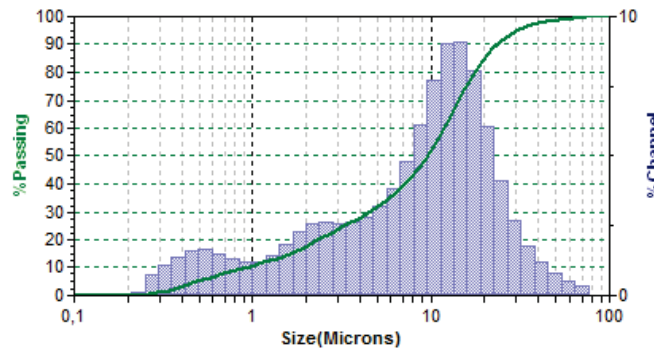


Figure 2.7 Granulometry data for calcined sol-gel prepared BST6040 powders.

After second ball milling 4% solution of polyvinyl alcohol (PVA) and deionized water was added to calcined powders as a binder with binder/powder ratio of 1/25 in weight. Using binder improves the plasticity of powder and lowers the possibility of crack formation during pressing. The powder-binder mixture was pressed into pellets by application of uniaxial load using a stainless steel cylindrical die with a tungsten carbide inner core and tungsten carbide pistons.

Solid-state powders were pressed with load of 70 MPa into pellets with 7 mm diameter and 1 mm thickness for dielectric measurements and 0.5 mm thickness for pyroelectric measurements. Sol-gel powders were pressed with 240 MPa to disk shaped samples with mentioned dimensions. Sol-gel powders have smaller grain size than solid-state powders so the pressure was higher in order to achieve desired density after sintering. For Dynamic mechanical analysis, powders were pressed to rectangle shaped samples with final dimensions of 7mm x 50 mm x 25 mm.

In the final step, solid-state pressed green samples were sintered in air in at 1723 K for 4 hours with 5 K/min heating and cooling rates. To identify sintering conditions for BST6040 sol-gel powders, dilatometry experiments were also performed at IJS, where green pellet was heated up to 1773 K and shrinkage of the pellet's diameter was measured as function of temperature (Figure 2.8). The maximum shrinkage took place around 1723 K and it was chosen for sintering temperature (dwell time of 4 hours).

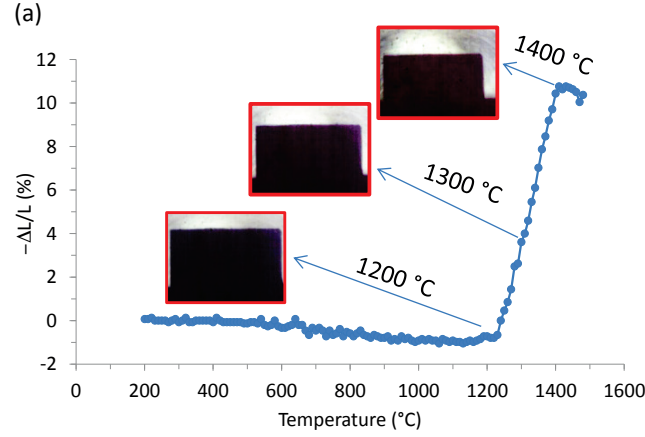


Figure 2.8 Shrinkage of the pellet's diameter as a function of temperature (heating rate 5 K/min,  $T_{\max}=1773$  K) with corresponding images of the pellet at three different temperatures.

Other  $Ba_{1-x}Sr_xTiO_3$  compositions that were processed in this research: BST1090, BST3367, BST5050 and BST6733 were processed exactly by same method optimized for BST6040 so their processing conditions and their structural and compositional analysis are not shown here.

As mentioned earlier, our Ba precursor was already formed  $BaTiO_3$ . As a result no calcination step was needed for fabrication of pure BTO. In case of p-BTO starting powder was mixed for 24 hours before pressing and sintered at 1723 K for 4 hours. For h-BTO as-received powder was pressed without any milling step and sintered at 1773 K for 4hours (for more discussion see chapter 4).

## 2.6 Density measurement

The geometrical densities of sintered samples were obtained from their weight and geometrical volume. Surface and bulk of sample could have different densities so the weights of samples were measured after mechanical polishing with Silicon Carbide papers (grit size of 1000) and cleaning samples for 5 minutes in acetone. The relative densities of ceramics were calculated as:

$$\rho_{\text{relative}} = \frac{\rho_{\text{geometrical}}}{\rho_{\text{theoretical}}} \quad 2.1$$

The theoretical densities were calculated from:

$$\rho_{\text{theoretical}} = \frac{\text{Molar mass} \times Z}{N_A \times V_{\text{cell}}} \quad 2.2$$

where  $Z$  is the number of formula unit contained in one unit cell ( $Z=1$  in case of BST),  $N_A$  is the Avogadro number and  $V_{\text{cell}}$  is the volume of unit cell calculated from the lattice constants obtained from XRD patterns.

## 2.7 X-Ray diffraction and compositional analysis

Relative densities of p-BTO and h-BTO samples were 94% and 95% of the theoretical densities respectively and all BST compositions possess density of 94%-98% of theoretical values.

### 2.7 X-Ray diffraction and compositional analysis

X-ray diffraction (XRD) was used to analyze phase formation and crystalline quality for both calcined powders and sintered samples. The scans were performed at room temperature using a Bruker D8 Discovery diffractometer with monochromatic CuK $\alpha$ 1 radiation (1.540596 Å) in the range from 20° to 80°. Scans were recorded in a  $\theta$ -2 $\theta$  geometry in 1D mode with scanning speed of 2 degrees per minute. To index the diffracted peaks we have used Powder Diffraction Files (PDF) provided by International Center for Diffraction Data (ICDD). p-BTO with tetragonal structure at room temperature was indexed according to tetragonal BTO PDF card 00-005-0626, Hexagonal BTO indexed with PDF card number 00-034-0129 and BST6040 with cubic structure at room temperature indexed with card number 00-034-0411.

Figure 2.9 shows the X-ray diffraction pattern of p-BTO and h-BTO. The patterns are in perfect match with reference PDF cards. As mentioned in the previous section, same starting powders were used for fabrication of both hexagonal and perovskite BTO. The as-received powders measured at room temperature reveals that it has tetragonal structure of p-BTO. The reasons for retention of h-BTO phase at room temperature after sintering will be discussed in details in chapter 4. For tetragonal barium titanate the splitting of {100}, {110}, {101}, and {200}, {002} peaks that is characteristic of P4mm space group is clearly visible.

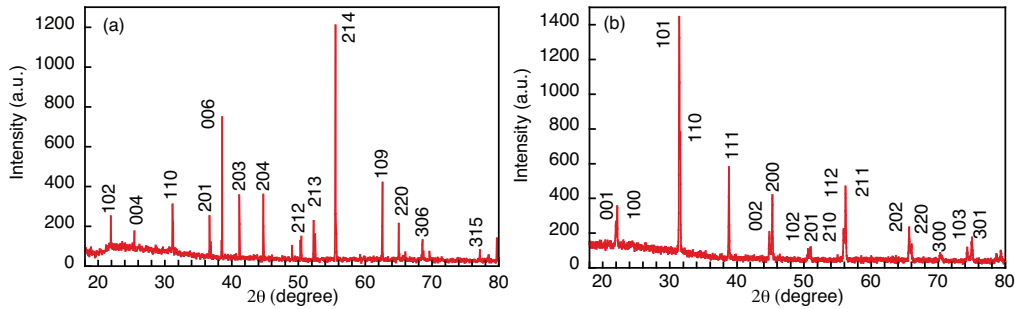


Figure 2.9 XRD patterns for a) h-BTO and b) p-BTO. See appendix C for larger graphs.

Figure 2.10 and Figure 2.11 represent XRD patterns for solid-state reacted and sol-gel BST6040 powders and samples respectively. In XRD pattern of BST6040 that is cubic at room temperature (Pm-3m cubic space group) the tetragonal peaks merge into single peaks for {100}, {110} and {200}. For both sol-gel and solid-state samples the sintering temperature was 300 K more than their calcination temperature, so peaks for sintered sample are sharper and due to the larger crystalline size, have higher intensities compared to powders.



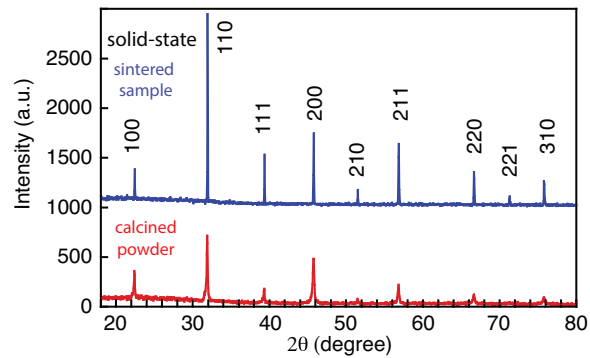


Figure 2.10 XRD spectra on the solid-state derived calcined powder and sintered sample of BST6040. See appendix C for larger image. See appendix C for larger graphs.

Diffraction peaks for all processed material are sharp indicating the homogenous calcination and sintering processes. The scans for all materials did not contain any extra peaks linked to existence of secondary phase or contamination originated from high temperature sintering process.

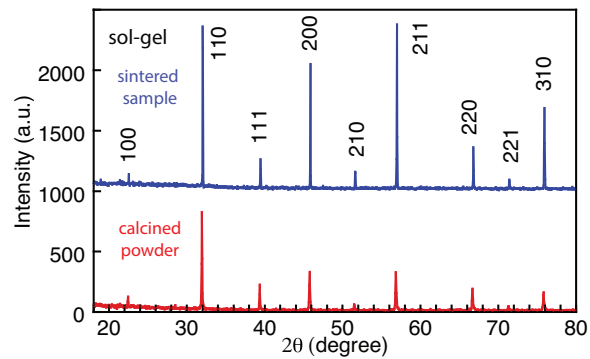


Figure 2.11 XRD spectra on the sol-gel derived calcined powder and sintered sample of BST6040. See appendix C for larger graphs.

It should be mentioned that due to the limited detection resolution of XRD technique (above 2-3%), small quantities of secondary phase could not be detected with XRD and as result could not be excluded based on this analysis.

Biancoli has performed energy dispersive X-ray spectrometry (EDS) for BST6040 (processed with exact conditions and starting powder as here) to investigate compositional homogeneity of sintered samples in more details [26]. His analysis suggests existence of a small quantity of a secondary phase where the ratio between barium and titanium is about 2 to 1 with very small traces of strontium. Secondary phase is likely to be  $\text{Ba}_2\text{TiO}_4$  orthotitanate [3, 30]. It is very small fraction of the ceramics (less than 1%) and could not be detected with XRD analysis.

## 2.8 Scanning electron microscopy

Due to the fact that this barium rich phase is present in samples sintered at different temperatures, its origin cannot be related with high temperature sintering of the ceramic. This reason and the fact that ceramics were synthesized with direct mixing of  $\text{BaTiO}_3$  and  $\text{SrTiO}_3$  and not from decomposition of  $\text{BaCO}_3$  and  $\text{SrCO}_3$  suggest that the secondary phase could be present in the Ba starting powder [26].

## 2.8 Scanning electron microscopy

Morphology and particle size distribution of raw powders and also microstructure of sintered ceramics (grain size, grain boundaries and surface porosity) were characterized by scanning electron microscopy (SEM). Images were taken by FEI-Teneo scanning electron microscope using in-lens and Everhart detectors. Microstructure of all ceramics is well packed and compact with low porosity. Figure 2.12 shows micrographs of p-BTO and h-BTO ceramics. p-BTO has large grains ranging from 20 to 50  $\mu\text{m}$  combined with smaller grains that is typical for barium titanate ceramics processed at high temperatures [1, 31]. For hexagonal BTO grain size is varying from 20 to 80  $\mu\text{m}$ . This exaggerated grain growth could be due to the presence of (111) twins in particular grains [32]. Presence of pores on the surface of h-BTO could be because of the consumption of smaller grains by large ones due to severe recrystallization at very high temperatures (1773 K). High density (more than 95% of theoretical density) and extremely low dielectric loss of h-BTO samples suggest the existence of the pores only on the surface of sintered ceramics.

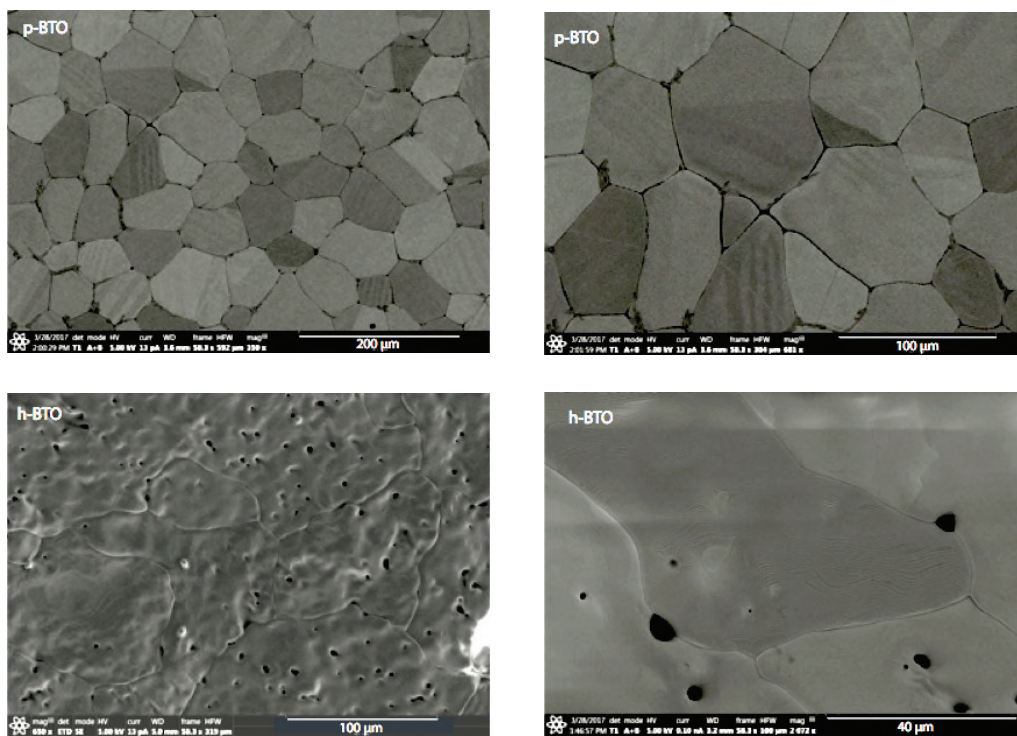


Figure 2.12 Surface SEM micrographs of as sintered p-BTO, h-BTO.

Microstructural analyze of BST solid-state powders has already been done by Biancoli [26] and is not discussed here. Figure 2.13 exhibits the micrographs of sol-gel derived powder and as-sintered ceramics (solid state and sol-gel prepared) of BST6040. After wet milling of calcined powder most of the agglomerates are broken and the particles are in the range of 50-150 nm. The average grain size decreases significantly by increasing the strontium content in  $\text{Ba}_{1-x}\text{Sr}_x\text{TiO}_3$  compositions. Grain size range in BST6040 is 5-20  $\mu\text{m}$  in solid-state reacted and sol-gel samples. All other processed BST compositions have a very similar microstructure to BST6040 solid-state.

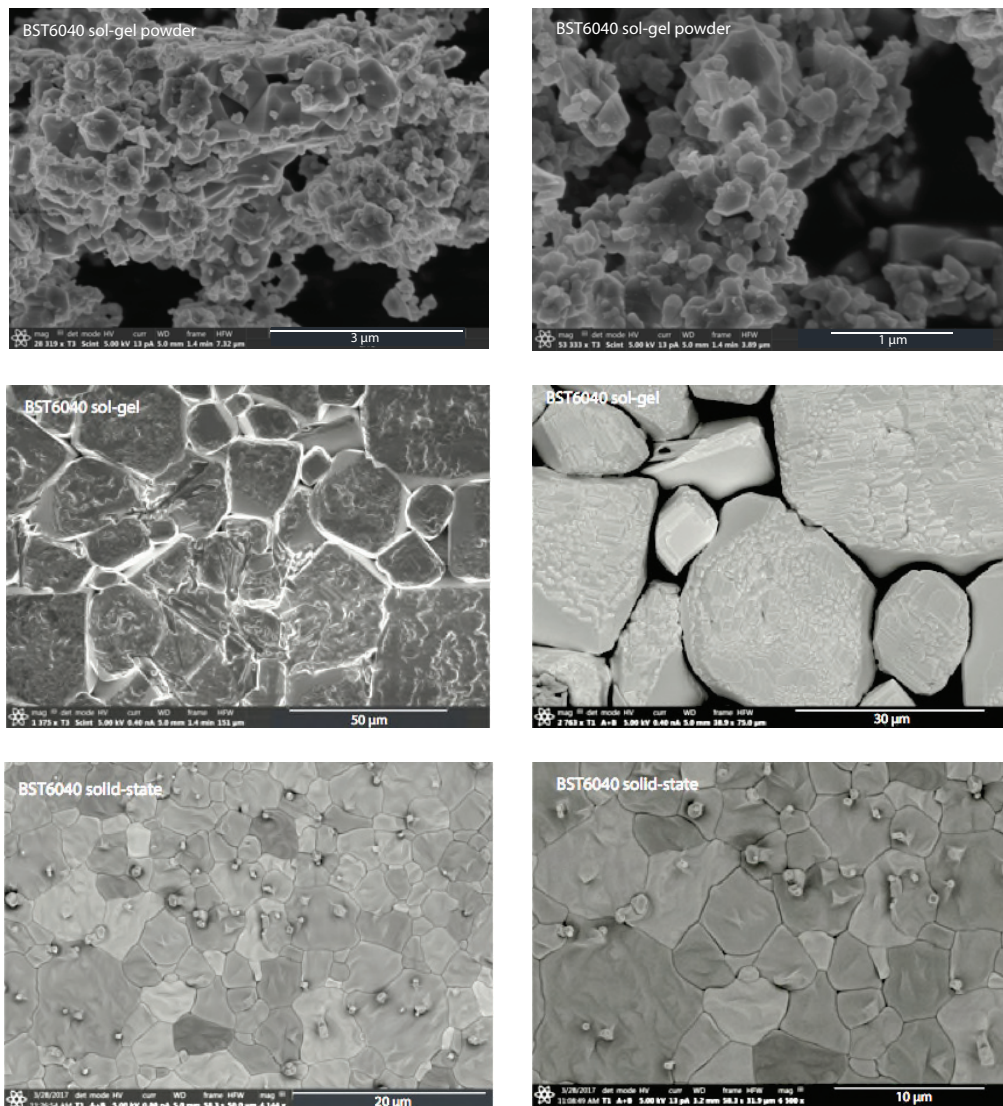


Figure 2.13 Surface SEM micrographs of BST6040 powders and ceramics processed by solid-state and sol-gel.

## 2.9 Dielectric properties measurements

Measurement of the dielectric permittivity as a function of temperature is the most common technique to detect different phase transitions in ferroelectric systems. The dielectric permittivity and loss were measured between 100 and 450 K at several frequencies (100 Hz-1 KHz-10 KHz and 100 KHz). The amplitude of the driving field was 1 V<sub>rms</sub> and measurements were carried out by using an HP 4284A high precision LCR meter while sample was placed in a Delta 9023 temperature chamber in case of BST system and p-BTO. For measuring dielectric permittivity of h-BTO a CTI-cryogenics refrigerator model 22 is used to achieve very low temperatures i.e. 30 K. Measurements were made only during cooling, with the rate of 2 K/min.

The relative dielectric permittivity  $\epsilon_r$  was determined from measured values of the sample's capacitance C:

$$\epsilon_r = \frac{C \times t}{\epsilon_0 \times A} \quad 2.3$$

Where t and A are sample thickness and area respectively and  $\epsilon_0$  is vacuum permittivity.

Figure 2.14 exhibits the measured relative dielectric permittivity as a function of temperatures for barium titanate and Ba<sub>1-x</sub>Sr<sub>x</sub>TiO<sub>3</sub> compositions that fabricated by solid-state process (BST6040-BST5050-BST3367-BST1090).

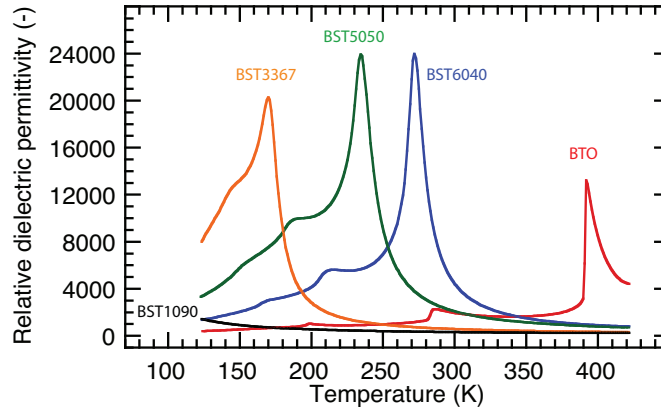


Figure 2.14 Relative dielectric permittivity as a function of temperature for BTO and Ba<sub>1-x</sub>Sr<sub>x</sub>TiO<sub>3</sub> compositions at 1 KHz.

The trend of the Curie temperature (taken as the maxima of real part of dielectric permittivity) versus composition respects Vegard's law and therefore indicates that Ba and Sr precursors are well mixed and homogeneously distributed over A-sites of the perovskite structure. The temperature of Curie point decreases linearly with reduction of barium concentration in barium rich compositions (Figure 2.15 taken from [26]). This relation becomes gradually nonlinear in strontium rich compositions. This behavior is consistent with reported data in the literature [33]. Moreover, with increasing the strontium content dielectric permittivity peaks become more

diffuse, and dielectric anomalies related to the tetragonal-orthorhombic and orthorhombic-rhombohedral phase transitions become concealed and finally become suppressed for strontium amount more than 80% [29, 33].

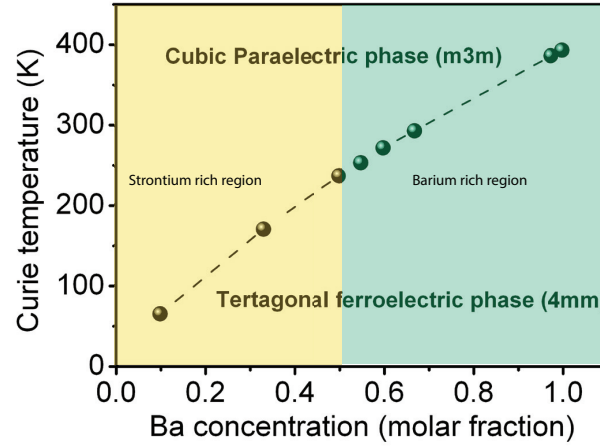


Figure 2.15 Curie temperature variation as a function Barium content in BST system [26]

Dielectric measurements also show thermal hysteresis for the phase transition temperatures revealing that they are first order transitions (shown for BST6040 in Figure 2.16). This fact suggests that ceramics possess high compositional order and is another indication for homogeneous distribution of A-site cations. Inhomogeneous BST ceramics show diffuse phase transition (DFT) at the paraelectric to the ferroelectric state even for small amounts of strontium [34], absence of such behavior in our case is another proof for the uniformity of the processed ceramics.

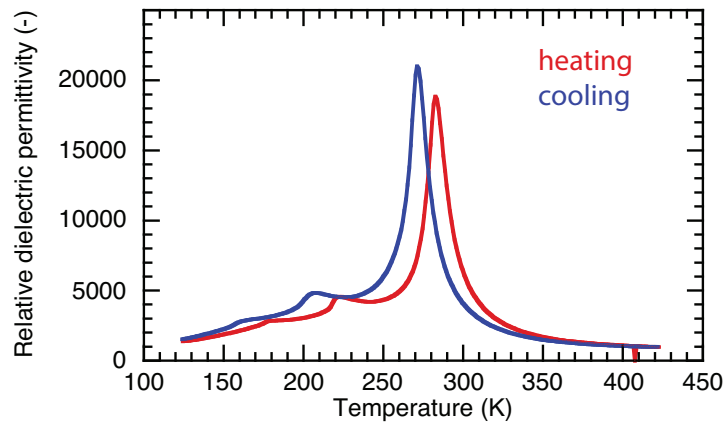


Figure 2.16 Thermal hysteresis observed for BST6040 dielectric permittivity during heating and cooling.

## 2.9 Dielectric properties measurements

Figure 2.17 compares the dielectric permittivity and loss for BST6040 processed by sol-gel and solid-state methods. This could be taken as a confirmation for the stoichiometry of our sol-gel sample (in addition to XRD data). Because of two different chemical routes used for sol-gel and solid-state reacted sample, it is expected that the samples will not have a similar nature of chemical defects. The slight differences in dielectric permittivity and the lower dielectric loss in sol-gel derived samples could confirm this assumption. The sol-gel derived samples could help us to study the effect of different processing routes on symmetry breaking (see chapter 5).

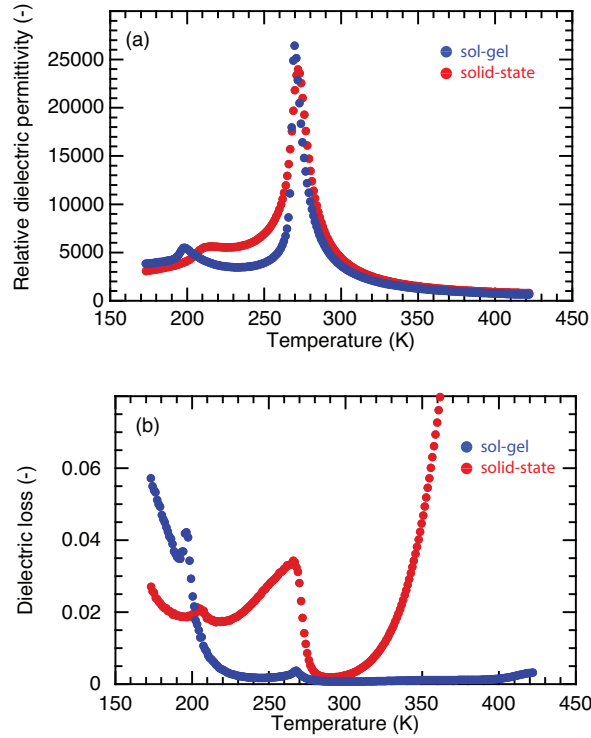


Figure 2.17 a) dielectric permittivity and b) dielectric loss measured at 1 KHz for sol-gel and solid-state BST6040.

In Figure 2.18, the frequency and temperature dependent dielectric measurements show that the frequency dispersion is almost negligible for our main materials (p-BTO, h-BTO and BST6040), which is expected for materials with low content of strontium. Addition of strontium leads to frequency dispersion due to decreasing the order of the system. Dielectric losses are less than 5% for all frequencies for all compositions at room temperature. At elevated temperatures (above 370 K) and especially at low frequencies, the dielectric losses show significant increase, which is associated with the higher conductivity of samples due to detrapping of space charges in the sample.



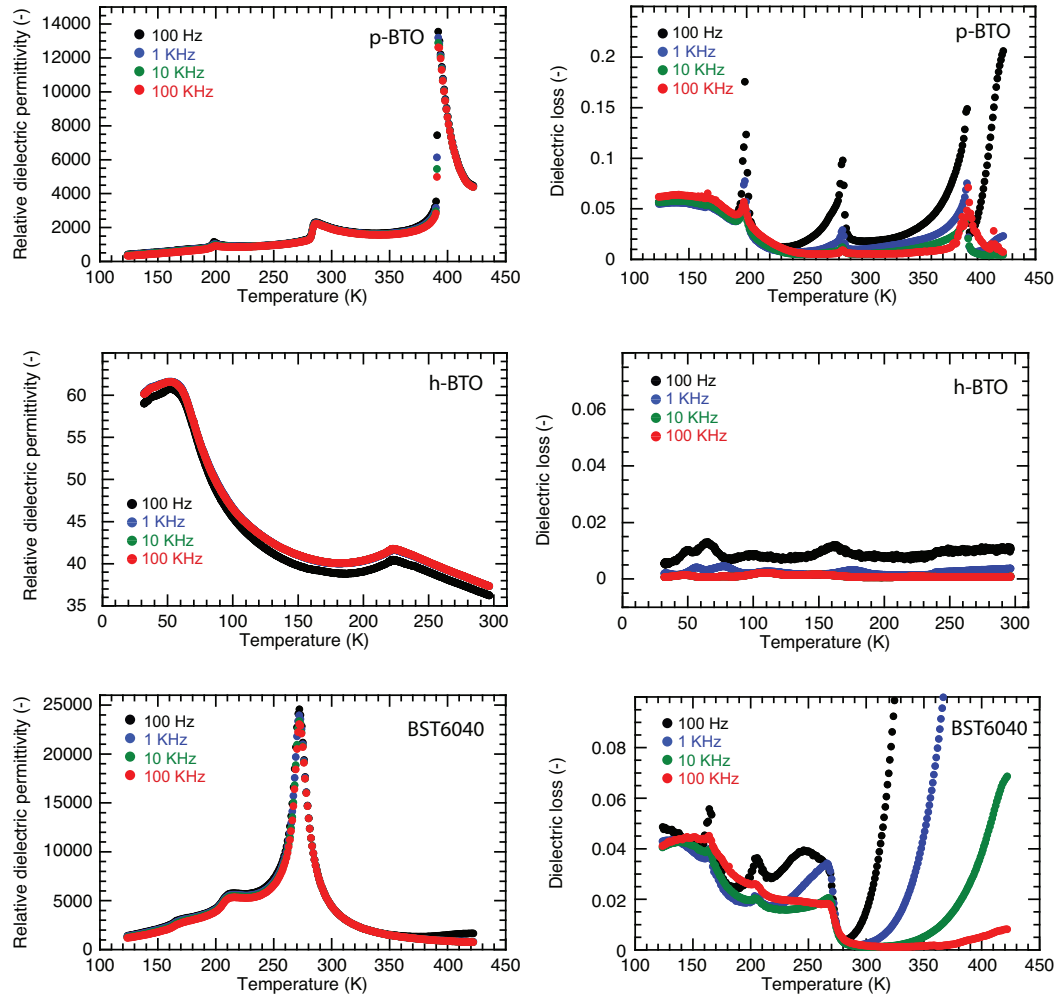


Figure 2.18 Temperature and frequency dependence of relative dielectric permittivity and loss for p-BTO, h-BTO and solid-state BST6040.

## 2.10 Summary

In this chapter we have discussed the material selection and different techniques that were used for sample preparation. XRD, EDS and SEM characterizations were performed to study the phase formation, chemical homogeneity and microstructure of starting powders and sintered ceramics. Dielectric permittivity and loss as a function of temperature were measured to identify different phase transitions. A good agreement of obtained dielectric data with what has been reported in the literature is a confirmation of desirable chemical homogeneity of synthesized samples.

## Bibliography

- [1] B. Jaffe, *Piezoelectric ceramics* vol. 3: Elsevier, 2012.
- [2] D. Sinclair, J. S. Skakle, F. Morrison, R. Smith, and T. Beales, "Structure and electrical properties of oxygen-deficient hexagonal BaTiO<sub>3</sub>," *Journal of Materials Chemistry*, vol. 9, pp. 1327-1331, 1999.
- [3] D. Rase and R. Roy, "Phase equilibria in the system BaO–TiO<sub>2</sub>," *Journal of the American Ceramic Society*, vol. 38, pp. 102-113, 1955.
- [4] W. J. Merz, "The Electric and Optical Behavior of BaTiO<sub>3</sub> Single-Domain Crystals," *Physical Review*, vol. 76, p. 1221, 1949.
- [5] A. K. Tagantsev, L. E. Cross, and J. Fousek, *Domains in ferroic crystals and thin films*: Springer, 2010.
- [6] K. Deguchi, H. Kobayashi, E. Nakamura, H. Yamaguchi, H. Uwe, and T. Sakudo, "Dielectric dispersion and twin structure in hexagonal barium titanate," *Journal of the Physical Society of Japan*, vol. 57, pp. 4011-4020, 1988.
- [7] E. Sawaguchi, Y. Akishige, and M. Kobayashi, "Ferroelectric behavior in hexagonal type barium titanate," *Japanese Journal of Applied Physics*, vol. 24, p. 252, 1985.
- [8] E. Sawaguchi, Y. Akishige, and M. Kobayashi, "Structural phase transition in hexagonal barium titanate," *Journal of the Physical Society of Japan*, vol. 54, pp. 480-482, 1985.
- [9] D. Damjanovic, "Ferroelectric, dielectric and piezoelectric properties of ferroelectric thin films and ceramics," *Reports on Progress in Physics*, vol. 61, p. 1267, 1998.
- [10] K. Kinoshita and A. Yamaji, "Grain - size effects on dielectric properties in barium titanate ceramics," *Journal of Applied Physics*, vol. 47, pp. 371-373, 1976.
- [11] K. Uchino, E. Sadanaga, and T. Hirose, "Dependence of the crystal structure on particle size in barium titanate," *Journal of the American Ceramic Society*, vol. 72, pp. 1555-1558, 1989.
- [12] H. Kay, H. Wellard, and P. Vousden, "Atomic positions and optical properties of barium titanate," *Nature*, vol. 163, pp. 636-637, 1949.
- [13] D. A. Berlincourt and F. Kulcsar, "Electromechanical properties of BaTiO<sub>3</sub> compositions showing substantial shifts in phase transition points," *The Journal of the Acoustical Society of America*, vol. 24, pp. 709-713, 1952.
- [14] J. Rödel, W. Jo, K. T. Seifert, E. M. Anton, T. Granzow, and D. Damjanovic, "Perspective on the Development of Lead - free Piezoceramics," *Journal of the American Ceramic Society*, vol. 92, pp. 1153-1177, 2009.
- [15] S. Nomura, "Solid state reaction between barium titanate and strontium titanate," *Journal of the Physical Society of Japan*, vol. 11, pp. 924-929, 1956.
- [16] P. Padmini, T. Taylor, M. Lefevre, A. Nagra, R. York, and J. Speck, "Realization of high tunability barium strontium titanate thin films by rf magnetron sputtering," *Applied Physics Letters*, vol. 75, pp. 3186-3188, 1999.
- [17] F. Schrey, "Effect of pH on the Chemical Preparation of Barium - Strontium Titanate," *Journal of the American Ceramic Society*, vol. 48, pp. 401-405, 1965.



- [18] G. Shirane and K. Sato, "Effects of mechanical pressures on the dielectric properties of polycrystalline barium-strontium titanate," *Journal of the physical Society of Japan*, vol. 6, pp. 20-26, 1951.
- [19] A. Tagantsev, V. Sherman, K. Astafiev, J. Venkatesh, and N. Setter, "Ferroelectric materials for microwave tunable applications," *Journal of electroceramics*, vol. 11, pp. 5-66, 2003.
- [20] S. Ueda, "Crystal growth and dielectric properties of barium strontium titanate Ba<sub>0.97</sub>Sr<sub>0.03</sub>TiO<sub>3</sub>," *Materials Research Bulletin*, vol. 9, pp. 469-476, 1974.
- [21] F. A. Miranda, C. H. Mueller, C. D. Cabbage, K. B. Bhasin, R. K. Singh, and S. D. Harkness, "HTS/ferroelectric thin films for tunable microwave components," *IEEE Transactions on Applied Superconductivity*, vol. 5, pp. 3191-3194, 1995.
- [22] A. Tombak, F. T. Ayguavives, J.-P. Maria, G. T. Stauff, A. I. Kingon, and A. Mortazawi, "Low voltage tunable barium strontium titanate thin film capacitors for RF and microwave applications," in *Microwave Symposium Digest. 2000 IEEE MTT-S International*, 2000, pp. 1345-1348.
- [23] J. S. Lee, J.-S. Park, J.-S. Kim, J.-H. Lee, Y. H. Lee, and S.-R. Hahn, "Preparation of (Ba, Sr) TiO<sub>3</sub> thin films with high pyroelectric coefficients at ambient temperatures," *Japanese journal of applied physics*, vol. 38, p. L574, 1999.
- [24] W. Hsu, J. Luttmmer, R. Tsu, S. Summerfelt, M. Bedekar, T. Tokumoto, *et al.*, "Direct current conduction properties of sputtered Pt/(Ba<sub>0.7</sub>Sr<sub>0.3</sub>) TiO<sub>3</sub>/Pt thin films capacitors," *Applied physics letters*, vol. 66, pp. 2975-2977, 1995.
- [25] W. Ma and L. E. Cross, "Flexoelectric polarization of barium strontium titanate in the paraelectric state," *Applied Physics Letters*, vol. 81, pp. 3440-3442, 2002.
- [26] A. Biancoli, "Breaking of the macroscopic centric symmetry in Ba<sub>1-x</sub>Sr<sub>x</sub>TiO<sub>3</sub> ceramics and single crystals," 2014.
- [27] S. Hashemizadeh, A. Biancoli, and D. Damjanovic, "Symmetry breaking in hexagonal and cubic polymorphs of BaTiO<sub>3</sub>," *Journal of Applied Physics*, vol. 119, p. 094105, 2016.
- [28] S. Hoffmann and R. Waser, "Control of the morphology of CSD-prepared (Ba, Sr) TiO<sub>3</sub> thin films," *Journal of the European Ceramic Society*, vol. 19, pp. 1339-1343, 1999.
- [29] L. Zhou, P. Vilarinho, and J. Baptista, "Dependence of the Structural and Dielectric Properties of Ba<sub>1-x</sub>Sr<sub>x</sub>TiO<sub>3</sub> Ceramic Solid Solutions on Raw Material Processing," *Journal of the European Ceramic Society*, vol. 19, pp. 2015-2020, 1999.
- [30] J. Bland, "The crystal structure of Barium orthotitanate, Ba<sub>2</sub>TiO<sub>4</sub>," *Acta Crystallographica*, vol. 14, pp. 875-881, 1961.
- [31] M. Demartin, C. Hérard, C. Carry, and J. Lemaître, "Dedensification and anomalous grain growth during sintering of undoped barium titanate," *Journal of the American Ceramic Society*, vol. 80, pp. 1079-1084, 1997.
- [32] A. Rečnik and D. Kolar, "Exaggerated growth of hexagonal barium titanate under reducing sintering conditions," *Journal of the American Ceramic Society*, vol. 79, pp. 1015-1018, 1996.
- [33] V. Lemanov, E. Smirnova, P. Syrnikov, and E. Tarakanov, "Phase transitions and glasslike behavior in Sr<sub>1-x</sub>Ba<sub>x</sub>TiO<sub>3</sub>," *Physical Review B*, vol. 54, p. 3151, 1996.

- [34] V. Tiwari, N. Singh, and D. Pandey, "Diffuse ferroelectric transition and relaxational dipolar freezing in (Ba, Sr) TiO<sub>3</sub>," *Journal of Physics: Condensed Matter*, vol. 7, p. 1441, 1995.

## Chapter 3. Experimental techniques

### 3.1 Introduction

The purpose of this chapter is to explain in details the main experimental techniques that have been used to characterize the materials of this study. To study the symmetry breaking phenomena above Curie temperature we have used elastic, dielectric, pyroelectric and thermally stimulated current measurements. The basics and instrument set-up of each measurement method are described in the following sections.

### 3.2 Dynamic mechanical analysis

Dynamic mechanical analysis (DMA) could be described as applying an oscillating force to a sample and analyzing the material's response to the applied force as a function of frequency and temperature. If the applied sinusoidal force is small enough, sample's deformation is also sinusoidal. The material's response is reproducible as long as it's been kept within its linear viscoelastic region.

Applied stress is defined by:

$$\sigma(t) = \sigma_0 \sin(\omega t) \quad 3.1$$

Where  $\sigma$  is stress at time  $t$ ,  $\sigma_0$  is maximum stress and  $\omega$  is oscillation frequency. The resulting strain depends on the viscoelasticity of the sample. If material is ideally elastic, strain  $\epsilon$  is defined by equation 3.2. There is no energy loss by elastic behavior; so stress and strain are in phase with each other.

$$\epsilon(t) = \epsilon_0 \sin(\omega t) \quad 3.2$$

On the other hand, the general response of material is defined as below, where  $\delta$  is phase lag:

$$\epsilon(t) = \epsilon_0 \sin(\omega t + \delta) \quad 3.3$$

Measuring the amplitude of the deformation and also the phase lag between stress and strain would enable us to calculate different mechanical properties of material such as complex Young's modulus (Figure 3.1) [1].

For dynamic mechanical analysis we have used a Pyris Diamond module from Perkin Elmer Instruments (built by Seiko). It measures the dynamic viscoelasticity, creep recovery and stress relaxation using bending, single-cantilever, tension, shear, and compression methods over wide range of temperature (-150°C to 600°C) and frequency (0.01 Hz to 100Hz). Heating and cooling rates could be set from 0.01 to 20°C/min. Maximum force is  $\pm 10$  N in static mode and  $\pm 8$  N in dynamic mode. In the version available to us we do not have access to temporal behavior of the strain  $\epsilon(t)$ , the system only provides its amplitude,  $\epsilon_0$ . During the measurement, a.c. and d.c. function generators send a signal to a force generator. These forces are transferred to the sample

### 3.2 Dynamic mechanical analysis

by a probe in the form of stress and a differential transformer detects the strain of the sample. Schematic shape of holder set-up for single-cantilever mode is shown in Figure 3.2.

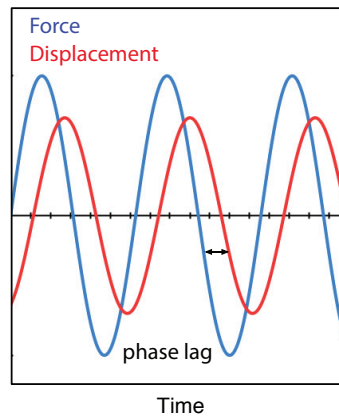


Figure 3.1 Schematics of the applied stress, the resulting strain and the phase lag in DMA

One advantage of Pyris Diamond DMA is its ability to obtain a modulus each time a sine wave is applied which makes it possible to sweep across a temperature or/and frequency range.

The simplest method to collect frequency data is to hold the temperature constant and scan several frequencies during temperature change. As long as the frequencies are high enough (0.1 Hz and above) and the heating rate is low (2-5 °/min), the temperature should be constant for the data collection. In this study, samples were ceramic bars with desired composition and the dimension of 50x5x1 mm. Oscillating load of 1 N was applied at frequency of 0.2, 2 and 20 Hz. Heating/cooling rates were 2°/min. The temperature was changed from -100°C to 200°C and measurements were done both during cooling and heating.

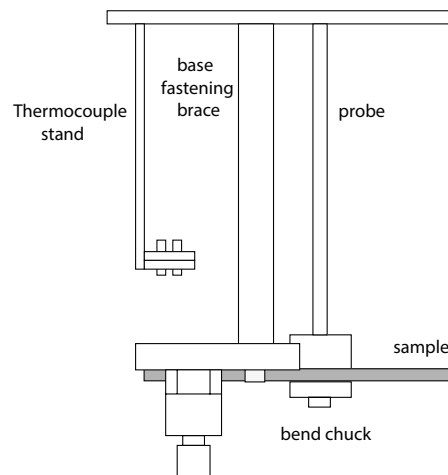


Figure 3.2 Pyris Diamond sample holder in single-cantilever mode (taken from the machine's manual)

### 3.3 Dielectric nonlinear harmonic analysis

In order to study in more details the dielectric permittivity response of material to sub-switching applied electric fields, the lock-in technique was used (Figure 3.3). The input voltage ( $V_{in}$ ) was generated by a Stanford lock-in amplifier (SR 830) and amplified by a Krohn-Hite 7602M wideband power amplifier. The output signal ( $V_{out}$ ), measured by the same lock-in, was synchronized with the input sinusoidal voltage. The amplitude of  $V_{out}$  should be within the range of the lock-in's voltage detector sensitivity. The testing sample is represented in the circuit schematic by capacitor  $C_s$ . A resistor,  $R$  is put in series with sample. If  $R \ll 1/\omega C_s$  ( $\omega$  is angular frequency,  $\omega=2\pi f$ ), the resistor would be a tool to measure the current determined by the voltage dropped across the capacitor [2]. 100  $\Omega$  to 10 K  $\Omega$  were typical range of used resistors.

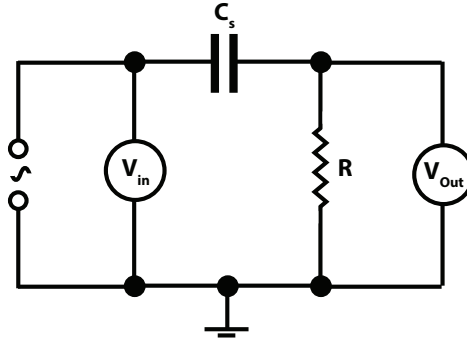


Figure 3.3 Schematic circuit for nonlinear measurement

Considering the input voltage

$$V_{in}(t) = V_0 \sin(\omega t) \quad 3.4$$

The impedance equation for a RC circuit is as following:

$$I = \frac{V_{in}}{Z}, Z = \sqrt{R^2 + (1/\omega C)^2} \quad 3.5$$

$$V_{out} = I(t)R = R \frac{V_{in}}{Z} \quad 3.6$$

If  $R \ll 1/\omega C_s$ , then:

$$C_s = \frac{V_{out}}{V_{in}} \times \frac{1}{\omega R \times N} \quad 3.7$$

### 3.3 Dielectric nonlinear harmonic analysis

Where N is the number of harmonic, since the measurement is done at a fixed frequency of 1KHz ( $f=\omega/2\pi$ ), knowing the sample's area and thickness (A and d), the dielectric permittivity can be calculated from obtained  $C_s$  values.

It is possible to decompose any signal, which is function of time into the frequencies that construct the signal (higher harmonics) by Fourier transform. Derivation of polarization's Fourier components from amplitudes and phase angles of the measured current is explained below:

For polarization response  $P(E)$ , described by any nonlinear function, Fourier series in the general case is:

$$P(t) = P_0 + \sum_{n=1,2,3...} (P'_n \sin(n\omega t) + P''_n \cos(n\omega t)) \quad 3.8$$

The current  $I(t)$  is the result of sample polarization, so it can be expressed as:

$$I(t) = \frac{\partial Q(t)}{\partial t} \approx A \frac{\partial P}{\partial t} = \sum_{n=1,2,3...} (An\omega P'_n \cos(n\omega t) - An\omega P''_n \sin(n\omega t)) \quad 3.9$$

On the other hand, the lock-in amplifier detects voltage  $V_{out}$  as amplitudes ( $V_{n0}$ ) and phase angles ( $\varphi_n$ ) of several first harmonics with respect to the phase and frequency of input signal  $V_{in}$ , hence  $V_{out}$  is composed as:

$$V_{out}(t) = \sum_{n=1,2,3...} (V_{n0} \sin(n\omega t) \cos\varphi_n + V_{n0} \cos(n\omega t) \sin\varphi_n) \quad 3.10$$

The circuit current is in-phase with the measured voltage and as mentioned before if  $R \ll 1/\omega C$ , it is calculated from  $V_{out} = R \times I$ . So by dividing equation 3.11 by R we would have:

$$\frac{V_{out}(t)}{R} = I(t) = \sum_{n=1,2,3...} \left( \frac{V_{n0} \cos\varphi_n}{R} \sin(n\omega t) + \frac{V_{n0} \sin\varphi_n}{R} \cos(n\omega t) \right) \quad 3.11$$

Also it is possible to write current and it's Fourier transform as follow (current is in phase with  $V_{out}$ ):

$$I(t) = I_0 \sin(\omega t + \varphi) = \sum_{n=1,2,3...} (I'_n \sin(n\omega t) + I''_n \cos(n\omega t)) \quad 3.12$$

From (3.7) and (3.10) we have:

$$I'_n = \frac{V_{n0}}{R} \cos\varphi_n, I''_n = \frac{V_{n0}}{R} \sin\varphi_n \quad 3.13$$

Comparing (3.13), (3.12) and (3.9) the complex Fourier components of polarization can be calculated through experimentally measured voltage and phase angle:

$$\begin{aligned} P_n' &= \frac{I_n''}{An\omega} = \frac{V_{n0}}{An\omega R} \sin\varphi_n \\ P_n'' &= \frac{-I_n'}{An\omega} = \frac{-V_{n0}}{An\omega R} \cos\varphi_n, \\ \varepsilon_n &= \frac{P_n'}{E_0} \end{aligned} \quad 3.14$$

The primed components are in-phase with the source signal and describe the real part of the complex amplitude. The double-primed components are out of phase with the driving field, describing imaginary part of the complex value. It is shown by equations 3.13 and 3.14 that amplitudes of polarization and current have 90° phase shift with respect to each other.

### 3.4 Pyroelectric measurement

Materials with spontaneous polarization have the property of altering polarization with temperature change. This phenomenon is called pyroelectricity and it's a first rank tensor, defining as below:

$$\delta P_i = p_i \delta T \quad 3.15$$

Where P is polarization, T is temperature and  $p_i$  is the pyroelectric coefficient[3, 4]. Under constant electric field E, the pyroelectric coefficient could be also written as:

$$p_i^\sigma = \left( \frac{\partial P_i}{\partial T} \right)_\sigma \quad 3.16$$

Theoretically pyroelectricity can be measured by determining the surface charge Q over the sample surface area A. So, 3.16 can be expressed as:

$$p = \left( \frac{\partial (Q/A)}{\partial T} \right)_{\sigma, E} = \frac{1}{A} \left( \frac{\partial Q}{\partial T} \right)_{\sigma, E} - \frac{Q}{A^2} \left( \frac{\partial A}{\partial T} \right)_{\sigma, E} \quad 3.17$$

By ignoring the change of area with respect to temperature, p becomes:

$$p = \frac{1}{A} \left( \frac{\partial Q}{\partial T} \right)_{\sigma, E} \quad 3.18$$

As shown in Figure 3.4 when a sample is heated, its polarization change can be monitored with two different measurements circuit. Measuring the voltage V across a reference capacitor C, or the current through a reference resistor R, both generated in sample by pyroelectricity.

### 3.4 Pyroelectric measurement

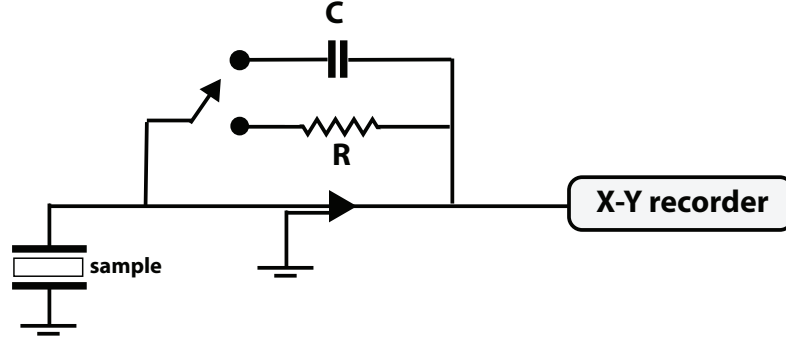


Figure 3.4 Two different methods for pyroelectric measurement [3].

According to 3.20, pyroelectric coefficient is calculated as following for each method:

$$p = \frac{i_p}{A \left( \frac{dT}{dt} \right)} \quad [C/m^2K] \quad 3.19$$

$$p = \frac{C_0}{A} \frac{dV}{dT} \quad [C/m^2K] \quad 3.20$$

Our set-up measures pyroelectric current  $i_p$ . Equation 3.19 is widely considered as the definition of the measured pyroelectric coefficient. This experiment can be done in two different ways mechanically: constant strain  $X$  (clamped condition) or constant stress  $\sigma$  (free expansion condition). For the first case the observed effect is called primary pyroelectricity. In the second case, which is much easier to perform, there is an additional secondary pyroelectricity, which involves piezoelectricity [3]. Experimentally it is problematic to measure separately each component, so what is measured in 3.21 (total coefficient  $p_{total}$ ) is considered sufficient and contain both primary and secondary components:

$$p_{total} = \left( \frac{\partial D}{\partial T} \right)_{X,E} + \left( \frac{\partial D}{\partial X} \right)_{E,T} \left( \frac{\partial X}{\partial T} \right)_{\sigma,E} \quad 3.21$$

An important factor during pyroelectric measurement is the necessity for uniform heating of sample during both qualitative and quantitative pyroelectric measurements. If the temperature is not the same in different parts of piezoelectric specimen the temperature gradient results in polarization and consequently an additional pyroelectric effect. This effect is called "tertiary" or "false" pyroelectricity [4, 5].

Lang [6] has divided pyroelectric measurement techniques into three categories: static, indirect and dynamic. In static methods the specimen is subjected to an incremental temperature change and charge displacement is measured; measurements are only taken at discrete temperatures. These methods are rarely used because they are time consuming. Indirect methods use measurement of related parameters such as polarization to determine pyroelectric coefficient.



Dynamic methods are the most widely used ones and involve pyroelectric coefficient measurement by continuous variation of sample temperature. Most important techniques for each method are given in Table 3.1.

Table 3.1 Different techniques for pyroelectric measurements

Static	Indirect	Dynamic
Heat-burst method [7]	E-P measurements (Sawyer-Tower) with temperature [8]	Linear temperature-ramp (Byer-Roundy) method [9]
	Electrocaloric method [10]	Modulated radiant heating (Chynoweth) method [11]
		Temperature oscillation or a.c. method [12]
		Shunt-resistor method [13]
		Charge –integration method [14]
		Step-radiation method [15]

We have used the a.c. method, which is recommended as the standard technique for pyroelectric measurement [5, 12]. In this method as illustrated in Figure 3.5 a Peltier device modulates the temperature in a regular periodic fashion (triangular or sinusoidal wave) whilst the current is recorded. Temperature is cycled at low frequency (10 to 100 mHz) with the amplitude of 1-3 K peak to peak. Temperature is regulated by a Pt 100 resistance temperature detector RTD, placed close to the sample. Pt RTD works based on resistance variation of platinum at different temperatures (platinum has a resistance of 100 ohm at 0°C). A HP 3478A multimeter reads the Pt 100's temperature. An additional thermocouple provides feedback for the system. The sample holder is located on top of a copper plate, which was placed over the Peltier element. The pyroelectric current produced by temperature variation is sent to Dyno Pyro III (a home made control module) where it is electronically converted into voltage and amplified. Output voltage is read with another HP 3478A multimeter. A Labview program controls the whole set up and record the data.

In this method, the pyroelectric coefficient is calculated by measuring the reversible sample current and the differential of sample temperature using equation (3.21). It has many advantages over other methods: It's capable of distinguishing between reversible pyroelectric current and irreversible thermally stimulated current responses. It is possible to apply d.c. electric fields during measurement. Experiments could be done at discrete or during continuous ramping of temperature. It's able to study frequency dependence of pyroelectric response. It is precise and reliable (better than 1%, typically  $0.1 \mu\text{C}/\text{m}^2\text{K}$ ). Also, it is straightforward to study the time dependence and stabilization of pyroelectric response because the reference temperature can be fixed in this technique. Finally, any distortion in current traces could be immediately shown providing useful information. For instance presence of space charges could distort current profile to a saw-tooth shape [5].

### 3.4 Pyroelectric measurement

To avoid problems related with nonhomogeneous heating of specimens, some dimension limitations were applied to disk shape samples. Sample's thicknesses were between 0.5-0.6 mm and diameters were about 6mm.

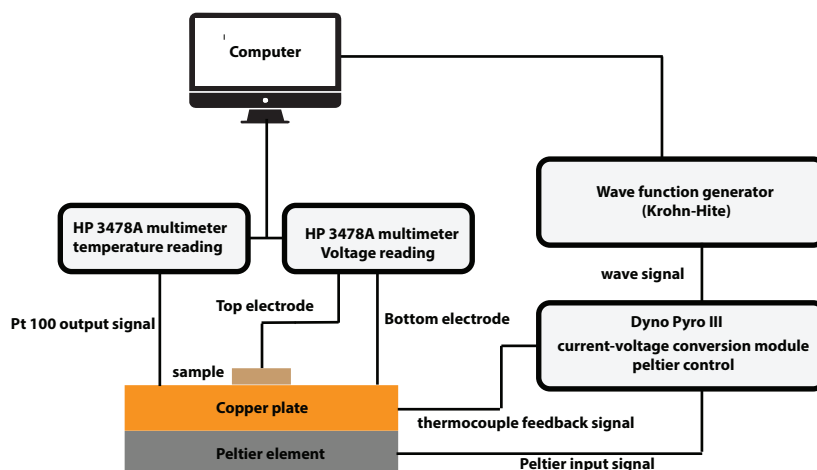


Figure 3.5 Schematics of pyroelectric measurement set-up [5].

Figure 3.6 represents the typical pyroelectric response to an applied triangular wave in a unpoled barium titanate ceramic (nonzero current suggests that domains are not perfectly averaged to give a zero polarization). The pyroelectric current has direction, meaning it changes its phase by  $180^\circ$  with respect to the temperature oscillation when the sample is inverted. We have used this method to identify the presence or absence of macroscopic symmetry breaking in our samples.

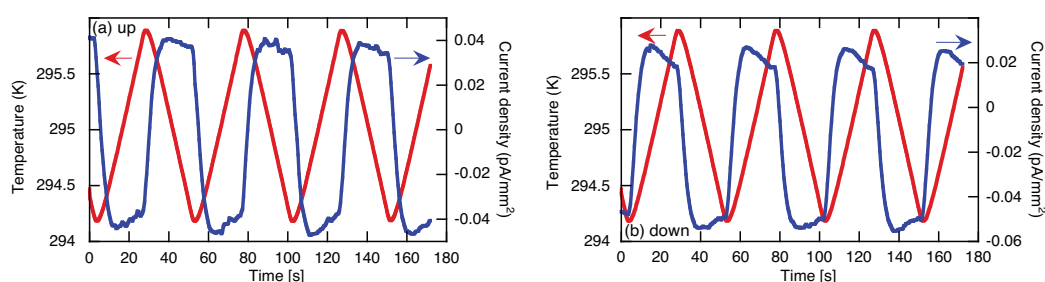


Figure 3.6 Typical pyroelectric response for ferroelectric  $\text{BaTiO}_3$  sample. Current is inversed when sample is flipped.

As mentioned in section 1.7, the macroscopic symmetry breaking could arise from different possible origins. It should be clarified at the beginning that observed polarity does not emerged from the surface conditions or/and presence of grain boundaries in our samples and this

measuring technique is able to help us achieve our goal of detecting the macroscopic polarity in the samples. Grain boundaries in ceramics considered as extrinsic defects compared to ideal lattice and are favored locations for charged defects (oxygen vacancies, space charges, etc.) [16]. Polarization in ferroelectric ceramics may affect the state of defects at the grain boundaries [17] leading to symmetry breaking. Biancoli [18] has shown that only granular nature of the ceramic by itself is not adequate to explain pyroelectric response. The absence of pyroelectric current in ceramics of strontium titanate and also presence of pyroelectric response in single crystal of barium titanate above its Curie temperature govern this claim. In that work, surface conditions were also excluded as a possible origin for the symmetry breaking as discussed in section 1.7.

### 3.5 Thermally stimulated current measurement

Thermally stimulated process (TSP) is a term used for a process in which a sample is heated in a controlled manner whilst a specific physical property is monitored as a function of time or temperature. This definition of TSP covers several phenomena such as thermally stimulated depolarization (TSD), thermoluminescence (TL), thermally stimulated conductivity (TSC), thermally stimulated electron emission (TSEE) and etc. In some of these methods the desired property appears when the sample has been excited or treated in a certain way before heating. Different TSPs are due to the different mechanisms but their measured thermograms are interestingly similar. A typical thermogram consists of one or more peaks related to a certain thermally activated microscopic mechanisms. It's possible to study these mechanisms from number, shape and position of the peaks and from dependence of the whole curve on the heating rate, sample history and etc. [19].

For this study we have used a modified version of TSD. It is simply called thermally stimulated current (TSC) measurement. TSC first demonstrated by Frei and Groetzinger [20] but it was Bucci and Fieschi [21] who established the theoretical basis of TSC method for the first time. In classical TSD a sample is electrically polarized from high temperature to the low temperature  $T_0$ , under an external electric field. Existing defects form a metastable state of charge or dipole distribution. At  $T_0$  the electric field is removed and the sample (electret) is heated up. At some high temperatures if the dipoles become free to rotate their motion to equilibrium causes the depolarization and consequently results in a current peak.

The way we used TSC technique is substantially different from classical approach, which usually involves excitation of the material with electric field to study dipole relaxation in polymers [22] or defect dipoles [21] in ionic solids. External electromagnetic radiation is also used for characterization of the trap levels in semiconductors [23]. For our experiments we have never used smallest electric field to excite samples. Observation of TSC in non-polarized materials such as Teflon has been reported before [21] but the theory of TSC in non poled materials has not been developed.

There are also other mechanisms that could be involved as origin of TSC peaks like space charge polarization. Space charge could be related to: i) field induced migration of intrinsic free charge carriers toward electrodes; ii) displacement of ionic defects over macroscopic scales and their trapping at interfaces such as electrodes and grain boundaries (Maxwell-Wagner effect). iii) electron injection from electrodes to the sample. Another source of TSC is temperature dependence of the spontaneous polarization in polar materials. Sign of the current due to pyroelectricity and the mechanisms mentioned above depends on the sample orientation. On the other hand there are other sources of TSC in which sign of the current is not related to how sample

### 3.5 Thermally stimulated current measurement

is placed. TSC produced by thermal gradient inside the sample through Seebeck effect [24] or small voltage of the picoammeter [25] are placed in such category.

Considering all the possible sources of TSC mentioned above, interpretation and analysis of each TSC peak to find its origin is not straightforward. In this study we used this method to check polarity and symmetry breaking of samples and studying the mechanisms behind the peaks are not a goal of the study.

TSC measurements were made by the set-up shown in Figure 3.7. Samples were heated at constant temperature rate of 2.5 °C/min in a controlled hot plate. A Keithley 648 picoammeter measured the current released by the sample. To secure a uniform heating, suitable thermal conductivity and electrical isolation between samples and hot plate, samples were put on top of a platinum foil, which was placed on top a sapphire disk. An external thermocouple was connected to sapphire disk near the sample to measure the temperature. The whole set-up was controlled by a Labview program that recorded the data as well.

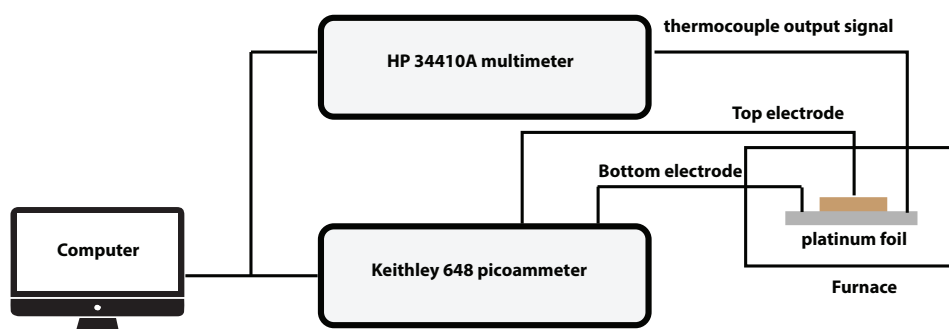


Figure 3.7 Thermally stimulated current measurement set-up

Biancoli [18] has done the TSC measurement with same setup upon heating and cooling from 300 K to 800 K without any sample (open circuit condition) to investigate possible artifacts of system and also estimate the magnitude of background current. As shown in Figure 3.8 no anomalies are present however there is some noise caused by the electrical interference from the heating system. During cooling below 200°C when the power regulator is off, this noise is absent.

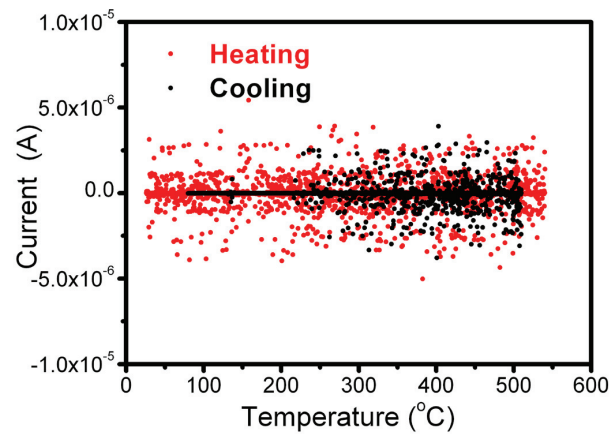


Figure 3.8 Thermally stimulated current measured during heating and cooling under open circuit [18].

The experimental conditions and set-up used for dielectric permittivity measurements are described in chapter 2 (section 2.9). Electron microscopy studies carried out for microstructural characterization of ceramics and also atomic resolution study of polar regions are explained in details in chapter 2 and chapter 7 respectively.

## Bibliography

- [1] K. P. Menard, *Dynamic mechanical analysis: a practical introduction*: CRC press, 2008.
- [2] M. Morozov, "Softening and hardening transitions in ferroelectric Pb (Zr, Ti) O<sub>3</sub> ceramics," ÉCOLE POLYTECHNIQUE FÉDÉRALE DE LAUSANNE, 2005.
- [3] R. E. Newnham, *Properties of materials: anisotropy, symmetry, structure*: Oxford University Press on Demand, 2005.
- [4] J. F. Nye, *Physical properties of crystals: their representation by tensors and matrices*: Oxford university press, 1985.
- [5] M. Daglish, "A dynamic method for determining the pyroelectric response of thin films," *Integrated Ferroelectrics*, vol. 22, pp. 473-488, 1998.
- [6] S. B. Lang, *Sourcebook of pyroelectricity* vol. 2: CRC Press, 1974.
- [7] W. Ackermann, *Am. Phys. (Leipzig)*, vol. 46, 1915.
- [8] C. B. Sawyer and C. Tower, "Rochelle salt as a dielectric," *Physical review*, vol. 35, p. 269, 1930.
- [9] R. L. Byer and C. Roundy, "Pyroelectric coefficient direct measurement technique and application to a nsec response time detector," *Ferroelectrics*, vol. 3, pp. 333-338, 1972.
- [10] G. G. Wiseman, *NASA report*, vol. CR-1080, 1967.
- [11] A. Chynoweth, "Dynamic method for measuring the pyroelectric effect with special reference to barium titanate," *Journal of applied physics*, vol. 27, pp. 78-84, 1956.
- [12] N. Hartley, P. Squire, and E. Putley, "A new method of measuring pyroelectric coefficients," *Journal of Physics E: Scientific Instruments*, vol. 5, p. 787, 1972.
- [13] S. B. Lang and F. Steckel, "Method for the measurement of the pyroelectric coefficient, dc dielectric constant, and volume resistivity of a polar material," *Review of Scientific Instruments*, vol. 36, pp. 929-932, 1965.
- [14] A. Glass, "Investigation of the electrical properties of Sr<sub>1-x</sub>Ba<sub>x</sub>Nb<sub>2</sub>O<sub>6</sub> with special reference to pyroelectric detection," *Journal of Applied Physics*, vol. 40, pp. 4699-4713, 1969.
- [15] M. Simhony and A. Shaulov, "Pyroelectric Voltage Response to Step Signals of Infrared Radiation in Triglycine Sulphate and Strontium - Barium Niobate," *Journal of Applied Physics*, vol. 42, pp. 3741-3744, 1971.
- [16] M. E. Lines and A. M. Glass, *Principles and applications of ferroelectrics and related materials*: Oxford university press, 1977.
- [17] J. Daniels, K. Härdtl, and R. Wernicke, "The PTC effect of barium titanate," *Philips Technical Review*, vol. 38, pp. 73-82, 1979.
- [18] A. Biancoli, "Breaking of the macroscopic centric symmetry in Ba<sub>1-x</sub>Sr<sub>x</sub>TiO<sub>3</sub> ceramics and single crystals," 2014.
- [19] R. Chen and Y. Kirsh, *The analysis of thermally stimulated processes*: Elsevier, 2013.
- [20] H. F. a. G. Groetzinger, *Phys. Z.*, vol. 37, p. 720, 1936.
- [21] C. Bucci, R. Fieschi, and G. Guidi, "Ionic thermocurrents in dielectrics," *Physical Review*, vol. 148, p. 816, 1966.

- [22] J. Van Turnhout, "Thermally stimulated discharge of polymer electrets," *Polymer Journal*, vol. 2, pp. 173-191, 1971.
- [23] U. V. Desnica and B. Šantić, "Optically enhanced photoconductivity in semi - insulating gallium arsenide," *Applied physics letters*, vol. 54, pp. 810-812, 1989.
- [24] W. Lau, K. Wong, T. Han, and N. P. Sandler, "Application of zero-temperature-gradient zero-bias thermally stimulated current spectroscopy to ultrathin high-dielectric-constant insulator film characterization," *Applied physics letters*, vol. 88, p. 172906, 2006.
- [25] W. S. Lau, T. C. Chong, L. S. Tan, C. H. Goo, and K. S. Goh, "The characterization of traps in semi-insulating gallium arsenide buffer layers grown at low temperature by molecular beam epitaxy with an improved zero-bias thermally stimulated current technique," *Japanese journal of applied physics*, vol. 30, p. L1843, 1991.





## Chapter 4. Symmetry breaking in hexagonal and cubic polymorphs of BaTiO<sub>3</sub>

### 4.1 Introduction

In the first part of this chapter the crystal structures and synthesis conditions of hexagonal and perovskite barium titanate (h-BTO and p-BTO respectively) are discussed. Next, symmetry breaking is investigated for h-BTO and p-BTO. Both the cubic and the hexagonal variants of BTO are centrosymmetric. Cubic BaTiO<sub>3</sub> is known to exhibit breaking of the centric symmetry locally [1] and globally [2, 3]. Such data are not available for BaTiO<sub>3</sub> with hexagonal symmetry. The aim of this chapter is to investigate possible origins of the symmetry breaking in the paraelectric phase of archetypal ferroelectric, BaTiO<sub>3</sub>. We compared dielectric, elastic, and pyroelectric properties of the two materials in polycrystalline form to distinguish between charged defects and polar regions models as possible origins of the macroscopic symmetry breaking.

p-BTO experiences a series of phase transitions from the high temperature centrosymmetric paraelectric-paraelastic cubic phase to a tetragonal phase at  $T_C \approx 473$  K, orthorhombic phase at  $\approx 278$  K and rhombohedral phase at  $\approx 183$  K, all of which are ferroelectric-ferroelastic, with polarization as the order parameter [4]. h-BTO becomes ferroelectric-ferroelastic below  $T_C \approx 60-74$  K, [5-7] possibly possessing a monoclinic structure and exhibiting ferroelectric polarization that is about one order of magnitude smaller than in ferroelectric phases of p-BTO [7-12]. The order parameter in the ferroelectric-ferroelastic phase of h-BTO appears to be strain [9]. So it's rational to expect that h-BTO should not exhibit polar regions at room temperature or at least polarization of polar regions and their effect on properties should be much smaller compared to paraelectric phase of p-BTO.

Considering the assumption that processing conditions and material parameters like the concentration and nature of charged defects are similar for the two materials, absence of properties related to polar structure in h-BTO above Curie temperature and their presence in p-BTO above its  $T_C$  would support models linking broken symmetry in p-BTO to the polar regions rather than to charged point defects. The work presented in this Chapter has been published in Ref. [13].

### 4.2 Crystal structure of hexagonal and perovskite BaTiO<sub>3</sub>

Several perovskite (ABO<sub>3</sub>) oxides, where A is a large cation like Ba and B is a small cation belonging to the d-transition metals, are known to exhibit polytypism (Figure 4.1). These oxides consist of stacked close-packed, AO<sub>3</sub> layers, with B cations occupying all the interlayer oxygen octahedra. The AO<sub>3</sub> layers stacking may be cubic (c) or hexagonal (h) with respect to its two adjacent layers, depending on whether it is in the middle of ABA or ABC sequence. In case of complete cubic perovskite structure (3C), the B-cation octahedra share only corners in three dimensions. In the all-hexagonal case (2H), the B-cation octahedra share opposite faces creating chains along the c-axis. In between the two extreme cases, several polytypic structures may exist containing mixed cubic and hexagonal stacking of AO<sub>3</sub> layers. For example, the 6H and 4H

## 4.2 Crystal structure of hexagonal and perovskite BaTiO<sub>3</sub>

polytypes have “c-h-c-c-h-c” and “c-h-c-h” stacking sequences respectively [14]. Figure 4.1 shows schematic of different polytypes of perovskites.

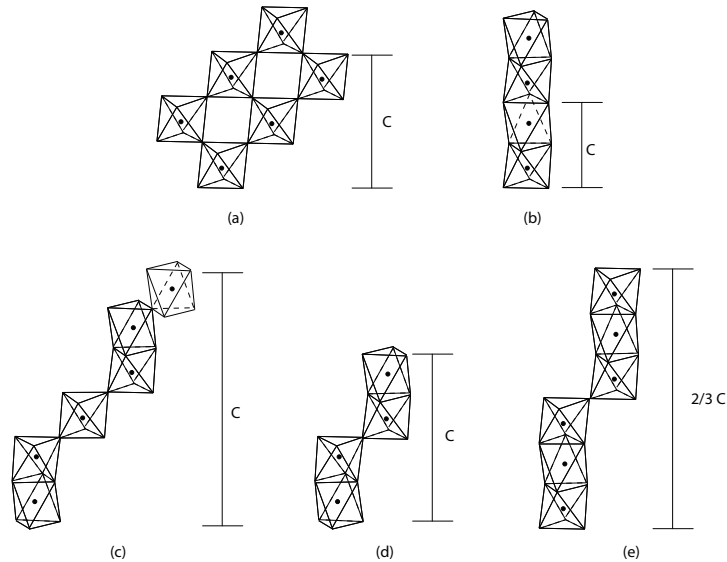


Figure 4.1 Different stacking of BO<sub>6</sub> octahedra in ABO<sub>3</sub> perovskite polytypes: a) 3C; b) 2H; c) 6H; d) 4H; and e) 9R. (a) and (b) represent complete cubic and all hexagonal structures [14].

Evans et al. [15, 16] studied the single crystal of h-BTO by XRD and demonstrated a similarity in crystal structures between the h-BaTiO<sub>3</sub> and the p-BaTiO<sub>3</sub>. They have found out that hexagonal cell fits almost exactly into cubic lattice. It means that hexagonal polymorph consists of closed packed BaO<sub>3</sub> layers of atoms. Assume a two-dimensional ionic sheets containing one part of Ba and three parts of oxygen ions. To make the close pack structure, it is convenient to consider three types of equivalent layers: A, B, C as shown in Figure 4.2. Stacking sequence of “B-C-A” results in atomic arrangement for perovskite structure, while hexagonal barium titanate is made by “A-B-A-C-B-C” sequence [17].

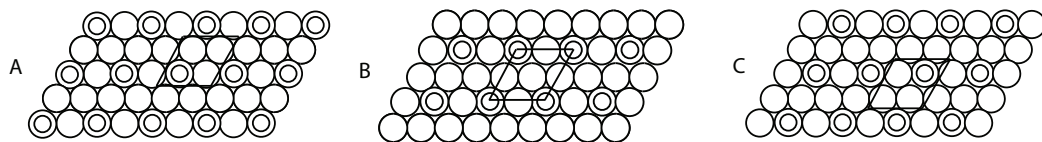


Figure 4.2 Three kinds of close-packed equivalent sheets (A, B and C) consisting one part of barium ions (double circles), and three parts of oxygen ions (open circles). The location of titanium ions is deleted in the figure; Ti ions are sandwiched between every neighboring pair of the Ba-O sheets and are accommodated in small holes formed by six oxygens to form TiO<sub>6</sub> octahedron. Solid lines show outlines of the hexagonal unit cell project on the sheets [17].

As presented in Figure 4.3 the two structures differ only in the manner of BaO<sub>6</sub> close packing. Hexagonal barium titanate has a 6h-hexagonal structure with partly face sharing and partly corner sharing octahedra [18], while perovskite structure has corner sharing octahedral.

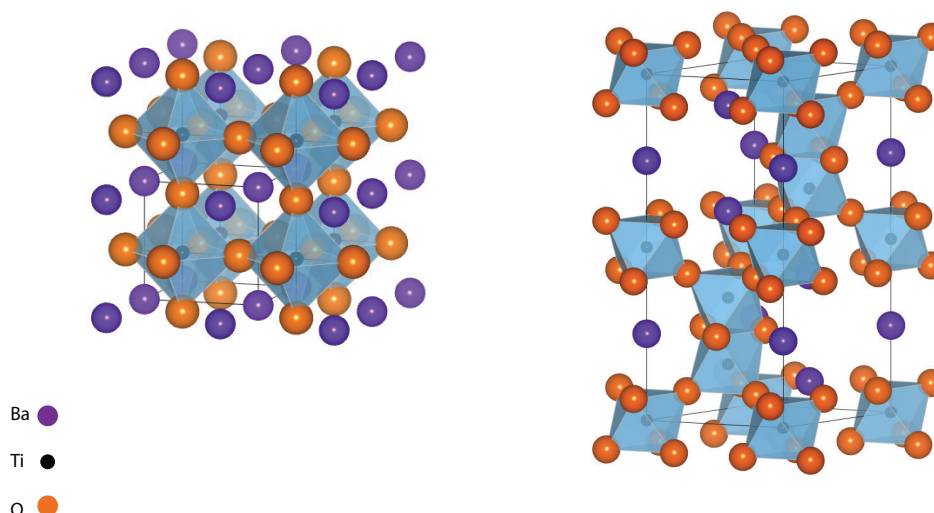


Figure 4.3 Crystal structures of perovskite (left) and hexagonal (right graph) barium titanate. Purple atoms are Ba, orange atoms are oxygen and black atoms are Ti.

### 4.3 Synthesis of apparently pure (single phase) hexagonal barium titanate

As illustrated in BaO-TiO<sub>2</sub> phase diagram (Figure 2.1) the hexagonal polymorph is only stable above 1733 K. However, it can be persevered metastably at room temperature. Different studies reported the influence of reducing sintering condition on hexagonal phase formation [19-21]. Moreover, Glaister [19] showed that doping with Mn, Fe and Ni has an effect similar to sintering in reducing atmosphere on cubic to hexagonal transition and lowering the cubic to hexagonal transition temperature down to 1603 K in a hydrogen atmosphere. Wakamatus et al. also [21] confirmed that the fraction of tetragonal to hexagonal phase conversion could be increased by decreasing the partial pressure of oxygen.

Interestingly, we were able to stabilize high quality pure h-BTO ceramics at room temperature by sintering in air and without any dopants. XRD and dielectric data were fully consistent with what were reported in the literature (see chapter2). Moreover, Andreja Bencan and Goran Drazic from Electronic Ceramics Department of Jozef Stefan institute have performed TEM/STEM (scanning transmission electron microscopy) analysis to study in more details the microstructure and stoichiometry of the h-BTO ceramics. Figure 4.4 (a) and (b) show high-angle annular dark-field (HAADF) and its corresponding annular bright-field (ABF) STEM images of h-BTO, respectively. Diffraction pattern obtained from Fourier transform of TEM images confirms the hexagonal phase. Positions of Ba, Ti and O atomic columns are marked with red arrows on the atomic resolution images.

#### 4.3 Synthesis of apparently pure (single phase) hexagonal barium titanate

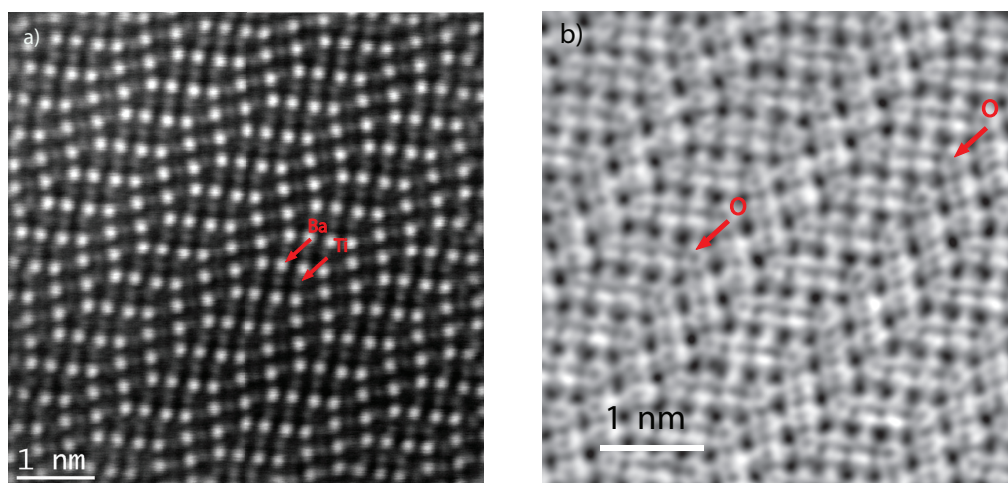


Figure 4.4 a) HAADF, b) ABF STEM image of h-BTO, positions of Ba, Ti and O atoms are marked with red arrows. Courtesy of Andreja Bencan, JSI and Goran Drazic, NIC.

It's reported in the literature that quantity of  $\text{Ti}^{+3}$  cations increases with the amount of hexagonal phase and  $\text{Ti}^{+3}$  ions occupy  $\text{Ti}^{+4}$  sites in the coordination groups in h-BTO [15, 21]. Valence state of Ti in hexagonal phase was also studied in this work to see if it is consistent with literature. Figure 4.5 represents standard EELS spectra of  $\text{Ti}^{+4}$  and  $\text{Ti}^{+3}$  in  $\text{TiO}_2$  (provided by Drazic). These spectra were used as reference to identify the valence of Ti in our h-BTO samples.

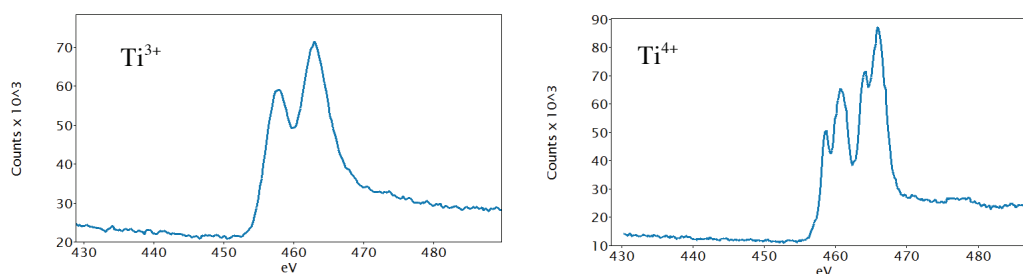


Figure 4.5 Standard experimental EELS spectra for Ti with different valence state in  $\text{TiO}_2$  provided by Drazic.

Figure 4.6 (c) and (d) shows simulated atomic structure of two hexagonal polymorphs, i.e.  $\text{BaTiO}_3$  and  $\text{BaTiO}_{2.83}$ . Valence of Ti in  $\text{BaTiO}_{2.83}$  is  $\text{Ti}^{3+}$  on  $\text{Ti}_1$  marked positions and is  $\text{Ti}^{4+}$  in case of  $\text{BaTiO}_3$ . Comparing EELS analysis data on hexagonal BTO samples (Figure 4.6 (b)) with standard data provided in Figure 4.5 revealed that valence of Ti is 4+ in its crystallographic positions (circled atoms). According to the model we can conclude that we synthesized stoichiometric hexagonal barium titanate. This is unexpected because all of the studies reported in the literature used methods to stabilize hexagonal phase that leads to a higher concentration of oxygen vacancies and formation of reduced titanium.

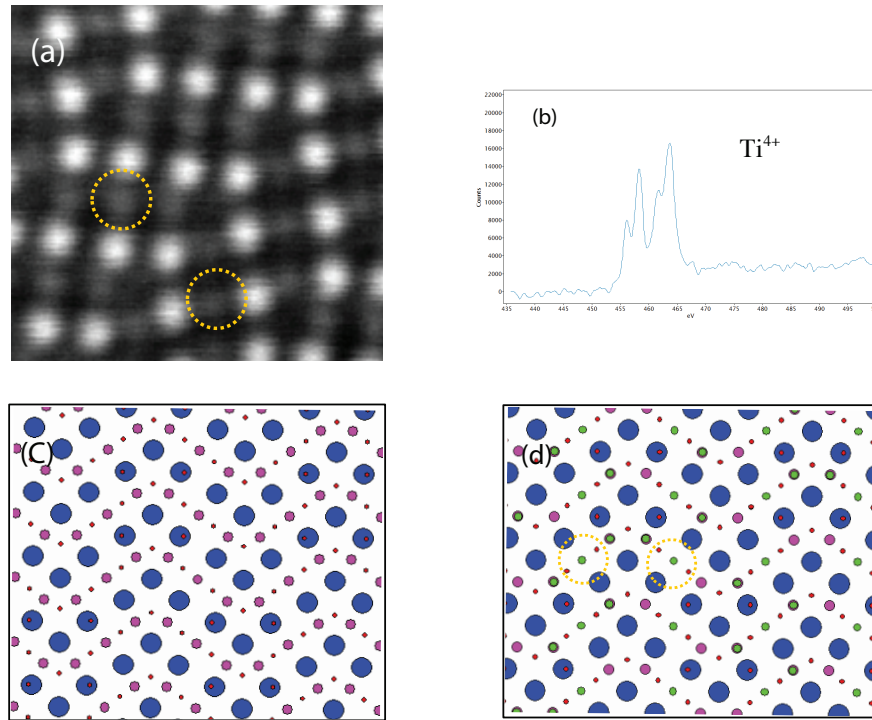


Figure 4.6 a) image taken for valence study of Ti (circled positions are titanium atoms), b) EELS spectra measured for h-BTO, c) ICSD model for BaTiO<sub>3</sub> image taken for valence study of Ti (circled positions are titanium atoms), d) ICSD model for BaTiO<sub>2.83</sub>. Courtesy of Andreja Bencan, JSI and Goran Drazic, NIC.

p-BTO and h-BTO were synthesized from the same powder (with the tetragonal structure at room temperature) with slight differences in processing conditions. For fabrication of h-BTO, there was no milling step of precursor and sintering temperature was 1773 K (50 K higher than p-BTO). Since the chemistry of precursor is the same for h-BTO and p-BTO, retention of h-BTO should be related to milling process and/or sintering temperature. Experiments with different combination of sintering temperature and milling step were designed systematically to find out the mechanism governing hexagonal phase formation at room temperature. XRD, dielectric permittivity measurement and transmission electron microscopy were used to study the BTO phase formation. Table 4.1 presents 5 different case studies:

Table 4.1 Different processing conditions used to study hexagonal phase retention of barium titanate at room temperature

no milling+ sintering at 1623 K	tetragonal
no milling+ sintering at 1723 K	hexagonal+tetragonal
no milling+ sintering at 1773 K	fully hexagonal
milling+ sintering at 1723 K	tetragonal
milling+ sintering at 1773 K	tetragonal

#### 4.3 Synthesis of apparently pure (single phase) hexagonal barium titanate

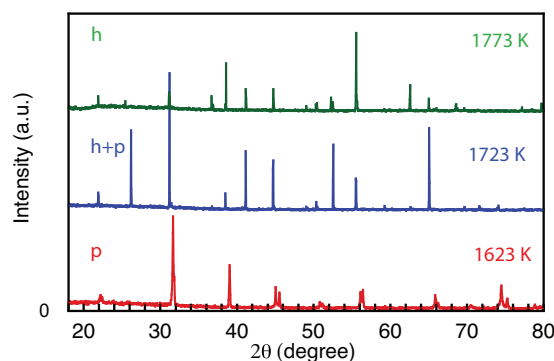


Figure 4.7 XRD spectra of ceramics pressed from unmilled powder sintered at three different temperatures.

XRD data (Figure 4.7) for pellets pressed from unmilled powder sintered at three different temperatures show that, 100% hexagonal phase is only obtained by sintering at 1773 K. Firing at 1723 K results in a mixture of hexagonal and perovskite phase, as proved by XRD and observation of small anomalies in the dielectric permittivity (Figure 4.8) exactly at temperatures associated with the tetragonal BTO phase transitions. Sample sintered at 1623 K was tetragonal because at this temperature material never experienced cubic to hexagonal phase transition. Using milled powder results in tetragonal phase formation regardless of sintering temperature.

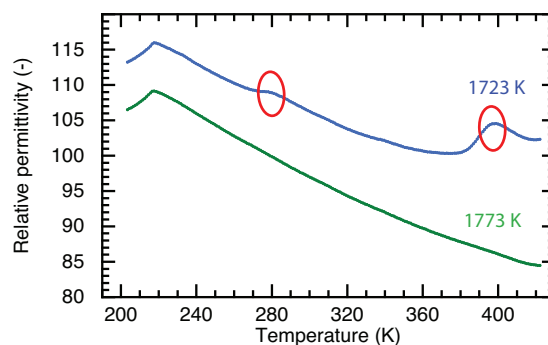


Figure 4.8 Dielectric permittivity of BTO sintered at 1723 K and 1773 K as a function of temperature at 1 kHz shows anomalies around 400 K and 280 K which are characteristic of perovskite barium titanate.

Our data suggest that sintering at temperatures lower than 1773 K does not result in complete cubic to hexagonal transition. The fact that sample fabricated with milled powder at 1773 K is perovskite at room temperature shows that the main cause for preservation of the hexagonal phase at room temperature should be related to the milling process. Therefore, the milled and unmilled powders were investigated. XRD data, Figure 4.9, show that both samples are perovskites (have tetragonal structure) at room temperature and milling has not changed the phase of powders (at least in the scale of XRD detection resolution).

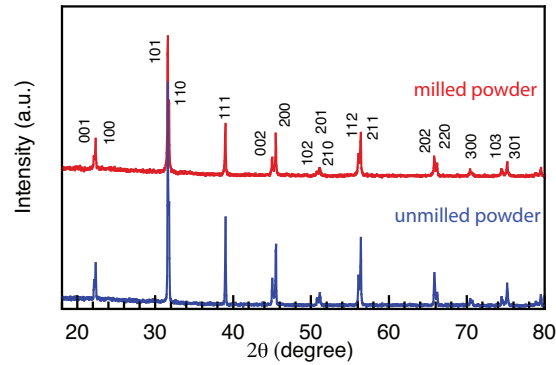


Figure 4.9 XRD spectra of milled and unmilled BTO powder. They both have identical tetragonal (cubic) structure at room temperature.

We speculate that unmilled starting powder possesses some hexagonal phase seeds (not detectable with XRD) that help hexagonal phase to stabilize at room temperature. These seeds may be related to (111) twins in the cubic phase, as described in Ref. [22]. As illustrated in Figure 4.10 the hexagonal phase may be related to the twinned cubic BaTiO<sub>3</sub> [5].

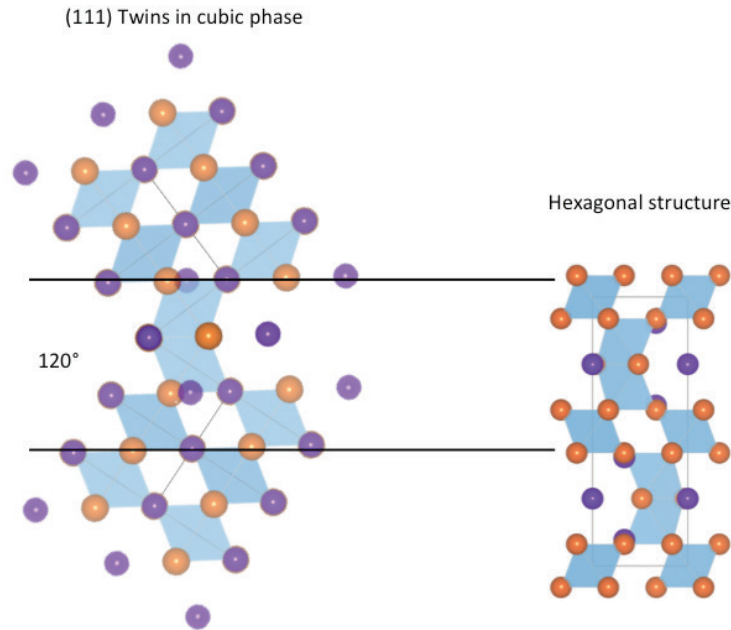


Figure 4.10 Similarity between structures of hexagonal BTO and (111) twin in perovskite BTO.

Milling process could break those seeds, which results in tetragonal phase formation during cooling from the sintering temperature. If the twins are present in the cubic phase, the



### 4.3 Synthesis of apparently pure (single phase) hexagonal barium titanate

hexagonal phase might be retained at room temperature after sintering at temperatures where hexagonal phase is stable. To study validity of this conjecture and the nature of entities that might be responsible for retention of the hexagonal phase, we carried out a TEM study. Figure 4.11 (a) presents HAADF of an unmilled powder grain obtained in [111]-zone axis. No visible planar defects were observed in the studied grain.

Bright field TEM images of unmilled and milled BTO are presented in Figure 4.11 (b) and (c), both powders composed of few hundred nm grains. From the structural point of view (e.g., number of twins or other defects) no difference was observed between the milled and unmilled powders. On the other hand, there are nano-sized grains containing Zr in the milled powder, which are absent in the non-milled powder. Zr is introduced during milling step by Zr milling balls.

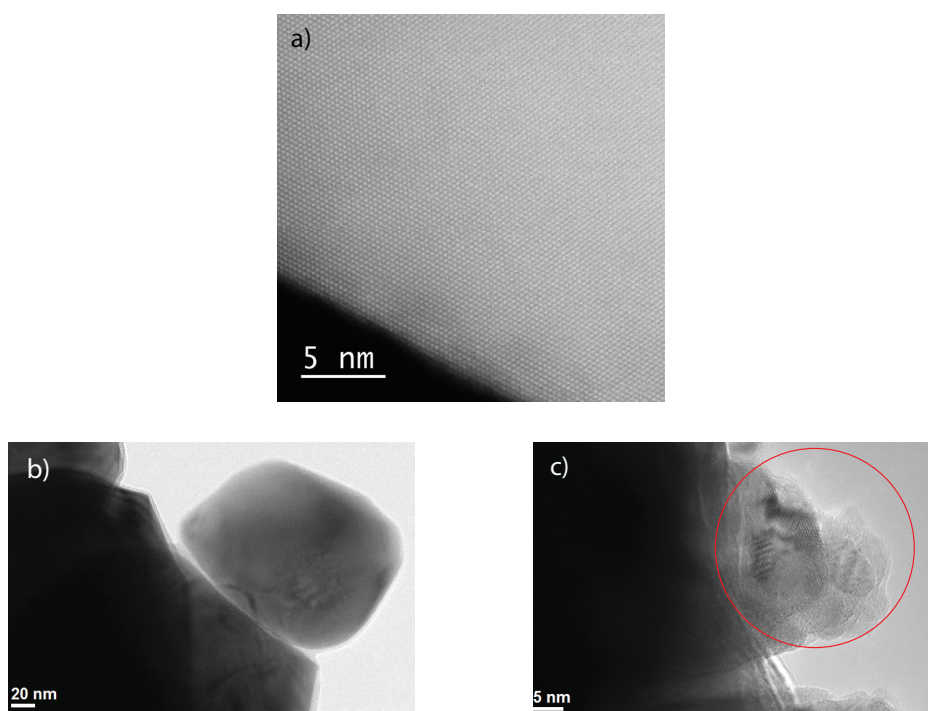


Figure 4.11 a) presents HAADF of an unmilled powder grain obtained in [111] zone axis. Bright field TEM image of (b) unmilled and (c) milled BTO. Courtesy of Andreja Bencan, JSI and Goran Drazic, NIC.

To study the possible effect of Zr on BTO phase formation we sintered samples at 1773 K from milled and unmilled powders provided by another supplier (Alfa Aesar). In both case BTO has perovskite (tetragonal) phase so we believe that the small trace of Zr in milled powder couldn't be the governing mechanism for h-BTO retention at room temperature. The fact that we were not able to observe any significant structural difference (i.e., presence of twin or twins) between the milled and unmilled powder does not imply that the powders are identical. It's possible that the chosen grains for TEM study were the same in both powders. More investigation is needed to identify any possible structural difference, which is out of scope of this thesis.



#### 4.4 Dielectric permittivity as a function of temperature

Figure 4.12(a) and 4.12(b) compare relative unclamped permittivities of p-BTO and h-BTO samples at 1 kHz. The temperature dependences of the measured permittivities are similar to those reported by other authors [5, 17, 23]. According to our measurement maximal permittivity in h-BTO is between 50 and 60 K, while Ref [7] reports  $T_C \approx 74$  K. The inconsistency could be related to the purity of the materials or accuracy of temperature measurements at cryogenic temperatures.

These data can also be considered as a confirmation of XRD data that the two kinds of materials are indeed p- and h-BTO. The peaks in permittivities and dielectric loss correspond to structural phase transitions in these two materials.

Figure 4.12(c) shows dielectric loss for p- and h-BTO. The  $\tan \delta$  at 1 kHz in h-BTO is ten times smaller than the loss in p-BTO. Such a low dielectric loss could be considered as a figure of merit for chemical purity and the small amount of mobile charged defects in the sample. For example, a low concentration of  $Ti^{+3}$ , which, if present would contribute to a hopping conductivity. Moreover, the lower loss in h-BTO is related to the absence of ferroelectric domain walls at room temperatures. By increasing the temperature the dielectric loss starts to increase for both material due to the increase of conductivity at elevated temperatures. It is important for the later discussion to notice much lower permittivity in h-BTO compared to that in p-BTO.

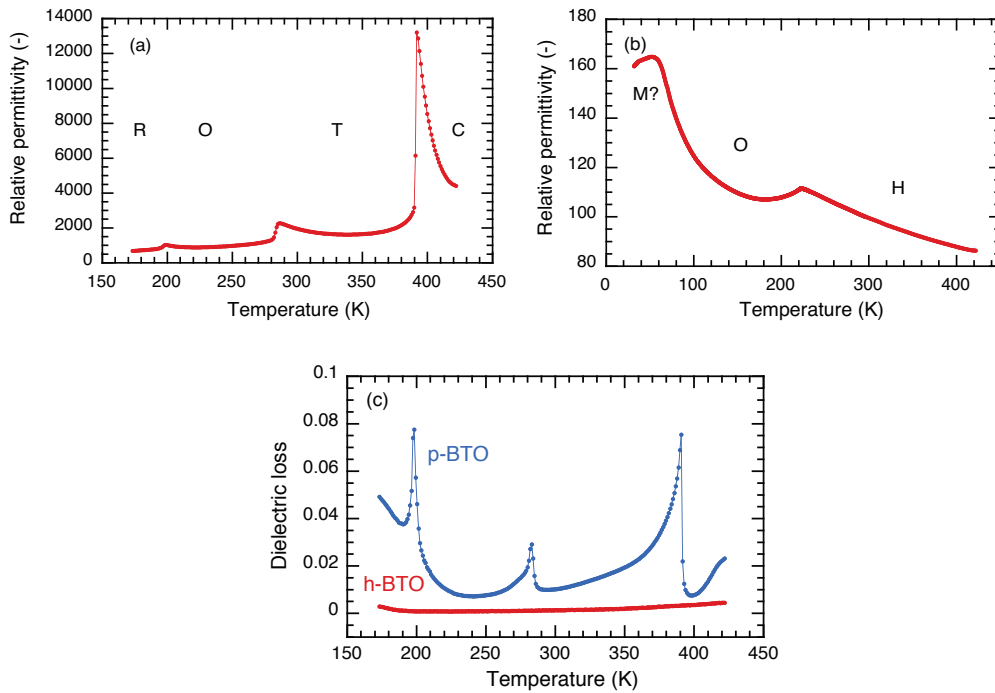


Figure 4.12 Temperature dependence of the relative permittivity of a) p-BTO and b) h-BTO. Letters R, O, T, C, M and H stand, respectively, for phases with rhombohedral, orthorhombic, tetragonal, cubic, monoclinic and hexagonal symmetries. c) Dielectric loss for p-BTO and h-BTO as a function of temperature at 1 kHz.

### 4.5 Elastic properties of p- and h-BTO as a function of temperature

In incipient ferroelectric-ferroelastic materials, such as  $\text{Pb}(\text{Mg}_{1/3}\text{Nb}_{2/3})\text{O}_3$  [24], polar regions are both electrically and elastically active possessing both polarization and strain with respect to the matrix of the nonpolar parent phase [25]. Aktas et al. [26] have investigated the elastic properties of p-BTO for evidences of polar precursors within its paraelectric cubic phase by resonance piezoelectric spectroscopy. Observation of resonances above the Curie temperature is associated with the presence and piezoelectric nature of dynamic polar regions. This fingerprint of polar regions was detected up to elevated temperatures, as high as 613 K. Figure 4.13 represents the elastic modulus and loss for p-BTO measured in this work by the DMA technique. All three phase transitions are indicated by anomalies in elastic modulus and loss due to the appearance or change in the configuration of ferroelastic domains and changes of the unit cell dimension through each phase transition. The frequency dispersion below the Curie temperature is related to the dynamics of ferroelectric-ferroelastic domain walls under applied elastic field. In addition, as reported in [26] frequency dispersion above  $T_C$  could be due to the dynamics of polar regions.

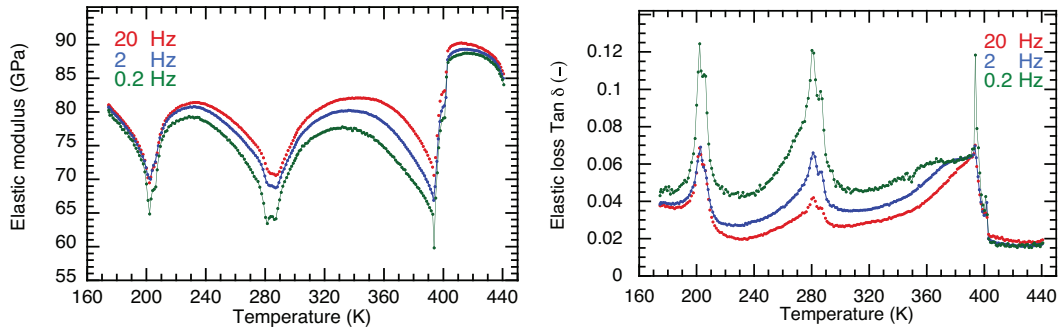


Figure 4.13 Temperature dependence of a) elastic modulus and b) elastic loss of p-BTO at three different frequencies.

In analogy to the presence of polar precursors of a ferroelectric phase above  $T_C$  in the case of p-BTO, one may therefore expect to see non-polar precursors of the ferroelastic phase in h-BTO above  $\approx 220$  K [27]. Figure 4.14 shows elastic modulus and associated  $\tan \delta$  as a function of temperature for h-BTO samples. Transition from the hexagonal paraelectric-paraelastic phase into orthorhombic paraelectric-ferroelastic phase is clearly visible around 220 K. The large softening of the material is due to the formation of ferroelastic domains below the phase transition temperature [28]. More significant and important is the frequency dispersion of the elastic modulus and frequency dependent peak of mechanical  $\tan \delta$  above the phase transition temperature. Both are most likely a consequence of the presence of elastic-dipolar regions. This situation is similar to the effect of electric and elastic dipolar regions on the permittivity and elastic modulus in relaxor ferroelectrics [25].

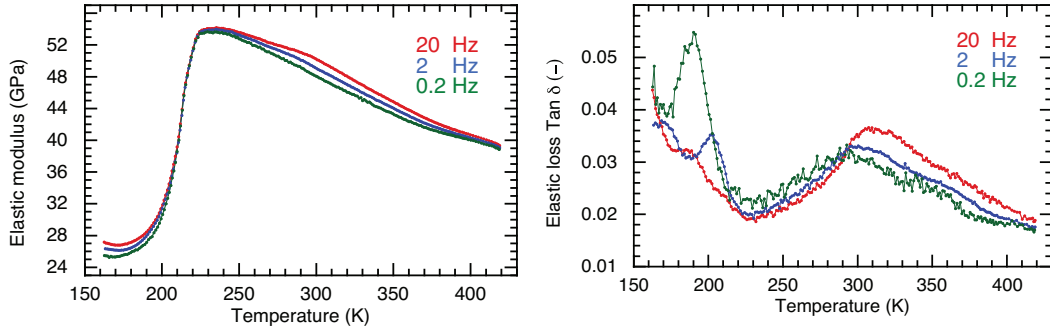


Figure 4.14 Temperature dependence of a) elastic modulus and b) elastic loss of h-BTO at three different frequencies.

The elastic data, therefore, suggest formation of nonpolar precursors of ferroelastic phase in h-BTO above  $\approx 220$  K and polar precursors of ferroelectric phase in p-BTO above its Curie temperature. It is important to recall that the ferroelastic phase of h-BTO is noncentrosymmetric i.e. piezoelectric. This means that local nonpolar precursors of the ferroelastic phase may exhibit piezoelectricity and could thus have an effect on the permittivity. However, those possibly piezoelectric elastic dipoles do not exhibit polarization and the pyroelectric effect. Consequences of this are discussed in more detail in the next sections.

#### 4.6 Dielectric Nonlinearity measurement

It is known that polar nano regions in relaxor ferroelectric materials contribute to the dielectric nonlinearity and it is believed that they show dynamics similar to that observed by domain walls in ferroelectrics [29-32]. Presence of polar regions in the paraelectric phase of a ferroelectric could be examined indirectly by examining the dielectric nonlinearity. Garten and Trolier-McKinstry [33, 34] studied (Ba,Sr)TiO<sub>3</sub> ceramics and thin films and proposed that the dependence of dielectric permittivity on electric field above  $T_C$  is due to the motion of polar regions and this motion can account for the apparently large flexoelectric effect reported for this material. Nonlinearity of polar regions will be discussed in more details in chapter 6.

It is interesting to investigate whether paraelectric phases of p-BTO and h-BTO exhibit dielectric nonlinearity; the result could be used to infer the presence or absence of polar precursors. If the dynamics of polar regions is responsible for the dielectric nonlinearity, one would not expect to observe it in h-BTO but could be apparent in p-BTO. However, this is not a trivial point because polar regions in chemically simpler compounds, such as BaTiO<sub>3</sub>, could manifest themselves in a less obvious way due to their different properties compared to polar regions in more complex perovskites with mixed cations, such as (Ba, Sr)TiO<sub>3</sub> and Pb(Mg<sub>1/3</sub>Nb<sub>2/3</sub>)O<sub>3</sub>.

Normalized dielectric permittivity for both p-BTO and h-BTO is plotted in Figure 4.15 for two temperatures above  $T_C$  (for h-BTO 203 K is just below the temperature of the phase transition into the ferroelastic orthorhombic phase). The observed nonlinearity for p-BTO in Figure 4.15 (a) is very small but that is expected at relatively weak fields used in the experiment. In fact, the nonlinearity measured in p-BTO is similar to the values reported in (Ba,Sr)TiO<sub>3</sub> for similar field

## 4.7 Pyroelectric measurement

range [33]. More pronounced nonlinearity in p-BTO at 413 K (closer to  $T_C$ ) than at 443 K is consistent with the assumption that the polar regions are larger and more numerous closer to the Curie temperature. For the origin of the nonmonotonous field dependence of the permittivity for p-BTO see chapter 6.

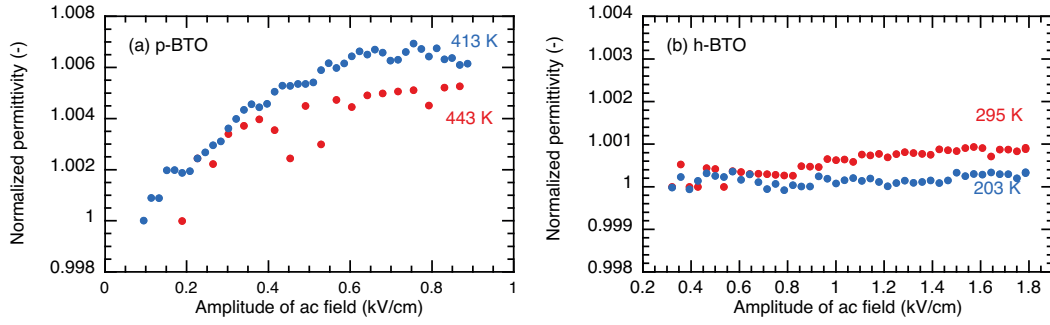


Figure 4.15 The dependence of dielectric permittivity on amplitude of the electric field for a) p-BTO and b) h-BTO. The values of permittivity are normalized with respect to the permittivity measured at approximately 0.1 kV/cm.

An even smaller, but measurable nonlinearity has also been observed in h-BTO, Figure 4.15 (b). Small dielectric nonlinearity for this material at room temperature could be associated with non-polar but piezoelectric precursors of ferroelastic state, which contribute to the apparent permittivity through electro-mechanical coupling. However, data obtained at 200 K does not support this conjecture: the nonlinearity should have been stronger at 200 K, just below the phase transition temperature into ferroelastic orthorhombic phase, than at room temperature if the piezoelectricity of ferroelastic domains and precursors contributed to the dielectric nonlinearity, while the opposite is observed. It is possible that at 200 K ferroelastic domain walls may be partially frozen and are not able to move much under weak fields used in the study. Other origins of the weak dielectric nonlinearity in h-BTO are discussed at the end of this chapter.

## 4.7 Pyroelectric measurement

Presence of ferroelectric state precursors within the cubic phase of p-BTO and non-polar precursors of the ferroelastic state within hexagonal phase of h-BTO is indicated before by optical [1] and elastic [13, 26] measurements. Precursors of low-temperature ferroic phases are responsible for the local symmetry breaking of each parent phase.

We now examine whether the precursors of ferroic states break *macroscopic* symmetry of cubic p-BTO and hexagonal h-BTO. Two statements can be made *a priori*: in case of p-BTO, if polar regions are preferentially oriented throughout the sample above  $T_C$ , the summation of ordered polar regions could result in nonzero macroscopic polarization, although very small. Therefore, the nominally cubic symmetry of p-BTO is broken. Pyroelectric measurement would enable us to detect this polarization in a nondestructive manner (see section 3.4). On the other hand, hexagonal barium titanate samples are not expected to exhibit pyroelectric response and consequently macroscopic polarization. Ferroelastic precursors in h-BTO are piezoelectric but not

polar at room temperature. Hence, one should not observe any macroscopic pyroelectric response even if ferroelastic nano regions are preferentially reoriented. We assume here that the tertiary pyroelectric effect due to piezoelectric effect and temperature gradient is too small [35].

Figure 4.16 shows the pyroelectric response of unpoled p-BTO ceramic at room temperature in its ferroelectric state. The sample shows polar behavior by inverting the response current when sample is flipped, suggesting that ferroelectric domains are not perfectly averaged to give a zero net polarization. Surfaces of the samples were marked with respect to their position in the furnace in which samples were sintered. This measurement was also used to verify the set-up.

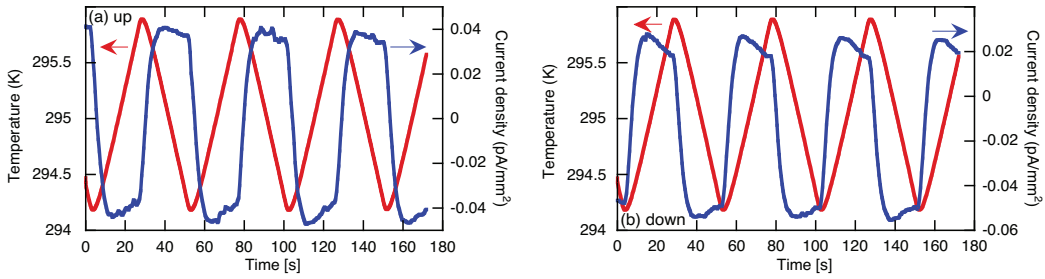


Figure 4.16 The pyroelectric current and the triangular temperature waveform for both sides of p-BTO sample at room temperature in the ferroelectric state.

The pyroelectric response of cubic p-BTO measured at  $\approx 413$  K, about 20 K above the Curie temperature, is shown in Figure 4.17. Minor drift of the pyroelectric current with time and noise in the current are due to fluctuations in the background current and instability of the background temperature. Presences of pyroelectric current and also its inversion reveal macroscopic symmetry breaking for p-BTO above  $T_C$ . Note that the same result was observed in single crystal BaTiO<sub>3</sub>, as shown in [36].

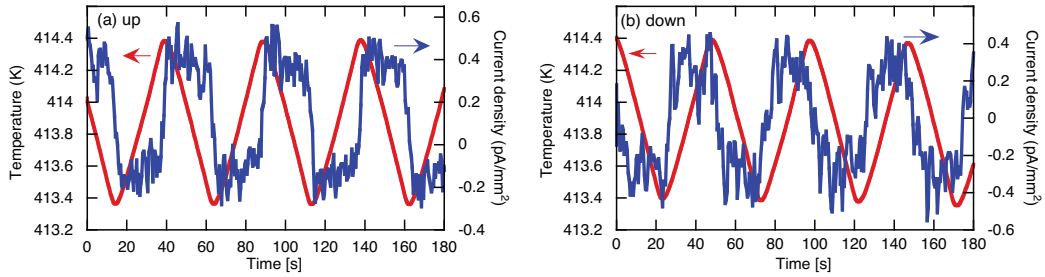


Figure 4.17 The pyroelectric current and the triangular temperature waveform for both sides of p-BTO sample at 413 K about 20 K above its Curie temperature.

The same experiment is shown for h-BTO at  $\approx 294$  K in Figure 4.18. h-BTO sample does not exhibit a pyroelectric current, even if the temperature amplitude is two times higher than used for p-BTO, only background current is observed.

#### 4.8 Macroscopic symmetry breaking revealed by Thermally Stimulated Currents

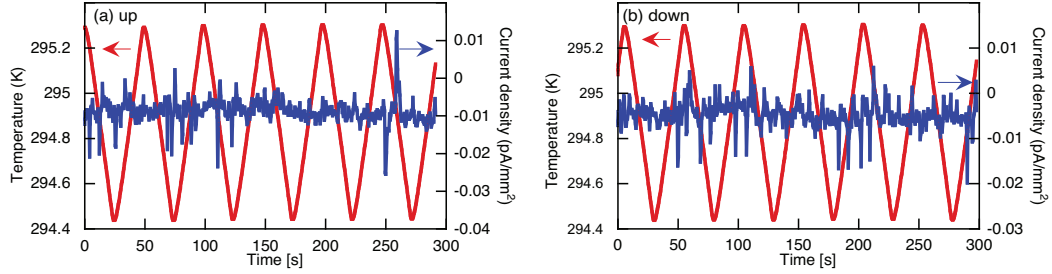


Figure 4.18 The pyroelectric current and the triangular temperature waveform for both sides of h-BTO sample at room temperature, 230 K above its Curie temperature.

These experimental results are thus consistent with the picture of ordered polar precursor being present in the cubic phase of p-BTO and absent in the hexagonal phase of h-BTO.

There are other reports in the literature in agreement with our results, demonstrating various forbidden effects in the nominal cubic symmetry in p-BTO that indicate global symmetry breaking [2, 26]. However, in Ref. [3], the measurements were made under electric field, which by itself could induce macroscopic polarization by reoriented polar nano-regions. h-BTO is a more complex case and there are several tentative arguments to explain absence of the pyroelectric response in this material in addition to the absence of polar regions. These issues will be addressed in the next sections.

#### 4.8 Macroscopic symmetry breaking revealed by Thermally Stimulated Currents

The appearance of the pyroelectric response in the paraelectric cubic phase of p-BTO could be considered as a possible evidence of macroscopic ordering of local polar precursors in this material, suggesting breaking of the centric symmetry both in local and global scale. On the other hand, the expected absence of pyroelectric current in hexagonal phase of h-BTO is consistent with the absence of a polar precursor. Although pyroelectric data suggest that h-BTO is not macroscopically pyroelectric, they do not give enough information whether macroscopic centric symmetry is broken. Thermally stimulated current was measured to seek for signs of macroscopic breaking of centric symmetry that does not manifest itself in the pyroelectric effect.

Samples were cut into halves and their surfaces were marked with respect to their position in the furnace, same as what was done in pyroelectric measurements. During TSC measurements for each sample, the “up” side of one half and the “down” side of the other half was in contact with the top electrode. The electric current was measured in the samples during heating and cooling. Both p-BTO and h-BTO showed thermally stimulated currents during heating and cooling, as plotted in Figure 4.19 and Figure 4.20 respectively.

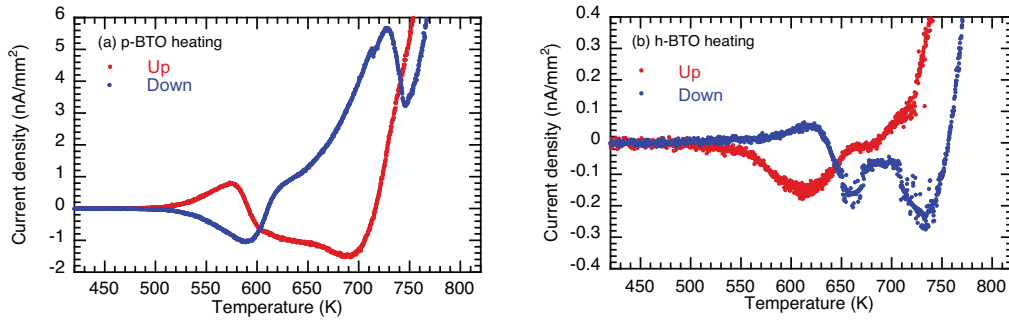


Figure 4.19 Thermally stimulated current for a) p-BTO and b) h-BTO during heating. Different signs of the current peaks between 550-650 K show that direction of the current depends on the orientation of the sample with respect to electrodes.

Possible origins of the thermally stimulated current were discussed in section 3.5. However, in our measurements since no electric field was applied on the samples and they were not polarized by an electric field to form an electret, the question can be posed about origins of the currents. Biancoli [36] has investigated the effective correlation between the TSC peak and the direction of polarization in the poled ferroelectric ceramics of  $0.5(\text{Ba}_{0.7}\text{Ca}_{0.3})\text{TiO}_3$ - $0.5\text{Ba}(\text{Zr}_{0.2}\text{Ti}_{0.8})\text{O}_3$  known as BCZT50 with two structural phase transition between 300 K and 373 K. His results indicated that sign of TSC peaks originating from polarization and phase transitions depends on the orientation of the sample in the setup. In analogy to TSC measurement for poled BCZT50 ceramics, the clear sign inversion of current peaks in p-BTO and h-BTO between 500 K and 750 K during heating (Figure 4.19 and Figure 4.20) should be sensitive to the sample orientation if there is a built-in polarization. In addition, if the current were originated from other sources like small voltage burden on the picoammeter [37] ( $300 \mu\text{V}$  in case of device used in our experiments) or temperature gradient across the sample (Seebeck effect) [38], it should not be sensitive to sample orientation (see section 3.5). Thermopolarization effect [39] could be another possible origin of TSC current, it may appear in materials with inversion center like both p- and h-BTO, however thermopolarization current needs a large time-dependent temperature gradient which is not the case here. Above 750 K a large increase in the current was observed during heating and cooling, whose sign is independent from sample orientation. This increase could be related to thermo-electric currents [38], low resistance of the sample and burden voltage across the picoammeter [37].

#### 4.8 Macroscopic symmetry breaking revealed by Thermally Stimulated Currents

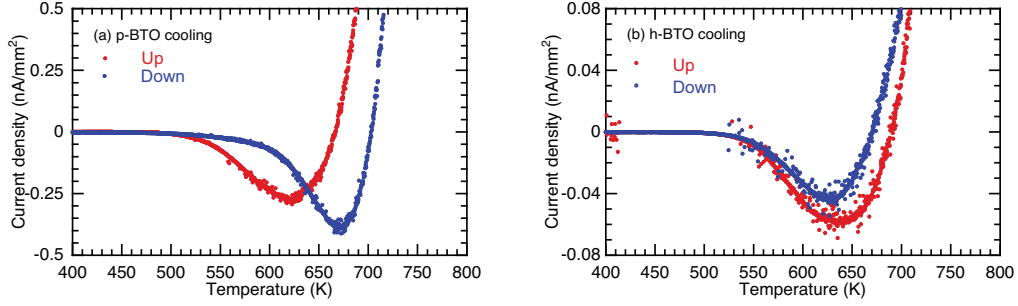


Figure 4.20 Thermally stimulated current for a) p-BTO and b) h-BTO during cooling.

No anomalies were observed during cooling for p- and h-BTO and also peaks have the same sign for both sides of samples. If the peaks were originated from a permanent built-in polarization due to the symmetry breaking, they would be seen on cooling as well, with opposite signs for the two sides of the sample. As shown in Figure 4.21 the p-BTO sample is still pyroelectric after cooling to room temperature from 830 K. This implies that the observed current peaks during heating is not associated with the disappearance of built in polarization itself but with the detrapping of trapped space charges. These charges may reinforce built-in polarization but are not its origin. It is important to mention that current sign originating from trapped charges is determined by the direction of the built-in polarization. After heating the sample, the space charges are released and what is observed during cooling is a background current that does not depend on the sample orientation.

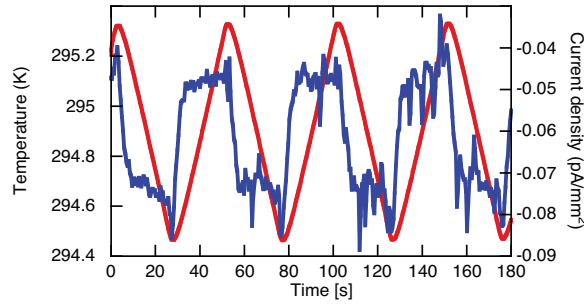


Figure 4.21 The pyroelectric current and the triangular temperature waveform measured immediately after TSC for down side of p-BTO.

Considering the mentioned reasons and after eliminating obvious possibilities such as surface effects and asymmetrical electrodes [40], this experiment proves that the samples cannot possess macroscopic centric symmetry. Breaking of symmetry in TSC may be expected for p-BTO because it exhibits macroscopic pyroelectricity and is therefore asymmetric; the sensitivity of TSC on orientation of h-BTO samples is surprising. These experiments show indisputably that the macroscopic inversion symmetry is also broken in h-BTO samples.



## 4.9 Discussion and conclusion

In this chapter our objective was to separate polar regions as the main mechanism for the symmetry breaking of p-BTO at paraelectric phase from other mechanisms, such as built-in flexoelectric polarization and inhomogeneous distribution of defects (e.g. ionic charges).

Considering the combination of our dielectric, elastic, pyroelectric and thermally stimulated measurements data with crystal symmetry of p-BTO and h-BTO and previous studies on polar regions in p-BTO, it is possible to indicate that: i) cubic phase of p-BTO shows microscopic and macroscopic breaking of nominal centrosymmetry and possess local and global polarization. These polarizations are likely associated with precursors of the ferroelectric phase known as polar regions. Global polarization of p-BTO could be related to macroscopic ordering of polar regions in this material; ii) the hexagonal phase of h-BTO probably exhibits precursors of the nonpolar paraelectric-ferroelastic phase and as a result does not possess microscopic and macroscopic polarization, although TSC measurements has shown that its macroscopic centric symmetry is broken; iii) ferroelastic regions ("elastic dipoles") are elastically active in paraelastic phase of hexagonal h-BTO, while polar regions are electrically and elastically mobile in the paraelectric phase of p-BTO.

Similar to what was reported for (Ba,Sr)TiO<sub>3</sub> solid solution [40], the mechanism governing the alignment of polar regions in p-BTO could be strain gradient. Strain gradient also exists in h-BTO because both h-BTO and p-BTO are prepared from the same starting powder under similar conditions. However, due to the non-polar nature of paraelectric-ferroelastic precursors in hexagonal phase, their ordering does not result in macroscopic polarization. Strain gradient might be needed in qualitative model of both materials because it explains directly the symmetry breaking in h-BTO revealed by TSC.

One can further consider that the precursors of paraelectric-ferroelastic phase could carry polarization related to the low-temperature ferroelectric phase of h-BTO below  $T_C \approx 50 - 70$  K [5, 7, 17]. However, since room temperature is so far away from the Curie temperature and the density of polar regions should scale with distance from  $T_C$  this polarization may not be easy to observe. However, although polarization is weak in the ferroelectric phase of h-BTO and strain is the order parameter [41] (rather than polarization), it is unlikely that h-BTO shows a polarization in ferroelastic regions that is smaller than our setup resolution. As an indication of the detection limit of pyroelectric current originated from ordered polar regions, as presented in Figure 4.22 we have observed rather strong pyroelectric current at room temperature in (Ba<sub>0.1</sub>Sr<sub>0.9</sub>)TiO<sub>3</sub> with  $T_C \approx 65$  K, near to the Curie temperature of h-BTO.

#### 4.9 Discussion and conclusion

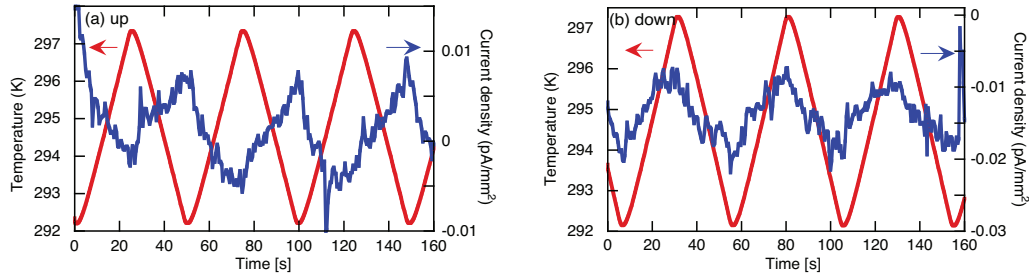


Figure 4.22 The pyroelectric current of  $(\text{Ba}_{0.1}\text{Sr}_{0.9})\text{TiO}_3$  measured at room temperature.

In this part we look at alternative mechanisms for symmetry breaking of investigated materials. We mentioned the strain gradient as the parameter, which might be responsible for aligning polar regions, which leads to macroscopic asymmetry. However, it should be noted that a strain gradient itself breaks the centrosymmetry of material even in absence of polar regions with flexoelectricity as the possible origin of pyroelectric current (flexoelectric coefficient relates strain gradient and polarization). Same mechanism were suggested for thin film due to either strain or chemical gradient [42]. In this case, nonappearance of pyroelectric current in h-BTO may imply that it is too small to be measured. Because flexoelectric polarization is proportional to permittivity [43] and h-BTO has small permittivity (around 100 at room temperature), the flexoelectric polarization may be small. We argue that if this was the case, it should have been valid for  $(\text{Ba}_{0.1}\text{Sr}_{0.9})\text{TiO}_3$  as well, because its permittivity value is in the same range of h-BTO. However, we have measured rather large pyroelectric response for this material as shown in Figure 4.22.

Therefore, we probably could have measured pyroelectric current in h-BTO if its origin was built-in flexoelectricity. Thus absence of pyroelectric current in h-BTO suggests another mechanism for symmetry breaking rather than insufficient resolution of our measurement. Remarkably, some flexoelectric experiments eliminated the presence of built-in polarization in single crystals of  $\text{BaTiO}_3$  [44]. Macroscopic polarization could have also been due to the separation or inhomogeneous distribution of charged defects instead of polar regions alignment. Strain gradient could be responsible for defects separation through chemical expansivity [40, 45, 46]. On the other hand the strain gradients could assist creation of ionic vacancies [46]. Although p- and h-BTO were prepared from the same powder and in similar sintering conditions, our data propose that h-BTO has lower concentration of mobile charges compared to p-BTO (TSC peaks and dielectric loss are one order of magnitude smaller in h-BTO than in p-BTO). This is fairly surprising considering the fact that h-BTO is unstable at room temperature and is usually stabilized with doping and/or under reducing sintering conditions which result in higher concentration of oxygen vacancies and reduced titanium [19, 22].

Moreover, TSC peaks from releasing the trapped charges appear at higher temperatures for h-BTO than p-BTO implying its higher activation energy of trapped charges [47]. This could be associated with different connections of oxygen octahedral in these two polymorphs. All this, combined with low permittivity of h-BTO, may make related polarization too small and too rigid to show pyroelectric current in response to small temperature variation at room temperature. If so, it's possible to explain different behavior of p- and h-BTO by excluding polar precursors as a

possible origin for symmetry breaking. However, we consider that relation between low permittivity and the charge model needs more investigation and it appears that low permittivity alone is not able to explain the absence of pyroelectricity in h-BTO. For example, a clear and strong pyroelectric response is observed by Wruck et al. [48] in doped nonpolar ferroelastic Pb<sub>3</sub>(PO<sub>4</sub>)<sub>2</sub> with even smaller permittivity than h-BTO.

From TSC experiment and absence of pyroelectric current in h-BTO it's possible to conclude that peaks in the current are not related to polar regions of p-BTO and ferroelastic precursors of h-BTO. In relaxor ferroelectrics, thermally activated acoustic emission measurements have shown peaks at one or more characteristics temperatures below Burns temperature, which have been related with processes within polar nano regions [49, 50]. One could conclude that the TSC peaks observed here are also related to those acoustic emission peaks because they would be generated from both polar regions and precursors of ferroelastic phase. The required electric charge for the current peaks in h-BTO could be originated from the piezoelectricity of ferroelastic phase. However, acoustic emission peaks in relaxor ferroelectrics were observed during cooling [49] while there was no peak present in TSC on cooling. As a result the two phenomena (peaks in TSC and acoustic emission) do not seem to be linked together.

Finally, it's possible that the pseudo Jahn-Teller effect (PJTE) [51] is responsible for polarization in nominally centrosymmetric BTO, where local dipolar distortions interact with the strain gradient. Since we do not see polarization in h-BTO, that could indicate differences in the PJTE in hexagonal h-BTO and cubic p-BTO. Therefore, our experimental results could be used for verification of theoretical models of PJTE in hexagonal BTO and for clarification of a possible role of PJTE in enhancing properties of ferroelectric-based materials as suggested in [52].

To conclude, we propose that all presented experimental results can be consistently explained by the strain gradient and its interaction with microscopic precursors of the ferroic states of the two materials.

## Bibliography

- [1] A. Pugachev, V. Kovalevskii, N. Surovtsev, S. Kojima, S. Prosandeev, I. Raevski, *et al.*, "Broken local symmetry in paraelectric BaTiO<sub>3</sub> proved by second harmonic generation," *Physical review letters*, vol. 108, p. 247601, 2012.
- [2] K. Wieczorek, A. Ziebiniska, Z. Ujma, K. Szot, M. Górny, I. Franke, *et al.*, "Electrostrictive and piezoelectric effect in BaTiO<sub>3</sub> and PbZrO<sub>3</sub>," *Ferroelectrics*, vol. 336, pp. 61-67, 2006.
- [3] H. Beige and G. Schmidt, "Electromechanical resonances for investigating linear and nonlinear properties of dielectrics," *Ferroelectrics*, vol. 41, pp. 39-49, 1982.
- [4] A. K. Tagantsev, L. E. Cross, and J. Fousek, *Domains in ferroic crystals and thin films*: Springer, 2010.
- [5] K. Deguchi, H. Kobayashi, E. Nakamura, H. Yamaguchi, H. Uwe, and T. Sakudo, "Dielectric dispersion and twin structure in hexagonal barium titanate," *Journal of the Physical Society of Japan*, vol. 57, pp. 4011-4020, 1988.
- [6] E. Sawaguchi, Y. Akishige, and M. Kobayashi, "Structural phase transition in hexagonal barium titanate," *J. Phys. Soc. Japan*, vol. 54, p. 480, 1985.
- [7] E. Sawaguchi, Y. Akishige, and M. Kobayashi, "Ferroelectric behavior in hexagonal type barium titanate," *Japanese Journal of Applied Physics*, vol. 24, p. 252, 1985.
- [8] E. Buixaderas, S. Kamba, J. Petzelt, M. Wada, K. Yamanaka, and K. Inoue, "Study of Phase Transitions in Hexagonal BaTiO<sub>3</sub> by means of Far-infrared Spectroscopy," *Journal of the Korean Physical Society*, vol. 32, p. S578, 1998.
- [9] M. Yamaguchi, M. Watanabe, Y. Akishige, K. Inoue, and T. Yagi, "Successive phase transitions of hexagonal barium titanate: soft acoustic mode and coupled acoustic-soft optic mode," *Physica B*, p. 647, 1996.
- [10] Y. Akishige, G. Oomi, T. Yamamoto, and E. Sawaguchi, "Dielectric properties of ferroelectric hexagonal BaTiO<sub>3</sub>," *J. Phys. Soc. Japan*, vol. 58, p. 930, 1989.
- [11] E. Sawaguchi, Y. Akishige, and T. Yamamoto, "Ferroelectric phase transition in hexagonal type BaTiO<sub>3</sub>," *Ferroelectrics*, vol. 106, p. 63, 1990.
- [12] T. Yamamoto, Y. Akishige, and E. Sawaguchi, "Twins in the intermediate phase of hexagonal BaTiO<sub>3</sub>," *Ferroelectrics*, vol. 97, p. 189, 1989.
- [13] S. Hashemizadeh, A. Biancoli, and D. Damjanovic, "Symmetry breaking in hexagonal and cubic polymorphs of BaTiO<sub>3</sub>," *Journal of Applied Physics*, vol. 119, p. 094105, 2016.
- [14] C. N. R. Rao and J. Gopalakrishnan, *NEW DIRECTIONS IN SOLID STATE CHEMISTRY. Edition en anglais*: Cambridge University Press, 1997.
- [15] R. Burbank and H. T. Evans, "The crystal structure of hexagonal barium titanate," *Acta Crystallographica*, vol. 1, pp. 330-336, 1948.
- [16] H. T. Evans Jr and R. D. Burbank, "The crystal structure of hexagonal barium titanate," *The Journal of Chemical Physics*, vol. 16, pp. 634-634, 1948.
- [17] E. Sawaguchi, Y. Akishige, and M. Kobayashi, "Structural phase transition in hexagonal barium titanate," *Journal of the Physical Society of Japan*, vol. 54, pp. 480-482, 1985.

- [18] J. Akimoto, Y. Gotoh, and Y. Oosawa, "Refinement of hexagonal BaTiO<sub>3</sub>," *Acta Crystallographica Section C: Crystal Structure Communications*, vol. 50, pp. 160-161, 1994.
- [19] R. Glaister and H. Kay, "An investigation of the cubic-hexagonal transition in barium titanate," *Proceedings of the Physical Society*, vol. 76, p. 763, 1960.
- [20] D. Sinclair, J. S. Skakle, F. Morrison, R. Smith, and T. Beales, "Structure and electrical properties of oxygen-deficient hexagonal BaTiO<sub>3</sub>," *Journal of Materials Chemistry*, vol. 9, pp. 1327-1331, 1999.
- [21] M. Wakamatsu, "INFLUENCE OF FIRING ATMOSPHERE ON THE CUBIC-HEXAGONAL TRANSITION AND THE CHEMICAL STATE OF TITANIUM IN BaTiO<sub>3</sub>," *J. CERAM. SOC. JAP. J. Ceram. Soc. Jap.*, vol. 95, p. 1181, 1987.
- [22] A. Rečnik, J. Bruley, W. Mader, D. Kolar, and M. Rühle, "Structural and spectroscopic investigation of (111) twins in barium titanate," *Philosophical Magazine B*, vol. 70, pp. 1021-1034, 1994.
- [23] Y. Akishige, G. Oomi, T. Yamaoto, and E. Sawaguchi, "Dielectric Properties of Ferroelectric Hexagonal BaTiO<sub>3</sub>," *Journal of the Physical Society of Japan*, vol. 58, pp. 930-939, 1989.
- [24] R. Blinc, V. Laguta, and B. Zalar, "Field Cooled and Zero Field Cooled P b 207 NMR and the Local Structure of Relaxor P b M g 1/3 N b 2/3 O 3," *Physical review letters*, vol. 91, p. 247601, 2003.
- [25] H. Uršič and D. Damjanovic, "Anelastic relaxor behavior of Pb (Mg<sub>1/3</sub>Nb<sub>2/3</sub>) O<sub>3</sub>," *Applied Physics Letters*, vol. 103, p. 072904, 2013.
- [26] O. Aktas, M. A. Carpenter, and E. K. Salje, "Polar precursor ordering in BaTiO<sub>3</sub> detected by resonant piezoelectric spectroscopy," *Applied Physics Letters*, vol. 103, p. 142902, 2013.
- [27] E. K. Salje and W. Schranz, "Low amplitude, low frequency elastic measurements using dynamic mechanical analyzer (DMA) spectroscopy," *Zeitschrift für Kristallographie Crystalline Materials*, vol. 226, pp. 1-17, 2011.
- [28] W. Schranz, H. Kabelka, A. Sarras, and M. Burock, "Giant domain wall response of highly twinned ferroelastic materials," *Applied Physics Letters*, vol. 101, p. 141913, 2012.
- [29] A. Bokov and Z.-G. Ye, "Recent progress in relaxor ferroelectrics with perovskite structure," in *Frontiers of Ferroelectricity*, ed: Springer, 2006, pp. 31-52.
- [30] A. Glazounov, A. Tagantsev, and A. Bell, "Evidence for domain-type dynamics in the ergodic phase of the PbMg<sub>1/3</sub>Nb<sub>2/3</sub>O<sub>3</sub> relaxor ferroelectric," *Physical Review B*, vol. 53, p. 11281, 1996.
- [31] A. a. Glazounov and A. Tagantsev, "Phenomenological model of dynamic nonlinear response of relaxor ferroelectrics," *Physical review letters*, vol. 85, p. 2192, 2000.
- [32] V. Westphal, W. Kleemann, and M. Glinchuk, "Diffuse phase transitions and random-field-induced domain states of the "relaxor" ferroelectric PbMg<sub>1/3</sub>Nb<sub>2/3</sub>O<sub>3</sub>," *Physical review letters*, vol. 68, p. 847, 1992.
- [33] L. Garten, P. Lam, D. Harris, J.-P. Maria, and S. Trolier-McKinstry, "Residual ferroelectricity in barium strontium titanate thin film tunable dielectrics," *Journal of applied physics*, vol. 116, p. 044104, 2014.

- [34] L. M. Gerten and S. Trolor-McKinstry, "Enhanced flexoelectricity through residual ferroelectricity in barium strontium titanate," *Journal of Applied Physics*, vol. 117, p. 094102, 2015.
- [35] R. Whatmore, "Pyroelectric devices and materials," *Reports on progress in physics*, vol. 49, p. 1335, 1986.
- [36] A. Biancoli, "Breaking of the macroscopic centric symmetry in  $\text{Ba}_{1-x}\text{Sr}_x\text{TiO}_3$  ceramics and single crystals," 2014.
- [37] W. S. Lau, T. C. Chong, L. S. Tan, C. H. Goo, and K. S. Goh, "The characterization of traps in semi-insulating gallium arsenide buffer layers grown at low temperature by molecular beam epitaxy with an improved zero-bias thermally stimulated current technique," *Japanese journal of applied physics*, vol. 30, p. L1843, 1991.
- [38] W. Lau, K. Wong, T. Han, and N. P. Sandler, "Application of zero-temperature-gradient zero-bias thermally stimulated current spectroscopy to ultrathin high-dielectric-constant insulator film characterization," *Applied physics letters*, vol. 88, p. 172906, 2006.
- [39] V. Gurevich and A. Tagantsev, "Theory for the thermopolarization effect in dielectrics having a center of inversion," *Pis'ma ZhETF*, vol. 35, pp. 106-108, 1982.
- [40] A. Biancoli, C. M. Fancher, J. L. Jones, and D. Damjanovic, "Breaking of macroscopic centric symmetry in paraelectric phases of ferroelectric materials and implications for flexoelectricity," *Nature materials*, vol. 14, pp. 224-229, 2015.
- [41] M. Yamaguchi, M. Watanabe, Y. Akishige, K. Inoue, and T. Yagi, "Successive phase transitions of hexagonal barium titanate: soft acoustic mode and coupled acoustic-soft optic mode," *Physica B: Condensed Matter*, vol. 219, pp. 647-649, 1996.
- [42] J. C. Agar, A. R. Damodaran, G. A. Velarde, S. Pandya, R. Mangalam, and L. W. Martin, "Complex Evolution of Built-in Potential in Compositionally-Graded  $\text{PbZr}_{1-x}\text{Ti}_x\text{O}_3$  Thin Films," *ACS nano*, vol. 9, pp. 7332-7342, 2015.
- [43] A. Tagantsev, "Piezoelectricity and flexoelectricity in crystalline dielectrics," *Physical Review B*, vol. 34, p. 5883, 1986.
- [44] J. Narvaez, S. Saremi, J. Hong, M. Stengel, and G. Catalan, "Large flexoelectric anisotropy in paraelectric barium titanate," *Physical review letters*, vol. 115, p. 037601, 2015.
- [45] S. B. Adler, "Chemical expansivity of electrochemical ceramics," *Journal of the American Ceramic Society*, vol. 84, pp. 2117-2119, 2001.
- [46] U. Aschauer, R. Pfenninger, S. M. Selbach, T. Grande, and N. A. Spaldin, "Strain-controlled oxygen vacancy formation and ordering in  $\text{CaMnO}_3$ ," *Physical Review B*, vol. 88, p. 054111, 2013.
- [47] G. Sessler, "Physical principles of electrets," in *Electrets*, ed: Springer, 1980, pp. 13-80.
- [48] B. Wruck, U. Bismayer, and E. Salje, "Dielectric properties of  $\text{Pb}_3(\text{PO}_4)_2$   $\text{Pb}_3(\text{AsO}_4)_2$ ," *Materials Research Bulletin*, vol. 16, pp. 251-257, 1981.
- [49] M. Roth, E. Mojaev, E. Dul'kin, P. Gemeiner, and B. Dkhil, "Phase Transition at a Nanometer Scale Detected by Acoustic Emission within the Cubic Phase  $\text{Pb}(\text{Zn}^{1/3}\text{Nb}^{2/3})\text{O}_3$   $\text{PbTiO}_3$  Relaxor Ferroelectrics," *Physical review letters*, vol. 98, p. 265701, 2007.
- [50] P. Gehring, H. Hiraka, C. Stock, S.-H. Lee, W. Chen, Z.-G. Ye, *et al.*, "Reassessment of the Burns temperature and its relationship to the diffuse scattering, lattice dynamics, and

thermal expansion in relaxor  $\text{Pb}(\text{Mg}^{1/3}\text{Nb}^{2/3})\text{O}_3$ ," *Physical Review B*, vol. 79, p. 224109, 2009.

- [51] I. B. Bersuker, "Pseudo Jahn–Teller effect in the origin of enhanced flexoelectricity," *Applied Physics Letters*, vol. 106, p. 022903, 2015.
- [52] I. B. Bersuker, "Giant permittivity and electrostriction induced by dynamic Jahn-Teller and pseudo Jahn-Teller effects," *Applied Physics Letters*, vol. 107, p. 202904, 2015.





## **Chapter 5. Origins of symmetry breaking in (Ba,Sr)TiO<sub>3</sub> system: processing issues**

### **5.1 Introduction**

We start this chapter with a short review of main results obtained by Biancoli on the origins of the symmetry breaking in BST prior to this study. They are summarized as follows: 1) The symmetry breaking in the samples probably develops during the densification process in the sintering step where material transport is maximal [1]; 2) Williamson-Hall analysis of the X-ray diffraction (XRD) data showed presence of a non-uniform microstrain across the sample thickness, possibly developed by the small thermal gradient or even gravity during the sintering [2]. The presence of the microstrain in the sample, which implies variation of lattice parameters, may orient separated charge defects and/or polar entities, and results in the built-in polarization; 3) Orientation of the sample in the furnace during the sintering defines the direction of the built-in polarization. When the direction is set, it is stable and survives temperatures in excess of 1720 K; 4) Detection of the symmetry breaking in the paraelectric phase of single crystals in the (Ba,Sr)TiO<sub>3</sub> solid solution indicates that the mechanism is not related to the polycrystalline nature of the ceramics; 5) Comparison of results for as-sintered samples and samples polished by half of their thickness proves that the symmetry breaking is not caused by surface effects; 6) Polarization in (Ba,Sr)TiO<sub>3</sub> consists of two components: one is built in the samples during the densification, which is stable and possesses definite orientation, and the other one is volatile, unstable and most likely is related to free charges that are trapped around the built-in polarization. This volatile component of the polarization is responsible for the peaks in thermally stimulated currents and dispersion of the electro-mechanical properties at low frequencies [1]. Experiments performed by Biancoli did not allow identification of the exact nature of the entities responsible for the built-in polarization. Both charged ionic defects (such as oxygen vacancies) and polar regions are the candidates.

The aim of this chapter is to shed more light on the origins of symmetry breaking in (Ba,Sr)TiO<sub>3</sub> (BST) system by monitoring the evolution of the asymmetry within the samples as a function of preparation parameters. Also studying different samples from various sources processed with very different techniques would enable us to reinforce the claim that the symmetry breaking is a general phenomenon rather than being limited to specific processing conditions.

### **5.2 Effect of processing conditions on pyroelectric response of BST6040**

Sample processing is perhaps the most critical stage in this work because the breaking of the global centric symmetry takes place during the sintering step. However, it is not clear which type of asymmetry during the sintering is responsible for the symmetry breaking and whether such asymmetry can be avoided.

One possibility to minimize both thermal gradient and gravitation effects is to continuously rotate the sample during sintering. A homemade Pt rotating sample holder and a tube

## 5.2 Effect of processing conditions on pyroelectric response of BST6040

furnace were used for this purpose. Samples were covered by powders with the same composition inside the sample holder to minimize any probable substrate effect and uneven heat transfer. Figure 5.1 shows that BST6040 sample sintered with continues rotation still show polar behavior above  $T_C$ . This result can exclude simple case of gravity as a possible origin of symmetry breaking. However, complete cancellation of thermal gradient is more challenging. While a perfect spherical rotation of the sample holder could minimize effects of temperature gradient across the diameter of the tube, the rotation cannot eliminate the thermal gradient along the axis of tube due to the arrangement of heating elements inside the furnace. Therefore just based on this experiment it's not possible to entirely eliminate the effect of thermal gradient on the symmetry breaking.

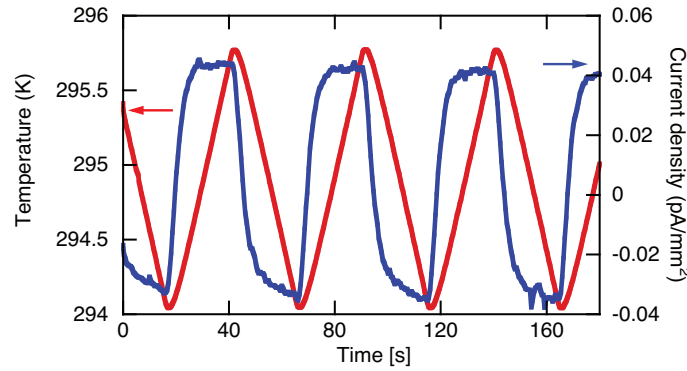


Figure 5.1 Pyroelectric response of BST6040 sintered with continues rotation.

BST is a very process-dependent material so it's possible to pose the question whether the observed symmetry breaking is limited to our processing conditions or not. To answer this question, we have studied BST samples processed with various precursors and very different techniques by different research groups (sol-gel and solid-state routes, spark plasma sintered and normal sintered samples, tape casted samples). Different samples are listed as follows: i) Spark Plasma Sintered (SPS) samples were provided by Prof. Catherine Elissalde from University of Bordeaux. Samples were pressed and sintered from carbonate precursors using a Dr. Sinter SPS-2080 apparatus (SPS Syntex Inc., Tokyo, Japan) with the pulse sequence of 12-2 (pulses-dead time or zero current). At start, the temperature was raised to 870 K in 3 minutes and then reached to 1670 K with heating rate of 100 K/min. Samples were sintered for 10 minutes under uniaxial pressure of 90 MPa. As-sintered samples were subjected to a post thermal treatment at 1070 K for 10 hours in air for reoxidization and removal of the surface carbon contamination [3, 4]. ii) Sol-gel samples; complete procedure for fabrication of sol-gel samples is discussed in chapter 2. iii) We also received both solid-state BST6040 powders and sintered samples from prof. Takuya Hoshina (Tokyo Institute of Technology). All of the mentioned samples prepared with different chemical routes and/or processing conditions were compared to samples processed by our convectional solid-state route.

As presented in Figure 5.2, forbidden pyroelectric current is present for all of the samples prepared from different methods. The composition of SPS sample was BST6535 with  $T_C$  of 293 K, the pyroelectric measurement was done at 313 K to ensure that sample is in its paraelectric phase

and also to keep the temperature distance of 20 K from  $T_C$  for both BST6040 and BST6535 samples. Studying the effect of sintering time was also possible by comparing results of SPS and normally sintered samples. SPS samples indeed showed one order of magnitude smaller pyroelectric current. However, interpretation of this result is not straightforward because SPS prepared samples exhibited suppressed dielectric permittivity and contained a large concentration of defects (grey color of those samples probably suggests presence of oxygen vacancies); those secondary effects must be taken into account when interpreting the results.

It's important to mention that the symmetry breaking was also observed in other compositions like  $\text{Pb}(\text{Mg}_{1/3}\text{Nb}_{2/3})\text{O}_3$  ceramics and single crystals of  $\text{K}(\text{Ta,Nb})\text{O}_3$  [5]. These results indicate that the symmetry breaking in the paraelectric phase of ferroelectrics is a general effect and it is not specific to one material or preparation procedure and is generally encountered in perovskite materials and broader.

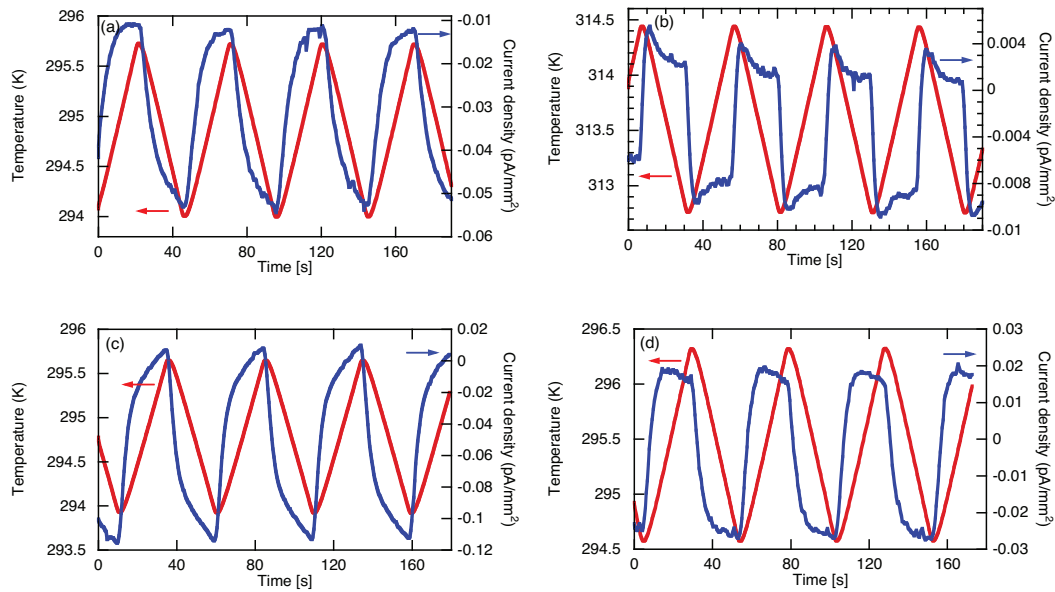


Figure 5.2 Pyroelectric response for samples prepared from different starting powders and processing conditions. (a) sol-gel sample (b) spark plasma sintered sample (c) sample processed with powder provided from Japan in our laboratory and (d) sample sintered in Japan.

### 5.3 Effect of grain size on pyroelectric response of BST6040

To study the effect of grain size on the symmetry breaking and the pyroelectric response of BST6040 ceramics in their paraelectric phase, samples with different grain size were provided by prof. Takuya Hoshina from Tokyo Institute of Technology.

Two-step sintering technique was used for obtaining high-density ceramics without significant grain growth. In the first step the goal is to obtain an intermediate density and produce a uniform pore structure by the grains rearrangements. Full densification happens in the second step. The sintering conditions for BST6040 were determined from the analysis of shrinkage curves to obtain the full densification. In the first stage, BST6040 ceramics were heated up to 1643 K

### 5.3 Effect of grain size on pyroelectric response of BST6040

with heating rate of 23 K/min then they have rapidly cooled with rate of 100 K/min down to different  $T_2$  temperatures (1490,1450,1400 K) with the dwell time of 15 hours [6]. Figure 5.3 presents schematics of the two-step sintering process.

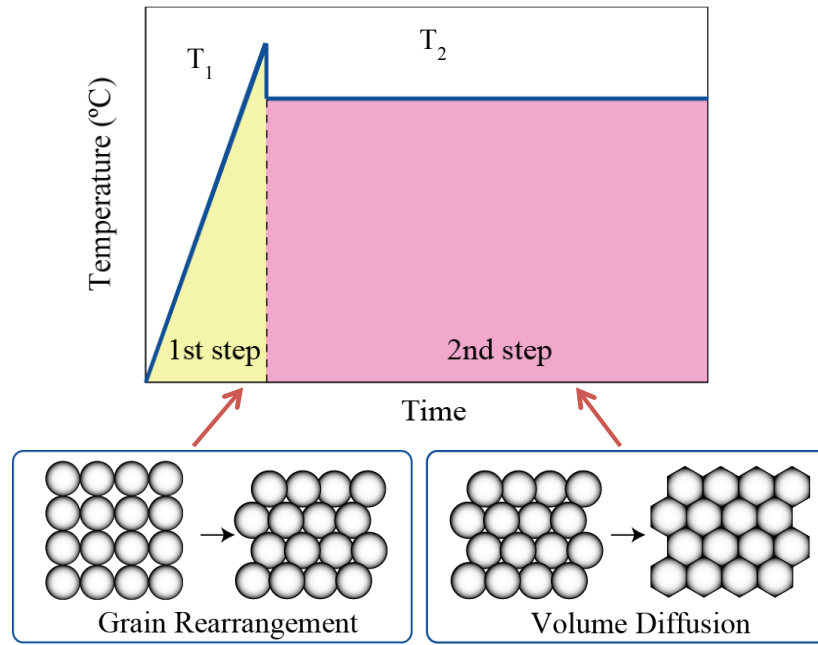


Figure 5.3 Schematic of two-step sintering process for BST6040.

By changing  $T_2$  from 1400 to 1490 K the grain size varied from 470 nm to 1.8  $\mu\text{m}$  as shown in Figure 5.4 by SEM micrographs. We compare results of sample processed by conventional sintering method with 4.5  $\mu\text{m}$  grain size and samples processed with 2-step sintering route. The density of all samples was more than 94% of theoretical one.

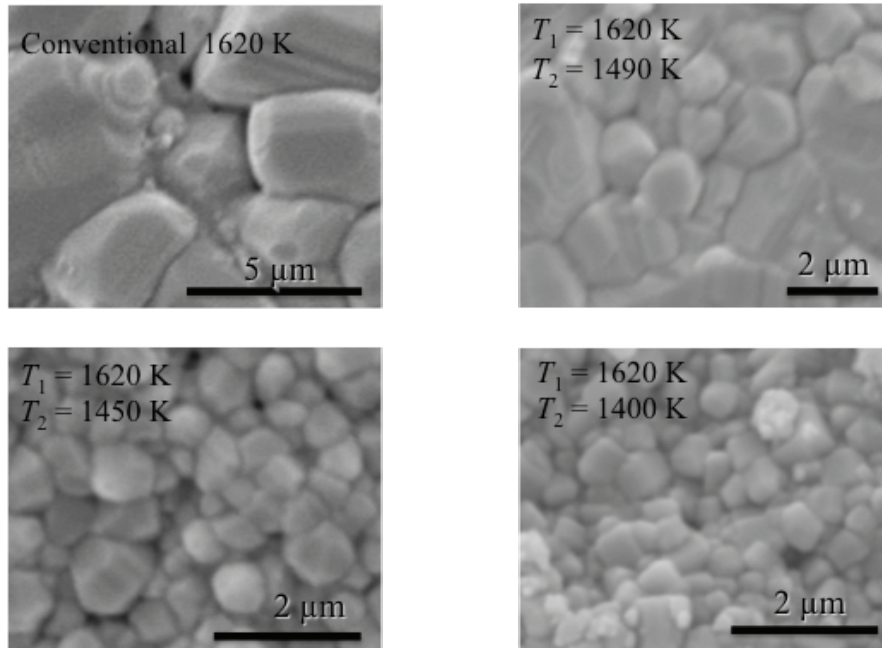


Figure 5.4 Micrographs of samples processed by two-step sintering process. The grain sizes are 1.8  $\mu\text{m}$ , 950 nm and 470 nm for  $T_2$  of 1490 K, 1450 K and 1400 K respectively. Sample sintered at 1620 K has grain size of 4.5  $\mu\text{m}$ . Micrographs provided by Takuya Hoshina.

It is known that the permittivity of BTO family ceramics increases with decreasing the grain size down to values between 1-2  $\mu\text{m}$  and then decreases below that grain size [7-11]. The origin of initial increase is explained by contribution of 90° domain walls to the material response [6]. In contrast, for grain sizes below 1  $\mu\text{m}$ , the dipole and ionic polarizations decrease with decreasing the grain size. In addition, grain boundaries act as pinning centers for the ferroelectric domains, restricting the domain wall motion, which lead to reduction of the bulk polarization [12, 13]. Simultaneously, spontaneous polarization and Curie temperature decrease through grain boundary effect where boundaries impose lattice distortion around themselves. Such distortions destroy the electrical and elastic order of the lattice and consequently suppress the ferroelectricity and the dielectric permittivity. The same concept is valid even at temperatures above  $T_C$  by suppression of polar clusters [13].

Figure 5.5(a) shows the dielectric permittivity as a function of grain size for BST6040 ceramics measured at room temperature at frequency of 1 KHz. Due to the absence of ferroelectric domains there is no contribution from domain walls and the dielectric permittivity was almost constant by changing grain size from 4.5  $\mu\text{m}$  to 1.8  $\mu\text{m}$ . Reducing the grain size below 2  $\mu\text{m}$  decreases the permittivity due to the strain introduced into the crystal lattice through the grain boundary effect, which suppresses ionic and dipole polarizations [14].

### 5.3 Effect of grain size on pyroelectric response of BST6040

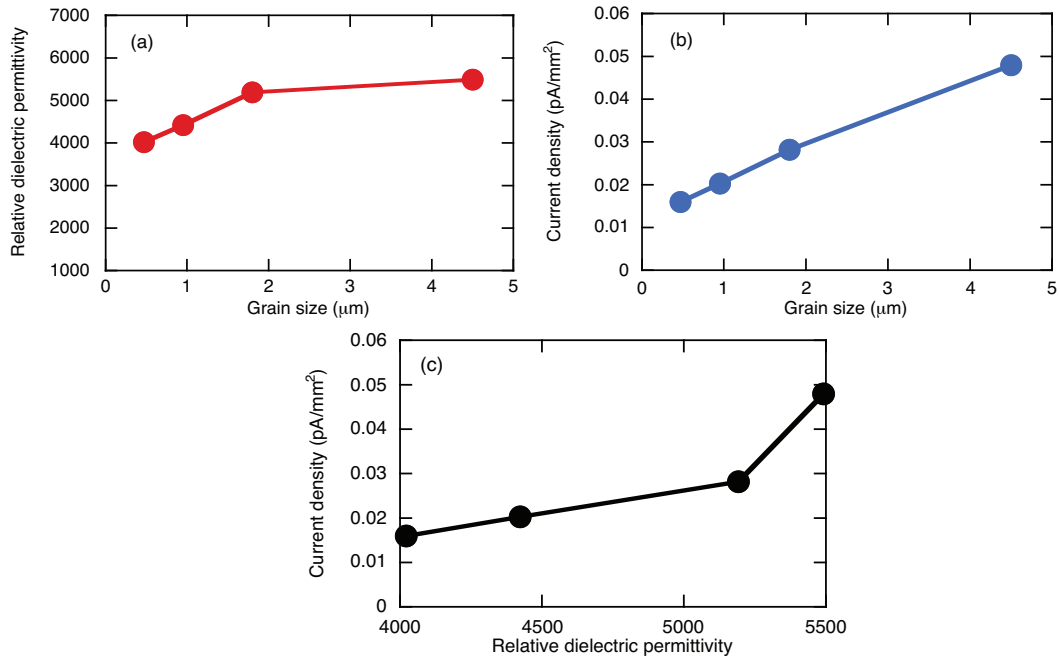


Figure 5.5 (a) dielectric permittivity as a function of grain size (b) pyroelectric current density as a function of grain size and (c) current density versus dielectric permittivity for BST6040.

As presented in Figure 5.5(b) and (c) the pyroelectric current density is decreased by reducing the grain size and the dielectric permittivity in BST6040. It is reasonable to assume that the magnitude of polarization in a polar cluster is reduced by the grain size effect as discussed above and as a result the current amplitude is lowered in samples with smaller grain size.

However, Biancoli has shown that the pyroelectric current for unpoled BTO ceramic with grain size of 50  $\mu\text{m}$  and permittivity of 1800 is 50 times larger than the one in BTO ceramic with grain size of 1  $\mu\text{m}$  and permittivity of 5000 [1]. In addition, he did not observe any proportionality between the dielectric permittivity and the amplitude of the pyroelectric current for entire range of BST solid-solution (Figure 5.6). According to Biancoli's data and considering the fact that different mechanisms could be responsible for magnitudes of the dielectric permittivity and the pyroelectric current, these results give the important insight that the grain size effect and value of the dielectric permittivity by themselves are not the main causes controlling the presence and magnitude of pyroelectric current.

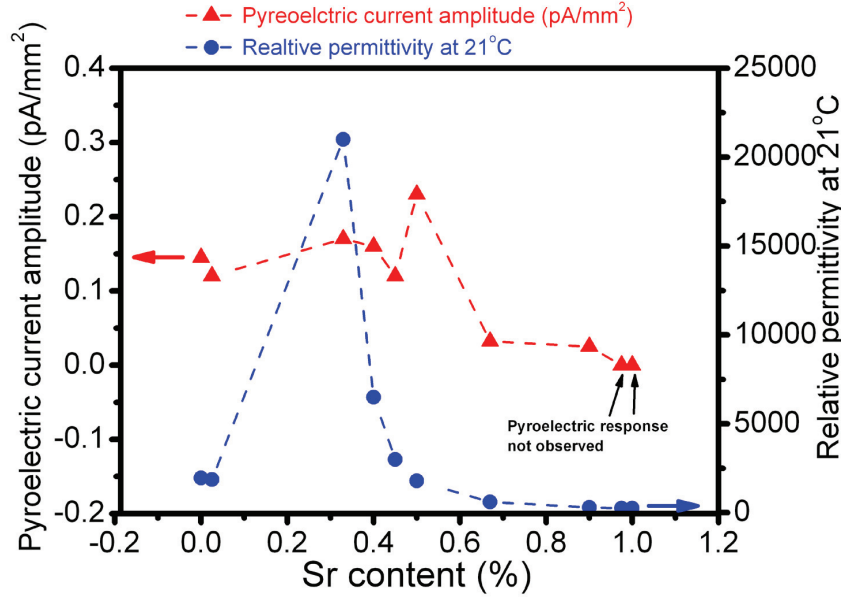


Figure 5.6 Comparison of the pyroelectric current amplitude and dielectric permittivity for different compositions of BST family [1].

## 5.4 Effect of point defects on pyroelectric response of BST6040

Point defects are defined as any deviation from the perfect atomic arrangement in the lattice structure including missing ions, interstitial ions, and their associated valence electrons. In ceramics, point defects could be formed by thermal excitation at high temperature, by the addition of solutes and impurities or by reduction or oxidation process [15]. In ferroelectrics, defects affect different macroscopic properties such as the remnant and spontaneous polarization, the motion of domain walls, the dielectric permittivity, and the leakage current. Oxygen vacancies are thought to be the most mobile and abundant defects among various defects in perovskite ferroelectrics [16]. Several studies discussed essential role of oxygen vacancies in the polarization degradation phenomena [16-19].

We have studied the effect of point defects concentration on the magnitude of pyroelectric current above  $T_C$ . Considering ionic charged defects as a possible origin of symmetry breaking, one would expect that samples with a higher concentration of point defects show larger pyroelectric current compared to pure samples.

0.1% Mn-doped and 0.5% Ti-rich BST6040 samples were provided by prof. Hoshina. Mn has different oxidation states changing from +1 to +7, however +2 and +3 valences are more common. In BST system Mn replace Ti site and act as an acceptor dopant and therefore oxygen vacancies are formed to balance the neutrality of the system. In the case of Ti excess the formed defects are A-site and oxygen vacancies.

As shown in Figure 5.7 for both cases, the magnitude of pyroelectric current has been reduced as the point defects concentration has been increased in the material. These results rule out

#### 5.4 Effect of point defects on pyroelectric response of BST6040

charge defects as the main polar entities responsible for the symmetry breaking. As discussed above, if the charged defects were the main contributors to the build-in polarization, the pyroelectric current should have been larger in doped samples compared to undoped ones.

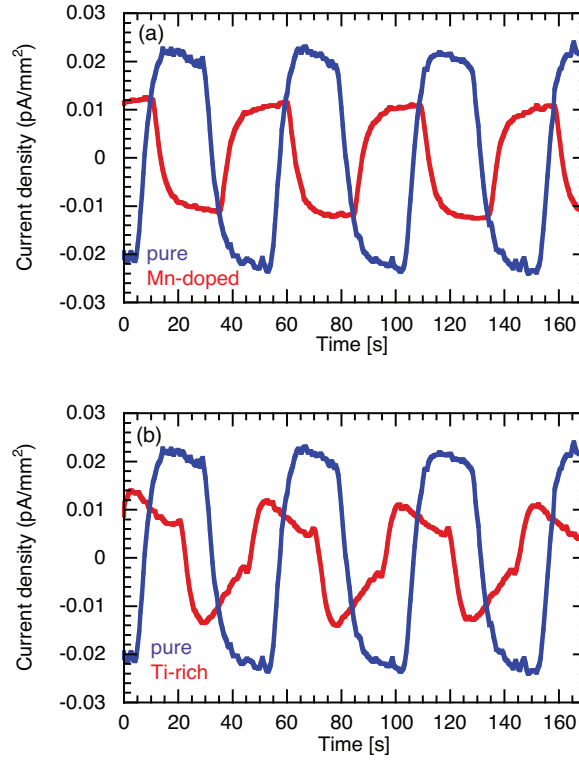


Figure 5.7 Comparison between amplitude of pyroelectric current of pure BST6040 sample with (a) Mn-doped sample, and (b) Ti-rich sample.

It's known that ferroelectricity is due to relatively 'long-range' interactions of dipoles; perturbation of this continuity is expected to weaken the stability of the ferroelectric phase [20]. As illustrated in Figure 5.8 in analogy to ferroelectricity, we believe that introduction of point defects in the lattice results in the violation of polarization continuity in polar clusters in paraelectric phase and results in smaller pyroelectric current compared to pure samples.



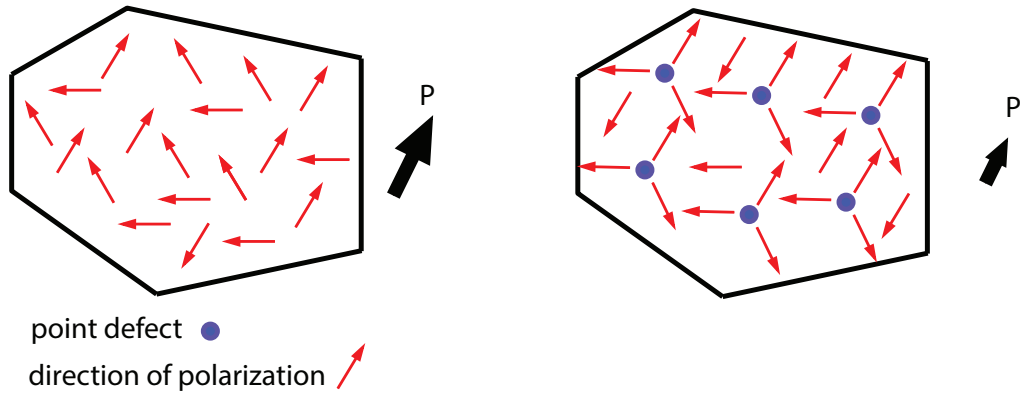


Figure 5.8 Schematic suppression of macroscopic polarization in material by doping.

## 5.5 Summary

In this chapter we have investigated effects of processing conditions, grain size and point defect concentration on the evolution of nominally forbidden pyroelectric response above Curie temperature for BST6040. Our results suggest that the symmetry breaking is a general phenomenon in perovskite materials and is not limited to a specific processing method or starting materials. Grain size could play a role on the magnitude of pyroelectric current but it is not the dominant mechanism governing the symmetry breaking. Finally, suppression of the pyroelectric response by increasing the concentration of point defects in the samples support the idea that point defects are not the principal charged entities responsible for the symmetry breaking.

## Bibliography

- [1] A. Biancoli, "Breaking of the macroscopic centric symmetry in  $\text{Ba}_{1-x}\text{Sr}_x\text{TiO}_3$  ceramics and single crystals," 2014.
- [2] F. Lenel, H. Hausner, O. Roman, and G. Ansell, "The influence of gravity in sintering," *Powder Metallurgy and Metal Ceramics*, vol. 2, pp. 379-384, 1963.
- [3] C. Elissalde, U. Chung, A. Artemenko, C. Estournes, R. Costes, M. Pate, *et al.*, "Stoichiometry and grain boundaries control by spark plasma sintering in  $\text{Ba}_{0.6}\text{Sr}_{0.4}\text{TiO}_3$ : Mn/MgO composites," *Journal of the American Ceramic Society*, vol. 95, pp. 3239-3245, 2012.
- [4] C. Elissalde, M. Maglione, and C. Estournes, "Tailoring dielectric properties of multilayer composites using spark plasma sintering," *Journal of the American Ceramic Society*, vol. 90, pp. 973-976, 2007.
- [5] A. Biancoli, C. M. Fancher, J. L. Jones, and D. Damjanovic, "Breaking of macroscopic centric symmetry in paraelectric phases of ferroelectric materials and implications for flexoelectricity," *Nature materials*, vol. 14, pp. 224-229, 2015.
- [6] T. Hoshina, Y. Kigoshi, S. Hatta, H. Takeda, and T. Tsurumi, "Domain contribution to dielectric properties of fine-grained  $\text{BaTiO}_3$  ceramics," *Japanese Journal of Applied Physics*, vol. 48, p. 09KC01, 2009.
- [7] G. Arlt, D. Hennings, and G. De With, "Dielectric properties of fine - grained barium titanate ceramics," *Journal of applied physics*, vol. 58, pp. 1619-1625, 1985.
- [8] M. Frey, Z. Xu, P. Han, and D. Payne, "The role of interfaces on an apparent grain size effect on the dielectric properties for ferroelectric barium titanate ceramics," *Ferroelectrics*, vol. 206, pp. 337-353, 1998.
- [9] T. Hoshina, T. Furuta, Y. Kigoshi, S. Hatta, N. Horiuchi, H. Takeda, *et al.*, "Size effect of nanograined  $\text{BaTiO}_3$  ceramics fabricated by aerosol deposition method," *Japanese Journal of Applied Physics*, vol. 49, p. 09MC02, 2010.
- [10] K. Kinoshita and A. Yamaji, "Grain - size effects on dielectric properties in barium titanate ceramics," *Journal of Applied Physics*, vol. 47, pp. 371-373, 1976.
- [11] A. V. Polotai, A. V. Ragulya, and C. A. Randall, "Preparation and size effect in pure nanocrystalline barium titanate ceramics," *Ferroelectrics*, vol. 288, pp. 93-102, 2003.
- [12] S. Mantri, J. Oddershede, D. Damjanovic, and J. E. Daniels, "Ferroelectric domain continuity over grain boundaries," *Acta Materialia*, vol. 128, pp. 400-405, 2017.
- [13] T. Hoshina, "Size effect of barium titanate: fine particles and ceramics," *Journal of the ceramic society of Japan*, vol. 121, pp. 156-161, 2013.
- [14] T. Yamazaki, T. Hoshina, H. Takeda, and T. Tsurumi, "Polarization Mechanism of Fine-grained  $\text{BaTiO}_3$  Ceramics at High Temperature Region," in *Key Engineering Materials*, 2013, pp. 12-15.
- [15] P. M. Rice, W. D. Kingery, H. Bowen, D. R. Uhlmann, G. Y. Onoda, L. L. Hench, *et al.*, "Physical ceramics: principles for ceramic science and engineering," 1997.
- [16] C. Park and D. Chadi, "Microscopic study of oxygen-vacancy defects in ferroelectric perovskites," *Physical Review B*, vol. 57, p. R13961, 1998.

- [17] W. L. Warren, D. Dimos, and R. M. Waser, "Degradation mechanisms in ferroelectric and high-permittivity perovskites," *MRS bulletin*, vol. 21, pp. 40-45, 1996.
- [18] H. Duiker, P. Beale, J. Scott, C. Paz de Araujo, B. Melnick, J. Cuchiaro, *et al.*, "Fatigue and switching in ferroelectric memories: Theory and experiment," *Journal of Applied Physics*, vol. 68, pp. 5783-5791, 1990.
- [19] D. Smyth, "Charge motion in ferroelectric thin films," *Ferroelectrics*, vol. 116, pp. 117-124, 1991.
- [20] D. Damjanovic, "Ferroelectric, dielectric and piezoelectric properties of ferroelectric thin films and ceramics," *Reports on Progress in Physics*, vol. 61, p. 1267, 1998.



## Chapter 6. Nonlinear behavior of polar entities

### 6.1 Introduction

In this chapter the dielectric nonlinearity of barium strontium titanate ( $\text{Ba}_{1-x}\text{Sr}_x\text{TiO}_3$ ) ceramics is investigated in the paraelectric phase. BST is technologically interesting for the high tunability of its dielectric permittivity at microwave frequencies. The goal is to identify mechanisms governing the dielectric nonlinearity by analyzing the amplitude and the phase angle of the first and the third harmonics of polarization. The work presented in this Chapter has been published in part in Applied Physics Letter entitled as “Nonlinear dynamics of polar regions in paraelectric phase of ( $\text{Ba}_{1-x}\text{Sr}_x\text{TiO}_3$ ) ceramics” [1].

### 6.2 Polar entities

The study of short-range polar entities in ferroelectric and related materials attracted a lot of attention because of their contribution to dielectric, piezoelectric and mechanical properties. Polar entity is a general term that describes a nanoscale region with polar order. It may refer to different phenomena like precursors of the ferroelectric phase just above the Curie temperature [2, 3], Känzig regions in  $\text{BaTiO}_3$  [4-5], the appearance of polar nano-regions (referred as PNR in this text) at the Burns temperature in nonpolar phase of complex solid solutions such as  $(\text{La,Pb})(\text{Zr,Ti})\text{O}_3$  that related to mixed cations [6], PNRs embedded in long-range polar domains in  $\text{Pb}(\text{Mn}_{1/3}\text{Nb}_{2/3})\text{O}_3$ - $\text{PbTiO}_3$  [7], polar boundaries in complex tweed structures in ferroic materials [8, 9] and defects-induced polar regions appearing above  $T_C$  [10]. Polar regions could have significant or even dominant contribution to material properties however their chemistry and physics are not fully understood. The large piezoelectric effect above  $\sim 150$  K in relaxor-ferroelectrics [7], the large and frequency dispersive dielectric permittivity in relaxors [11, 12], the flexoelectric coupling in relaxor-ferroelectrics [13-16] and the macroscopic polarization in nominally nonpolar phases observed in ferroelectric materials [17] are few examples of mentioned contributions to properties.

Existence of polar regions and their contribution to dielectric loss has been indicated both in bulk ceramics [18] and thin films [19] of paraelectric ( $\text{Ba}_{1-x}\text{Sr}_x\text{TiO}_3$ ). Two reasons motivated us to study the effect of short-range polar regions on polarisation response in paraelectric phase of ( $\text{Ba}_{1-x}\text{Sr}_x\text{TiO}_3$ ) solid solution. First, it's believed that unexpected macroscopic polarization of BST compositions in their paraelectric phase [17-20] is due to the alignment of polar regions and second, the largest flexoelectric coefficient above  $T_C$  is reported for BST [21, 22]. Its flexoelectric coefficient value is so large that it could not been reconciled easily with theoretical predictions [23-26] (see chapter1). Garten et al. [14-16] suggested that large apparent flexoelectric coefficients in thin films of ( $\text{Ba}_{1-x}\text{Sr}_x\text{TiO}_3$ ) is due to the flexoelectric polarization enhancement by residual ferroelectric domains (polar domains that remain in the material when it is heated above  $T_C$ ), similar to what was reported for the paraelectric phase of a single crystal relaxor-ferroelectric by Narvaez and Catalan [13]. Garten also proposed that their ability to permanently polarize their films by simple bending is originated from the alignment of residual ferroelectric domains. Moreover, the increase of the ( $\text{Ba}_{1-x}\text{Sr}_x\text{TiO}_3$ ) dielectric permittivity with respect to electric field

### 6.3 Rayleigh law

amplitude that they have observed in nonlinear measurement was interpreted in terms of Rayleigh-type dynamics [27] of residual domain walls. They considered this nonlinearity as another indication that polar entities responsible for the polarization and the large flexoelectric effect in the films are residual ferroelectric domains. However, it's extremely important to notice that the polarization in paraelectric phase of  $(\text{Ba}_{0.6}\text{Sr}_{0.4})\text{TiO}_3$  ( $T_c = 273$  K) has been observed in samples that have never experienced ferroelectric phase, so polar entities should not be called "residual" ferroelectric domains but rather "precursors" of the ferroelectric phase [2, 3, 8, 9] or polar regions [6]. Moreover, it is essential to understand the exact nature and origin of the polar entities in these materials in order to uncover the mechanisms leading to large flexoelectric effect and macroscopic polarization, which could be different from each other.

Studying the material response to dynamic electric field could provide significant information on the nature of polar entities. In this chapter, we present results of a study where we used higher harmonics analysis of the nonlinear polarization to distinguish between domain wall-like dynamics of residual ferroelectric domain walls or polar regions above  $T_c$ , proposed by Garten, from other types of local polar regions dynamics [28, 29]. This topic is in the heart of the debate on the nature of polar nano regions in ferroelectric and relaxor materials [30, 31].

Principles of Rayleigh behavior and higher harmonic analysis are discussed in the next two sections.

### 6.3 Rayleigh law

Rayleigh [32] originally showed that in some ferromagnetic materials, the magnetic susceptibility  $\chi$  is linearly related to the magnetic field  $H$  during the first magnetization of the material under low field conditions:

$$\chi(H) = \chi_{\text{init}} + \alpha H \quad 6.1$$

Where  $\chi_{\text{init}}$  is the initial susceptibility and  $\alpha$  is Rayleigh coefficient. Susceptibility is defined as proportion of magnetization over magnetic field ( $\chi = M/H$ ). The magnetization curve is given by:

$$M(H) = \chi_{\text{init}}H + \alpha H^2 \quad 6.2$$

Rayleigh proposed that in equation 6.2 the linear term stands for instantaneous or reversible component of the magnetization and the quadratic part represents the irreversible component. Néel [33] was the first one who tried to explain the physical origins of Rayleigh law by analyzing displacement of a single domain wall in a medium with defects. He proposed that defects in a material introduce irregular perturbations of the potential energy for domain wall motion (Figure 6.1) and displacement of domain walls in such medium results in material magnetization with Rayleigh characteristics (reversible linear component and irreversible quadratic component).

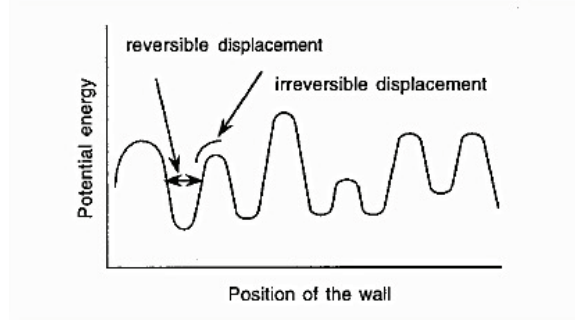


Figure 6.1 Energy profile domain wall motion in medium with random pinning centers [33].

The reversible part of the magnetization is due to the movement of the domain wall inside of a potential energy minimum and from the intrinsic response. On the other hand, the irreversible domain wall motion and the dependence of the magnetic susceptibility on the external field occur when the applied force is sufficiently large to overcome the potential barrier separating two local energy minima. Thus the Rayleigh coefficient could be counted as a measure of the irreversible displacement of the domain wall [34].

Many researches have been carried out to explain the domain wall contribution to dielectric, elastic and piezoelectric properties of ferroelectric materials [35-38]. Most of the early studies were focused on nucleation, growth and switching of domain walls, on the other hand domain wall response to subcoercive fields (electric or elastic) has been less investigated [39, 40]. Recently it has been shown that in many cases, pinning of domain walls may be treated quite generally as interface pinning with similar theoretical analysis whether the interface is a ferromagnetic domain wall, a liquid-liquid interface, or a ferroelectric domain wall [41]. This implies universal validity of the Rayleigh law for the domain wall displacements in all ferroic – ferromagnetic, ferroelectric and ferroelastic materials. The applicability of this general approach to the weak field displacement of ferroelectric domain walls has been confirmed experimentally [42, 43]. Under weak fields, domain walls vibrate or have small displacement and their overall distribution within material does not change. Typically, as a consequence of domain wall motion, ferroelectric materials show electro-mechanical response that is nonlinear and hysteretic function of applied subcoercive fields [34]. In the case of the dielectric polarization response, the Rayleigh equations are:

$$\begin{aligned}\varepsilon(E_0) &= \varepsilon_{\text{init}} + \alpha E_0 \\ P(E_0) &= (\varepsilon_{\text{init}} + \alpha E_0)E_0\end{aligned}\tag{6.3}$$

Where  $\varepsilon$  is the relative dielectric permittivity,  $E_0$  is the applied electrical field,  $P$  is the material polarization and  $\alpha$  is the Rayleigh coefficient. If the applied field is cycled, material response for increasing and decreasing field is not the same. Rayleigh showed that the weak field hysteresis loop could be described by the following nonanalytical relationship:

#### 6.4 Higher harmonics analysis of dielectric polarization

$$P(E) = (\varepsilon_{\text{init}} + \alpha E_0)E \pm \alpha(E_0^2 - E^2)/2 + \dots \quad 6.4$$

Where “-” stands for increasing fields and “+” for decreasing fields. This is the reason why the term with  $\alpha$  in 6.3 is called irreversible term. The main feature of the equation is the link between the nonlinearity and hysteresis. As long as this link is present we refer to the system as Rayleigh-like. It should be noted that domain walls in ferroelectrics may exhibit and often do a different dynamics from that described by Eq. 6.4 (for example hard PZT) [44, 45]. Origin of the dielectric hysteresis and the stress dependence of the dielectric permittivity is a combination of the reversible and irreversible displacement of domain walls. The Rayleigh relationships are in a good agreement with experimental data for low fields, while for higher values of field it is necessary to fit the data with a higher order polynomial. It is important to note that for more complete description of a real, non-ideal material, equation 6.4 may possess additional terms reflecting the degree of randomness of the energy profile [33, 46].

#### 6.4 Higher harmonics analysis of dielectric polarization

Investigation of an ac-signal through its harmonic amplitudes and phase angles is useful to study the nonlinear systems. The harmonic analysis by using discrete Fourier transform permits the separate study of different contributions to nonlinearity if the material response is result of several contributions differently depending on time. Based on Fourier transformation principles, it's possible to decompose any existing waveform into an equivalent series of sine waves with possible phase shift and a dc component, such presentation of waveform in time and frequency domain will include same information but in different form [47-49].

For higher harmonic analysis of polarization response due to applied electric field it is convenient to define a periodic sine signal:

$$E = E_0 \sin(\omega t) \quad 6.5$$

The perfect symmetrical response of material (polarization in this case)  $P(E) = -P(-E)$  results in half-wave symmetry:

$$P(\omega t) = -P(\omega t + \pi) \quad 6.6$$

Half-wave symmetry of polarization exists in non-textured and non-poled ceramics with the random orientation of grains. In this case by implementing the Fourier transform, the amplitudes of all even harmonics would be zero and polarization is written as:

$$P(t) = P'_1 \sin(\omega t) + P''_1 \cos(\omega t) + P'_3 \sin(3\omega t) + P''_3 \cos(3\omega t) + P'_5 \sin(5\omega t) + P''_5 \cos(5\omega t) + \dots \quad 6.7$$

The phase angle  $\delta_n$  and amplitude  $P_n$  of the  $n^{\text{th}}$  harmonic of the polarization is defined by:



$$P = \sum_n P_n \sin(n\omega t + \delta_n)$$

$$P_n = \sqrt{(P'_n + P''_n)} \quad 6.8$$

$$\delta_n = \arctan \frac{P''_n}{P'_n}$$

Equation 3.14 indicates how polarization and dielectric permittivity is calculated for each harmonic. Different cases of polarization could be considered as references, first is material response due to the domain wall motion in a random potential energy profile described by Rayleigh equations, [44]. Equation 6.4 presents the Fourier expansion of Rayleigh relation for polarization:

$$P(E) = (\epsilon_{\text{init}} + \alpha E_0)E_0 \sin(\omega t) - \frac{4\alpha E_0^2}{3\pi} \cos(\omega t) - \frac{4\alpha E_0^2}{\pi} \left[ \frac{1}{15} \cos(3\omega t) - \frac{1}{105} \cos(5\omega t) + \dots \right] \quad 6.9$$

There are few interesting key features that could be extracted from equation 6.9:

- i) The absence of even harmonics is a consequence of half-wave symmetry, which assumes the system is symmetric with respect to the driving field direction. It is only an approximation for a real sample [44, 45].
- ii) All harmonics are out-of-phase with the driving field, meaning that they contribute to both the hysteresis and nonlinearity.
- iii) All higher harmonics are quadratic functions of the field amplitude.
- iv) Phase angle  $\delta_n$  of all higher harmonics is  $\pm 90^\circ$ .

The above features give us the ability to identify the Rayleigh behavior experimentally.

In the second case, anhysteretic but nonlinear response of material is consequence of domain wall motion in a regular V-shaped potential, which explain the behavior of hard clamped domain walls. Another limiting case of polarization is linear anhysteretic polarization that could be the case for material without ferroelectric domains. In this case, the intrinsic material response is described by parabolic potential and cannot be explained by Rayleigh model. Higher harmonic analysis of this behavior would include only non-zero first harmonic amplitude that is in-phase with the driving field. Field-induced changes in the intrinsic (lattice) properties become important only at very large fields, which are not of interest for this discussion [44].

## 6.5 Results and discussion

In this section we report results for  $\text{Ba}_{0.6}\text{Sr}_{0.4}\text{TiO}_3$  (BST6040), and two end-members of the BST solid solution,  $\text{BaTiO}_3$  (BTO) and  $\text{SrTiO}_3$  (STO) (all the nonlinear measurements were done at a frequency of 1 kHz). BST6040 is paraelectric at room temperature. BTO was examined both in ferroelectric and paraelectric states. BTO's polarization response at room temperature is dominated by domain wall motion (it is ferroelectric with tetragonal structure). STO is an incipient ferroelectric with cubic structure with dielectric permittivity independent on electric field at room temperature. BTO and STO are used as a reference for Rayleigh and quasi-linear dielectric material respectively. The dielectric nonlinearity in  $\text{Pb}(\text{Mg}_{1/3}\text{Nb}_{2/3})\text{O}_3$  PMN (a typical lead-based

relaxor) and other compositions of BST ceramics (BST1090-BST3367-BST5050) are investigated for comparison with BST6040.

Most studies and models of the dielectric nonlinearity place emphasis on the amplitude of the nonlinear response, however, we also investigated field dependence of the phase angle of the third harmonic. Such information can directly reveal wheather nonlinear contributions exhibit hysteretic character or not. Moreover, phase angle study is interesting to test for the presence of the Rayleigh-like dynamics[29].

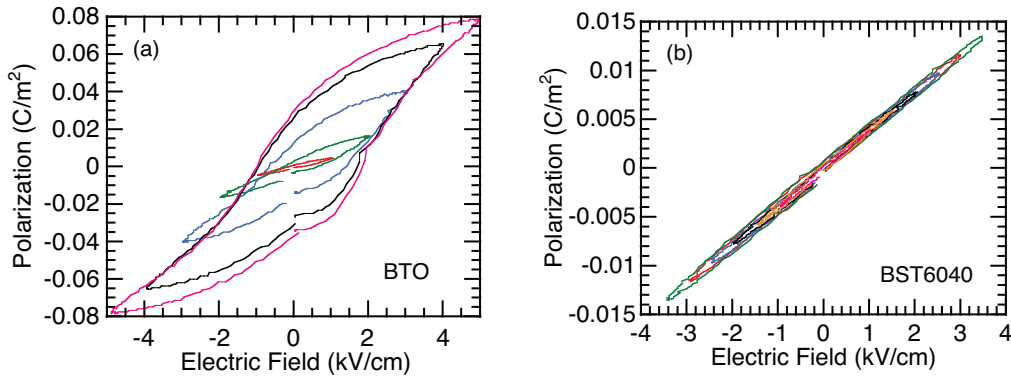


Figure 6.2 (a) BTO at room temperature and (b) BST6040 hysteresis loops.

Figure 6.2 shows P-E loops for BTO and BST6040 samples at 50 Hz. The coercive field for measured BTO sample is 1.5 kV/cm. The Rayleigh behavior was checked in sub-switching conditions (up to 0.75 kV/cm) to insure that motion of units responsible for Rayleigh-like behavior (e.g., domain walls in ferroelectrics) does not become governed by another process with different P-E relationship at larger fields (such as nucleation of domains). Figure 6.2 (b) shows hysteresis loops for paraelectric BST6040 at room temperature for selected fields up to the highest field used in this work. If BST6040 was ferroelectric at room temperature, all these loops would have characteristics of ferroelectric Rayleigh loops similar to BTO (which is not the case here). The slim loops indicate low leakage losses even at highest ac fields applied.

Results of harmonic analysis of a BTO sample at room temperature are plotted in Figure 6.3. At fields above  $\approx 0.35$  kV/cm, the field dependent behavior of the real part of the permittivity suggests the Rayleigh-like behavior as may be expected for a relatively soft ferroelectric material, Figure 6.3(a). The change of the slope below this threshold field signifies that the energy profile is not perfectly random [50].

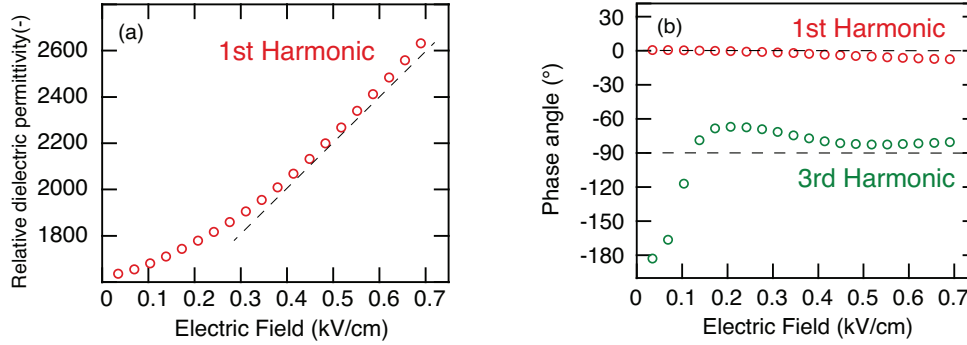


Figure 6.3 (a) The 1<sup>st</sup> harmonic relative dielectric permittivity and (b) the 1<sup>st</sup> and the 3<sup>rd</sup> harmonics phase angle of the polarization for a BTO sample. The dashed line in (a) indicates transition into linear, Rayleigh-like regime. The horizontal dashed lines in (b) show values expected from the ideal Rayleigh-like behavior, as predicted by Eq. (1). Measurements were done at room temperature.

Due to the low coercive field of BTO, the field dependence of the permittivity is nontrivial and the focus here is to investigate the nonlinear hysteretic behavior of the material by monitoring the phase angle of the third harmonic. The value of the phase angle of different harmonics could verify the presence of a Rayleigh-like mechanism. As predicted by Eq. 6.4, Figure 6.3 (b) shows that the phase angle of the 1<sup>st</sup> harmonic ( $\delta_1$ ) is near zero at larger fields while the phase angle of the 3<sup>rd</sup> harmonic ( $\delta_3$ ) is close to  $-90^\circ$ . Note that the out-of-phase (quadrature) component of the first harmonic is non-zero (dielectric loss data for BTO), but its amplitude is relatively small with respect to the in-phase component, leading to a nonzero but small  $\delta_1$ . The nonlinear motion of domain walls is strongly hysteretic as indicated by the value of the  $\delta_3$  (roughly around  $-90^\circ$ ). The rapid change of  $\delta_3$  from  $-180^\circ$  to  $\sim -90^\circ$  is consistent with the threshold field observed in Figure 6.3(a) and could be due to non-uniform distribution of potential energy barriers (the barriers' heights may not extend uniformly all the way to zero) [27].

At weak fields, the value of the phase angle is around  $-180^\circ$ . This behavior is consistent with the anhysteretic displacement of domain walls in potential wells that are too deep to be overcome by the applied electric field. Once the field is strong enough, the domains are able to depin from defects and move in a hysteretic, nonlinear, irreversible fashion, indicated by the phase angle of  $\delta_3$  approaching  $-90^\circ$ . At fields higher than 0.8 kV/cm, the occurrence of large-scale switching leads to saturation of the lock-in amplifier and data were not reliable.

Figure 6.4 shows harmonic analysis of an STO ceramic. The relative dielectric permittivity determined from the amplitude of the 1<sup>st</sup> harmonic, the phase angles of the 1<sup>st</sup> ( $\approx 0^\circ$ ) and the 3<sup>rd</sup> ( $-180^\circ$ ) harmonics are nearly independent of the electric field. Therefore, contribution of the first and the small third harmonic to the polarization is essentially anhysteretic because the angles are not perfectly  $0^\circ$  or  $-180^\circ$  small hysteresis is present. STO behavior is neither (strongly) nonlinear nor hysteretic at these fields and, at room temperature if it contains any polar entities, their contribution to polarization is small and their dynamics cannot be described by Rayleigh behavior.

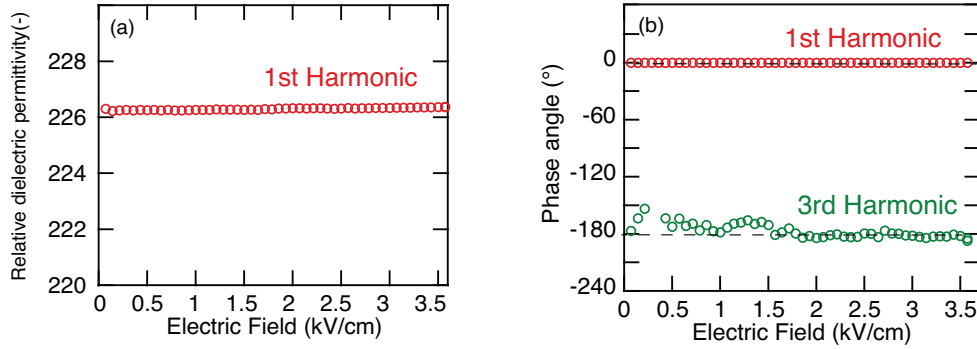


Figure 6.4 Real part of the relative dielectric permittivity for the first harmonic and the phase angles of the 1st and the 3rd harmonics for STO measured at room temperature. Dashed lines represent the expected values for phase angles of the 1<sup>st</sup> and the 3<sup>rd</sup> harmonics for an ideal linear, anhysteretic material.

The breaking of the cubic symmetry in the paraelectric phase of BST6040 is confirmed by pyroelectric measurements (see chapter 5). It has been suggested that the origin of such symmetry breaking could be associated with the orientation of polar entities by a strain gradient [14-17]. We measured and analyzed nonlinear polarization response in BST6040 samples to get more information on the nature of these polar objects. It is possible to consider the following two verifiable cases: (i) polar objects show dynamics similar to that of domain walls in soft ferroelectrics resulting in the Rayleigh-like behavior of polarization. In this situation, the response should be qualitatively similar to that in the BTO sample shown in Figure 6.3 and should exhibit nonlinearity and hysteresis in all higher odd harmonics (ideally non-zero quadrature and zero in-phase components of polarization); and (ii) the dynamics of local polar entities leads to a nonlinear but nearly anhysteretic response similar to response of polar-entities in the ergodic phase of PMN [29]. Ideally in this case, the higher harmonics of polarization are non-zero for in-phase and are zero for out of phase components.

The permittivity data for the first harmonic and  $\delta_3$  are shown for a BST6040 and a PMN sample in Figure 6.5. We discuss and show a similar set of data for different BST6040 samples in Figure 6.6. In the Figure 6.6(a) and (b) sample (i) has never experienced ferroelectric phase after cooling from sintering temperature and sample (ii) was cooled to 263 K, about 10K below  $T_C$ , and then heated again to room temperature. A close inspection of sample (i) shows that it probably exhibits a maximum in the permittivity at weak fields, which is, however, lost in the noise in the data (inset of Figure 6.6(a)). The permittivity increases with increasing field at low fields, followed by a negative nonlinearity for high fields in all samples.

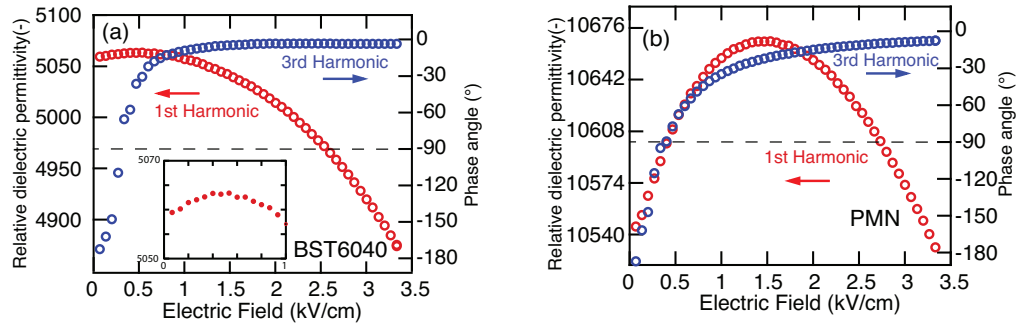


Figure 6.5 The real part of the relative dielectric permittivity measured at the first harmonic and the phase angle of the third harmonic at room temperature for: (a) a BST6040 ceramic sample with no history of the ferroelectric phase transition and (b) a PMN ceramic. Dashed lines represent expected values for the phase angle of the 3<sup>rd</sup> harmonic for a material with the Rayleigh-like behavior. Inset in (a) shows the maximum in permittivity at low fields.

Figure 6.6(c) is related to the sample that has been prepared at Tokyo Institute of Technology, by T. Hoshina. It has not been cooled through  $T_C$ . The grain size of sample is on the order of 2-4  $\mu\text{m}$ , while our samples (Fig. 6.6(a) and Fig. 6. (c)) exhibit grain size  $>20 \mu\text{m}$ .

It is interesting that nonlinear behavior of different BST6040 and PMN samples is qualitatively similar (specifically see PMN data in Figure 6.5 (b) and data for a BST6040 sample in Figure 6.6 (c)). The microstructure and history affect the nonlinear behavior, but it still remains qualitatively similar for all samples. Thin films of PMN and BST have shown exactly the same dependence of the permittivity with respect to ac field [51, 52]. Significantly, thin films of BST in Ref. [53] exhibit relaxor behavior while our ceramics behave as "normal" ferroelectrics (see chapter 2), however, their behaviors above  $T_{\text{max}}$  (films) and  $T_C$  (ceramics) are similar.

Two mechanisms could be related to the decrease of the permittivity at high fields: (i) "tunability" of the permittivity [54] and (ii) reorientation of polar entities followed by their response saturation at high fields [51, 55-57]. Tunability discusses the decrease of the permittivity with increasing dc field strength due to the dependence of intrinsic lattice polarization response on static fields. A qualitatively similar behavior of the dielectric nonlinearity may be derived for alternating fields by using a simple phenomenological model of a nonlinear, centrosymmetric dielectric [55-57]. Thus, we cannot conclude what is the exact origin of the negative nonlinearity at higher fields in these samples just on the basis of the present data. While the two mechanisms can act simultaneously, our data and previous studies are consistent with the interpretation regarding dominant contribution from orientable polar entities at high fields [51, 54, 55].

At weak fields, where polarization response is dominated by the contribution of polar entities, the situation is clearer. In this region the permittivity usually increases with respect to the field amplitude, for example, due to the displacement of domain walls, or "breathing" of polar regions. Thus, the initial increase of the permittivity with increasing field in our samples suggests presence of some kind of electrically active polar entities above the Curie temperature.

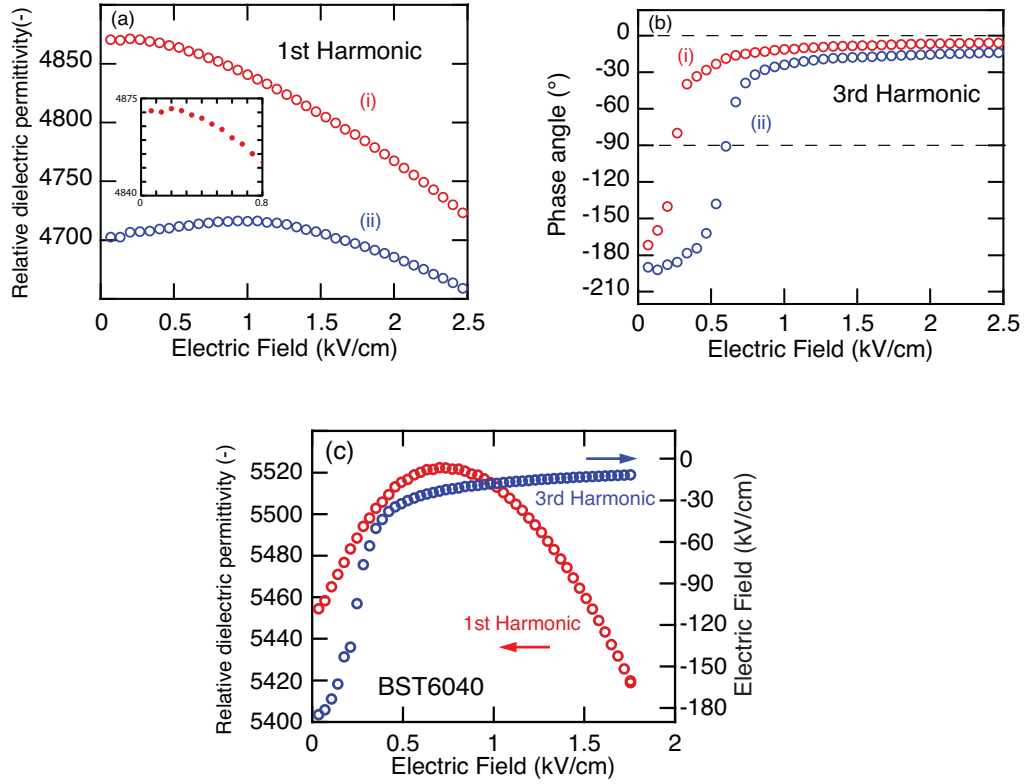


Figure 6.6 BST6040 samples with different histories and preparation conditions. (a) and (b): sample experienced ferroelectric phase by cooling down below  $T_C$ . (c) The sample prepared in Japan All samples show qualitatively similar nonlinear behavior. Compare with data shown in for BST6040 and PMN.

We next discuss the phase angle of BST6040 samples in the two main regimes that can be identified in Figure 6.5 and Figure 6.6. The phase angle of the 3<sup>rd</sup> harmonic globally approaches either  $\approx 0^\circ$  or  $\approx -180^\circ$ , meaning that the amplitude of the out of phase component of the nonlinear polarization for this harmonic is close to zero. This behavior is similar to that previously suggested for PMN [29] and confirmed experimentally here (see Figure 6.5(b)). The physical meaning of the values of  $0^\circ$  and  $-180^\circ$  for phase angle of the 3<sup>rd</sup> harmonic is the following: both of them are ideally anhysteretic, when  $\delta_3 \approx -180^\circ$ , the third harmonic increases the amplitude of the total polarization but phase angle of  $0^\circ$  decreases the response amplitude. These effects agree well with the trend in the permittivity that increases at first and then decreases when  $\delta_3$  shifts towards zero. Rayleigh equation which requires the  $\delta_3$  to be close to  $-90^\circ$  does not predict either the evolution of the  $\delta_3$  nor the permittivity with the field amplitude.

Figure 6.7 represents the normalized 1<sup>st</sup> harmonic of the dielectric permittivity and the 3<sup>rd</sup> harmonic phase angle for different BST compositions (BST6040-BST5050-BST3367 and BST1090). In BST system, by decreasing the barium content the Curie phase transition shifts to lower temperatures. At room temperature the intensity and coupling effect of polar entities is expected to be less for compositions with lower  $T_C$ . As shown in Figure 6.7 (a) the nonlinearity

decreases by increasing of the Sr content to the point that BST1090 response is almost similar to that of STO. The anhysteretic transition of the phase angle from  $-180^\circ$  to  $0^\circ$  is shifted to higher fields by decreasing the intensity of polar entities.

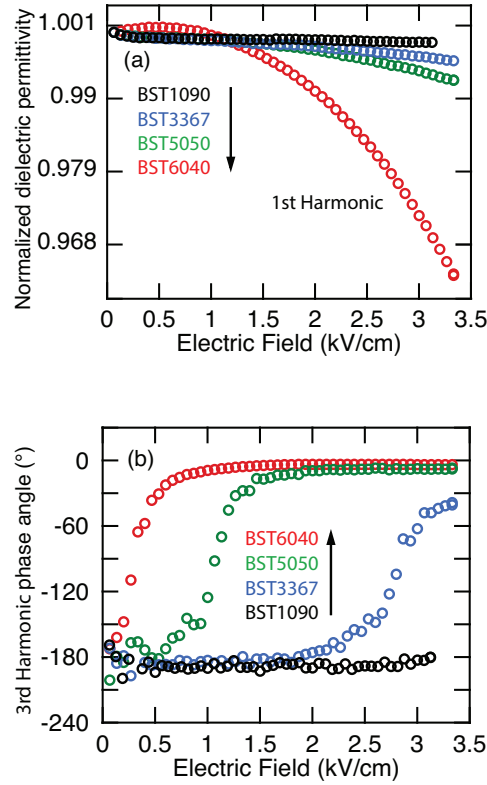


Figure 6.7 Normalized dielectric permittivity and  $\delta_3$  for BST samples with 10, 33, 50 and 60% Ba. The dashed line shows value of  $\delta_3$  expected for a Rayleigh-like nonlinear process.

Like BST, BTO has shown macroscopic polarization above its Curie temperature that might be associated with the presence of polar entities. To investigate this claim we also examined the nonlinear response of BTO samples above  $T_C$ . Figure 6.8 indicates that the BTO sample exhibits nonlinear permittivity that increases with increasing field some twenty degrees above its  $T_C$  (390 K). The  $\delta_3$  rapidly evolves from  $\sim -180^\circ$  toward  $\sim 0^\circ$  at weak fields and then shows a tendency to stabilize toward  $0^\circ$  at large fields similar to BST6040 and PMN. Considering the trend in  $\delta_3$ , we anticipate a possible maximum and then a decrease in the permittivity at higher fields than used here. If true for  $\text{BaTiO}_3$ , the nonlinear behavior described in this chapter is not exclusively due to chemical inhomogeneities at cation sites. Clearly, over the examined field range the BTO sample does not exhibit a dielectric nonlinearity that can be described by Rayleigh equation.

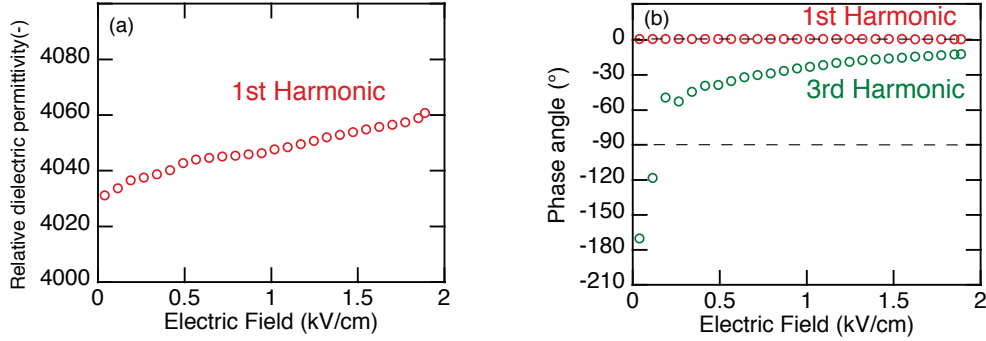


Figure 6.8 (a) The real part of the relative dielectric permittivity measured at the first harmonic and (b) the phase angle of the first and the third harmonic for a BTO sample. All measurements were made above  $T_C$ , at 413 K. Dashed lines represent the expected values for the phase angles of the 1<sup>st</sup> and 3<sup>rd</sup> harmonics of a material with the Rayleigh-like behavior.

In section 6.4 we stated that the absence of even harmonics is a consequence of the half-wave symmetry. One could argue that the half-wave symmetry cannot be valid for samples that have shown symmetry breaking. However, we believe that there is no contradiction here. Even if the material is centrosymmetric, the second harmonic of dielectric response to electric field in a real sample is usually not exactly zero. This has been discussed in Refs. [50, 58, 59]. There is a delicate point about the dielectric measurement under electric field. The very first field application may disturb sample's symmetry. The influence of the 2<sup>nd</sup> harmonic on the nonlinear dielectric behavior is easily detectable by Fourier analysis of the polarization signal or, in the case of particularly strong 2<sup>nd</sup> harmonic, by observing asymmetry in the P-E loop. The shape of the energy landscape for contributing polar entities will be affected by any mechanism that leads to the appearance of the second harmonic. For strongly asymmetric poled ferroelectric ceramic and films which exhibit Rayleigh-like behavior [59], although the amplitude of the second harmonic is large and comparable in magnitude to the third harmonic, the phase angle of the third harmonic is not qualitatively disturbed by the 2<sup>nd</sup> harmonic and remains roughly around  $-90^\circ$ . This is due to the fact that the asymmetry ideally changes only the quadrature component of the third harmonic but not the in-phase component, which remains zero. In our BST 6040 samples with macroscopic polarization in paraelectric phase, amplitudes of the second harmonic and the 3<sup>rd</sup> harmonics are close and three orders of magnitude smaller than the amplitude of first harmonic (Figure 6.9). If the analysis is done using Fourier series so that the phase angle of each harmonic can be separated, a relatively small second harmonic does not disturb the observation of the underlying Rayleigh law. We do not think that for the present qualitative analysis it is important to consider effects of the second harmonic as long as the experimental behavior confirms (or disproves) qualitatively one of the models and one knows that the deviation due to 2<sup>nd</sup> harmonic cannot be so large as to bring about confusion between different interpretations.



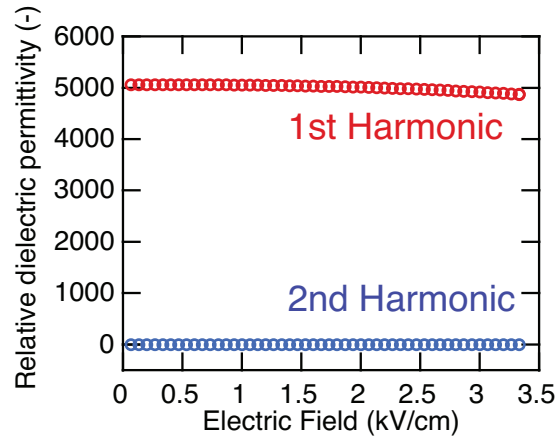


Figure 6.9 1st and 2<sup>nd</sup> harmonic of dielectric permittivity for BST6040 at room temperature.

## 6.6 Summary

In summary, the dependence of the nonlinear dielectric properties on the amplitude of the ac electric field were studied in the paraelectric phase of ferroelectric BST6040 and BTO ceramics. The nonlinear response, with a low hysteresis in the third harmonic over most of the examined field range, is qualitatively different from the one that can be described by a Rayleigh-like mechanism and is similar to that observed in relaxor PMN ceramics. The results presented here do not imply that the nonlinear dynamic behavior of BST6040 at room temperature, BTO above  $T_C$  and of PMN above  $T_{max}$  cannot be described by a domain-wall like dynamics. What these results do show is that the dynamics of polar entities in these materials cannot be well described in its totality by the Rayleigh-like relations that are otherwise valid for description of domain-wall contributions in soft ferroelectrics, such as donor-doped PZT. The nonlinear behavior reported here for the permittivity and  $\delta_3$  can thus serve as a test for validity of models of dynamics of polar entities in the paraelectric phase of ferroelectrics.

## Bibliography

- [1] S. Hashemizadeh and D. Damjanovic, "Nonlinear dynamics of polar regions in paraelectric phase of (Ba<sub>1-x</sub>, Sr<sub>x</sub>) TiO<sub>3</sub> ceramics," *Applied Physics Letters*, vol. 110, p. 192905, 2017.
- [2] K. Rusek, J. Kruczek, K. Szot, D. Rytz, M. Gorny, and K. Roleder, "Non-Linear Properties of BaTiO<sub>3</sub> above T<sub>C</sub>," *Ferroelectrics*, vol. 375, pp. 165-169, 2008.
- [3] J.-H. Ko, T. H. Kim, K. Roleder, D. Rytz, and S. Kojima, "Precursor dynamics in the ferroelectric phase transition of barium titanate single crystals studied by Brillouin light scattering," *Physical Review B*, vol. 84, p. 094123, 2011.
- [4] K. Werner, "Röntgenuntersuchungen über die Seignetteelektrizität von Bariumtitanat," 1951.
- [5] B. Rolov, "ON SOME POSSIBILITIES OF DETERMINING THE VOLUME OF KÄNZIG REGIONS IN FERROELECTRICS," *Le Journal de Physique Colloques*, vol. 33, pp. C2-257-C2-258, 1972.
- [6] G. Burns and F. Dacol, "Crystalline ferroelectrics with glassy polarization behavior," *Physical Review B*, vol. 28, p. 2527, 1983.
- [7] F. Li, S. Zhang, T. Yang, Z. Xu, N. Zhang, G. Liu, *et al.*, "The origin of ultrahigh piezoelectricity in relaxor-ferroelectric solid solution crystals," *Nature Communications*, vol. 7, 2016.
- [8] E. K. Salje, S. Li, M. Stengel, P. Gumbsch, and X. Ding, "Flexoelectricity and the polarity of complex ferroelastic twin patterns," *Physical Review B*, vol. 94, p. 024114, 2016.
- [9] E. K. Salje, M. Alexe, S. Kustov, M. C. Weber, J. Schiemer, G. F. Nataf, *et al.*, "Direct observation of polar tweed in LaAlO<sub>3</sub>," *Scientific reports*, vol. 6, 2016.
- [10] C. Darlington and R. Cernik, "The ferroelectric phase transition in pure and lightly doped barium titanate," *Journal of Physics: Condensed Matter*, vol. 3, p. 4555, 1991.
- [11] G. Smolenskii, V. Isupov, and A. Agranovskaya, "NEW FERROELECTRICS OF COMPLEX COMPOSITION OF THE TYPE A<sub>2</sub>2+ (B<sub>1</sub>3+ B<sub>II</sub>5+) O-6. 1," *SOVIET PHYSICS-SOLID STATE*, vol. 1, pp. 150-151, 1959.
- [12] G. Smolenskii, V. Isupov, A. Agranovskaya, and S. Popov, "Ferroelectrics with diffuse phase transitions," *Soviet Physics-Solid State*, vol. 2, pp. 2584-2594, 1961.
- [13] J. Narvaez and G. Catalan, "Origin of the enhanced flexoelectricity of relaxor ferroelectrics," *Applied Physics Letters*, vol. 104, p. 162903, 2014.
- [14] L. Ganten and S. Trolier-McKinstry, "The field induced e<sub>31</sub>, f piezoelectric and Rayleigh response in barium strontium titanate thin films," *Applied Physics Letters*, vol. 105, p. 132905, 2014.
- [15] L. Ganten, P. Lam, D. Harris, J.-P. Maria, and S. Trolier-McKinstry, "Residual ferroelectricity in barium strontium titanate thin film tunable dielectrics," *Journal of applied physics*, vol. 116, p. 044104, 2014.
- [16] L. M. Ganten and S. Trolier-McKinstry, "Enhanced flexoelectricity through residual ferroelectricity in barium strontium titanate," *Journal of Applied Physics*, vol. 117, p. 094102, 2015.

- [17] A. Biancoli, C. M. Fancher, J. L. Jones, and D. Damjanovic, "Breaking of macroscopic centric symmetry in paraelectric phases of ferroelectric materials and implications for flexoelectricity," *Nature materials*, vol. 14, pp. 224-229, 2015.
- [18] V. Lemanov, E. Smirnova, P. Syrnikov, and E. Tarakanov, "Phase transitions and glasslike behavior in  $\text{Sr}_{1-x}\text{Ba}_x\text{TiO}_3$ ," *Physical Review B*, vol. 54, p. 3151, 1996.
- [19] D. Tenne, A. Soukiassian, M. Zhu, A. Clark, X. Xi, H. Choosuwan, *et al.*, "Raman study of  $\text{Ba}_x\text{Sr}_{1-x}\text{TiO}_3$  films: evidence for the existence of polar nanoregions," *Physical Review B*, vol. 67, p. 012302, 2003.
- [20] A. Biancoli, "Breaking of the macroscopic centric symmetry in  $\text{Ba}_{1-x}\text{Sr}_x\text{TiO}_3$  ceramics and single crystals," 2014.
- [21] L. E. Cross, "Flexoelectric effects: Charge separation in insulating solids subjected to elastic strain gradients," in *Frontiers of Ferroelectricity*, ed: Springer, 2006, pp. 53-63.
- [22] W. Ma and L. E. Cross, "Flexoelectric polarization of barium strontium titanate in the paraelectric state," *Applied Physics Letters*, vol. 81, pp. 3440-3442, 2002.
- [23] I. Ponomareva, A. Tagantsev, and L. Bellaiche, "Finite-temperature flexoelectricity in ferroelectric thin films from first principles," *Physical Review B*, vol. 85, p. 104101, 2012.
- [24] A. Tagantsev, "Piezoelectricity and flexoelectricity in crystalline dielectrics," *Physical Review B*, vol. 34, p. 5883, 1986.
- [25] P. Yudin, R. Ahluwalia, and A. Tagantsev, "Upper bounds for flexoelectric coefficients in ferroelectrics," *Applied Physics Letters*, vol. 104, p. 082913, 2014.
- [26] P. Yudin and A. Tagantsev, "Fundamentals of flexoelectricity in solids," *Nanotechnology*, vol. 24, p. 432001, 2013.
- [27] D. Taylor and D. Damjanovic, "Domain wall pinning contribution to the nonlinear dielectric permittivity in  $\text{Pb}(\text{Zr}, \text{Ti})\text{O}_3$  thin films," *Applied physics letters*, vol. 73, pp. 2045-2047, 1998.
- [28] A. Bokov and Z.-G. Ye, "Recent progress in relaxor ferroelectrics with perovskite structure," in *Frontiers of Ferroelectricity*, ed: Springer, 2006, pp. 31-52.
- [29] A. Glazounov and A. Tagantsev, "Crossover in a non-analytical behaviour of dielectric non-linearity in relaxor ferroelectric," *Journal of Physics: Condensed Matter*, vol. 10, p. 8863, 1998.
- [30] J. Petzelt, D. Nuzhnyy, V. Bovtun, M. Kempa, M. Savinov, S. Kamba, *et al.*, "Lattice dynamics and dielectric spectroscopy of BZT and NBT lead-free perovskite relaxors—comparison with lead-based relaxors," *Phase Transitions*, vol. 88, pp. 320-332, 2015.
- [31] J. Hlinka, "Do we need the ether of polar nanoregions?," *Journal of Advanced Dielectrics*, vol. 2, p. 1241006, 2012.
- [32] L. Rayleigh, "XXV. Notes on electricity and magnetism.—III. On the behaviour of iron and steel under the operation of feeble magnetic forces," *The London, Edinburgh, and Dublin Philosophical Magazine and Journal of Science*, vol. 23, pp. 225-245, 1887.
- [33] L. Néel, "Théorie des lois d'aimantation de Lord Rayleigh. 1ere partie: les déplacements d'une paroi isolée," *Cahiers Phys*, vol. 12, pp. 1-20, 1942.
- [34] D. Damjanovic, "Stress and frequency dependence of the direct piezoelectric effect in ferroelectric ceramics," *Journal of Applied Physics*, vol. 82, pp. 1788-1797, 1997.

- [35] G. Arlt and N. Pertsev, "Force constant and effective mass of 90 domain walls in ferroelectric ceramics," *Journal of Applied Physics*, vol. 70, pp. 2283-2289, 1991.
- [36] S. Li, W. Cao, and L. Cross, "The extrinsic nature of nonlinear behavior observed in lead zirconate titanate ferroelectric ceramic," *Journal of applied physics*, vol. 69, pp. 7219-7224, 1991.
- [37] Q. Zhang, W. Pan, S. Jang, and L. Cross, "Domain wall excitations and their contributions to the weak - signal response of doped lead zirconate titanate ceramics," *Journal of applied physics*, vol. 64, pp. 6445-6451, 1988.
- [38] Q. Zhang, H. Wang, N. Kim, and L. Cross, "Direct evaluation of domain - wall and intrinsic contributions to the dielectric and piezoelectric response and their temperature dependence on lead zirconate - titanate ceramics," *Journal of Applied Physics*, vol. 75, pp. 454-459, 1994.
- [39] D. Berlincourt and H. H. Krueger, "Domain processes in lead titanate zirconate and barium titanate ceramics," *Journal of Applied Physics*, vol. 30, pp. 1804-1810, 1959.
- [40] G. Schmidt, "Zwei Versuche zum elektromechanischen Verhalten von Bariumtitanatkeramik im Curie-Gebiet," *Zeitschrift für Physik*, vol. 148, pp. 314-320, 1957.
- [41] T. Nattermann, Y. Shapir, and I. Vilfan, "Interface pinning and dynamics in random systems," *Physical Review B*, vol. 42, p. 8577, 1990.
- [42] D. Damjanovic, M. Demartin, F. Chu, and N. Setter, "Practical consequences of the extrinsic contributions to the properties of piezoelectric sensors and actuators," in *Applications of Ferroelectrics, 1996. ISAF'96., Proceedings of the Tenth IEEE International Symposium on*, 1996, pp. 251-257.
- [43] D. Damjanovic and M. Demartin, "The Rayleigh law in piezoelectric ceramics," *Journal of Physics D: Applied Physics*, vol. 29, p. 2057, 1996.
- [44] M. Morozov, "Softening and hardening transitions in ferroelectric Pb (Zr, Ti) O<sub>3</sub> ceramics," ÉCOLE POLYTECHNIQUE FÉDÉRALE DE LAUSANNE, 2005.
- [45] M. I. Morozov and D. Damjanovic, "Hardening-softening transition in Fe-doped Pb (Zr, Ti) O<sub>3</sub> ceramics and evolution of the third harmonic of the polarization response," *Journal of Applied Physics*, vol. 104, p. 034107, 2008.
- [46] L. Néel, "Some theoretical aspects of rock-magnetism," *Advances in physics*, vol. 4, pp. 191-243, 1955.
- [47] C. B. DiAntonio, F. A. Williams, and S. M. Pilgrim, "The use of harmonic analysis of the strain response in Pb (Mg/sub 1/3/Nb/sub 2/3/) O/sub 3/-based ceramics to calculate electrostrictive coefficients," *IEEE transactions on ultrasonics, ferroelectrics, and frequency control*, vol. 48, pp. 1532-1538, 2001.
- [48] S. Leary and S. Pilgrim, "Harmonic analysis of the polarization response in Pb (Mg/sub 1/3/Nb/sub 2/3/) O/sub 3/-based ceramics-A study in aging," *IEEE transactions on ultrasonics, ferroelectrics, and frequency control*, vol. 45, pp. 163-169, 1998.
- [49] S. Srilomsak, W. A. Schulze, S. M. Pilgrim, and F. A. Williams, "Harmonic analysis of polarization hysteresis of aged PZTs," *Journal of the American Ceramic Society*, vol. 88, pp. 2121-2125, 2005.
- [50] D. Damjanovic, "Hysteresis in piezoelectric and ferroelectric materials," *The science of hysteresis*, vol. 3, pp. 337-465, 2006.

- [51] M. Tyunina and J. Levoska, "Effect of ac field on the dielectric behavior in epitaxial films of relaxor ferroelectric  $\text{Pb}(\text{Mg}_{1/3}\text{Nb}_{2/3}\text{O}_3)$ ," *Physical Review B*, vol. 72, p. 104112, 2005.
- [52] M. Tyunina and J. Levoska, "The paraelectric state in thin-film  $(\text{Ba}, \text{Sr})\text{TiO}_3$ ," *Journal of applied physics*, vol. 101, p. 084119, 2007.
- [53] L. M. Gerten, "Residual ferroelectricity, piezoelectricity, and flexoelectricity in barium strontium titanate tunable dielectrics," The Pennsylvania State University, 2014.
- [54] A. Tagantsev, V. Sherman, K. Astafiev, J. Venkatesh, and N. Setter, "Erratum: "Ferroelectric Materials for Microwave Tunable Applications" [J. Electroceram. 11, 5 (2003)]," *Journal of Electroceramics*, vol. 14, pp. 199-203, 2005.
- [55] A. Glazounov, A. Tagantsev, and A. Bell, "Evidence for domain-type dynamics in the ergodic phase of the  $\text{Pb}(\text{Mg}_{1/3}\text{Nb}_{2/3}\text{O}_3)$  relaxor ferroelectric," *Physical Review B*, vol. 53, p. 11281, 1996.
- [56] A. Glazounov, "Non-linear dielectric response of  $\text{Pb}(\text{Mg}_{1/3}\text{Nb}_{2/3}\text{O}_3)$  relaxor ferroelectric," 1997.
- [57] A. Tagantsev and A. Glazounov, "Mechanism of polarization response in the ergodic phase of a relaxor ferroelectric," *Physical Review B*, vol. 57, p. 18, 1998.
- [58] J. Dec, W. Kleemann, S. Miga, C. Filipic, A. Levstik, R. Pirc, *et al.*, "Probing polar nanoregions in  $\text{Sr}_{0.61}\text{Ba}_{0.39}\text{Nb}_2\text{O}_6$  via second-harmonic dielectric response," *Physical Review B*, vol. 68, p. 092105, 2003.
- [59] D. V. Taylor, "Dielectric and piezoelectric properties of sol-gel derived  $\text{Pb}(\text{Zr}, \text{Ti})\text{O}_3$  thin films," 1999.



## Chapter 7. Direct observation of polar entities in paraelectric phase of BST6040

### 7.1 Introduction

In the previous chapters we studied symmetry breaking in the paraelectric phase of barium titanate and barium strontium titanate by carrying out pyroelectric, mechanical and thermally stimulated current measurements. All of the mentioned macroscopic studies enabled us to indirectly identify the oriented polar regions as an origin of the symmetry breaking phenomenon. There are many studies in the literature that indirectly observed the local symmetry breaking in ferroelectric perovskites using different techniques such as, X-Ray single crystal structure analysis [1, 2], X-ray diffuse scattering [3-5], X-ray absorption fine structure spectroscopy (XAFS) [6], anomalous birefringence [7], nuclear magnetic resonance spectroscopy (NMR) [8, 9], pulsed soft X-ray laser experiments [10] and electron energy loss spectroscopy (EELS) [11]. Pugachev et al [12] showed that optical second harmonic generation (SHG) experiments on pure BaTiO<sub>3</sub> with no chemical disorder surprisingly exhibit noncentrosymmetric properties up to 900 K, about 200 K more than Burns temperatures where precursors of ferroelectric to paraelectric phase transformation are expected to appear [13, 14]. It was proposed that the origin of the SHG signal is related to clusters of off-centered Ti cations, which are preferably displaced by defects along the eight  $\langle 111 \rangle$  perovskites directions, the ground state of the rhombohedral phase [4, 12, 15].

There are few studies on the direct observation of polar entities in paraelectric phase of ferroelectrics. Tsuda and Tanaka [16] reported in 2016 the first direct observation of polar clusters in the cubic phase of the BaTiO<sub>3</sub> single crystal by Scanning Transmission Electron Microscope-Convergent Beam Electron Diffraction (STEM-CBED). Their data sets obtained from a "defect-free" area of the sample at three different temperatures above  $T_C$  (415, 460 and 600 K) confirm the breaking of the cubic symmetry. They show that the size and fraction of polar clusters decay with increasing the temperature. Interestingly they gave evidence for the existence of a spatially hierarchical structure in the cubic phase of BTO in which, averaging rhombohedral nanometer size clusters shapes tetragonal domains. Also tetragonal domains when averaged over a macroscopic scale form the cubic structure. Burch et al. [17] believed that the presence of what they called remnant ferroelectricity beyond the paraelectric phase transition in BST is associated with the local stoichiometry of the A-site cations. They proposed that the formation of barium rich regions due to the chemical inhomogeneity give rise to the appearance of forbidden polarization in the paraelectric phase. However, their results were not conclusive enough to support their claim. We will see later that Ba-rich regions are probably not the only origin of the polar entities.

To reveal precisely the mechanisms leading to the macroscopic polarization and possibly also to the large flexoelectric effects in ferroelectrics, it is important to understand the exact nature and origin of the local polar regions. Note that origins of the macroscopic polarization and large flexoelectric coefficients do not have to be the same. The aim of this chapter is to search for the direct evidence of polar regions above  $T_C$  and understand their structure and nature by investigating the atomic structure of Ba<sub>0.6</sub>Sr<sub>0.4</sub>TiO<sub>3</sub> (BST6040) ceramics at room temperature using the aberration-corrected scanning transmission electron microscopy (STEM).

## 7.2 STEM investigation of BST6040

Our atomic scale microscopy studies were conducted in collaboration with Interdisciplinary Centre for Electron Microscopy (CIME), Computer Vision Laboratory (CV Lab) from EPFL, Jozef Stefan Institute (JSI) and National Institute of Chemistry from Ljubljana, Slovenia. In CIME, high angle annular dark field scanning transmission electron microscopy (HAADF-STEM) imaging was performed at room temperature on an aberration-corrected FEI Titan-Themis 60-300 operated in scanning mode at an accelerating voltage of 300 kV. This microscope is equipped with a high brightness X-FEG gun and silicon drift Super-X EDX detectors. Series of HAADF-STEM images were acquired with a frame time of 0.5 second along the [001] zone axis on a 45 nm thick BST6040 sample. Drift between the images and scan noise were removed using SmartAlign software. HAADF images were acquired using Tecnai Imaging and Analysis (TIA) software. HAADF images were analyzed by CV Lab to study the atomic structure of BST6040 at room temperature. In Figure 7.1(a) streamlines manifest correlated shifts of A-site atoms (Ba or Sr) from their ideal cubic positions. Figure 7.1(b) and (d) show lattice distortion for both A-site and B-site sublattices respectively. O atoms were not resolvable in this particular image. BST6040 is assumed to possess cubic structure; these graphs show distinct static clusters with average size of few nanometers where A- and B-site atoms are displaced from their ideal cubic positions, similar to what is expected for polar nano regions. Our data also suggest that off centering of Ti in the cubic phase of ferroelectrics, which was believed to be dynamic along  $\langle 111 \rangle$  direction [12], are rather static in these samples. Possibly strain gradients or defects freeze dynamic displacement of Ti in certain directions or these distortions are associated with Ba/Sr variation within the unit cell [18].



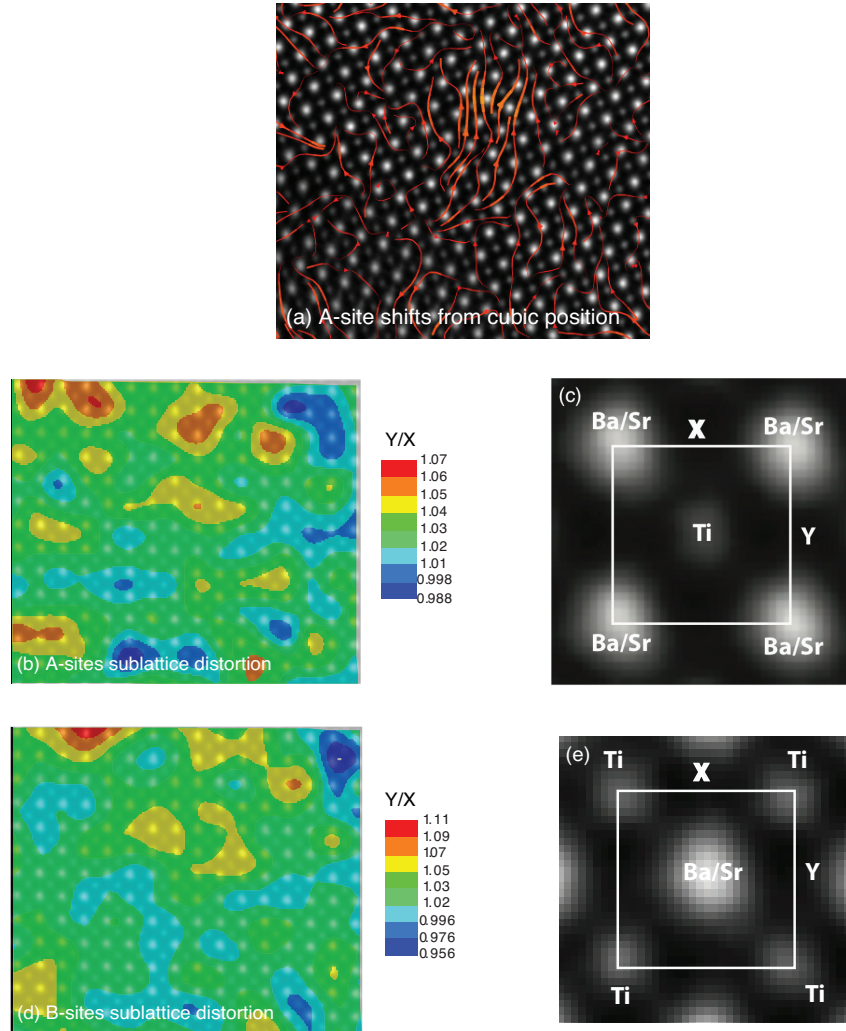


Figure 7.1 (a) HAADF-STEM image of BST6040 along [001] zone axis superimposed with A-site atomic shifts from ideal cubic structure provided by CIME and CV Lab (for original size of image see appendix B); (b) contour map of A-site sublattice distortion; (c) Y and X in A-site sublattice (d) contour map of B-site sublattice distortion; (e) Y and X in B-site sublattice. Figure 7.1 (b) and (d) colors are indication of the degree of departure from cubic structure.

To confirm the polarity of these regions it is essential to show that the gravity centers of positive ( $\text{Ti}^{+4}$ ) and negative ( $\text{O}^{2-}$ ) charges do not coincide with each other and form nonzero dipole moment in the lattice. Just based on Figure 7.1 we cannot study the polarization because O atoms were not resolvable in those images and we have to take into account displacement of O atoms in addition to Ba/Sr and Ti shifts. Moreover, in imaging along [001] zone axis, Ti atomic columns superpose with oxygen columns, which makes the calculation of Ti atoms displacement difficult and inaccurate due to the small difference of Ti and O atomic radiuses. To be able to analyze O

and Ti atoms displacement precisely, [011] zone axis is used to isolate Ti atomic column. Figure 7.2(a) and (b) illustrate BST structure from [001] and [011] zone axes.

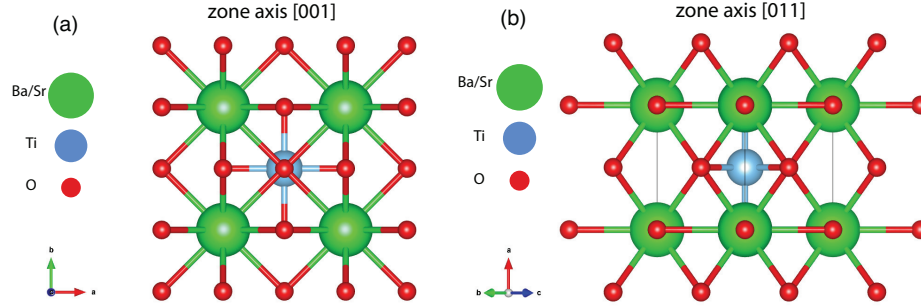


Figure 7.2 (a) BST lattice along [001] zone axis; (b) BST lattice along [011] zone axis.

Imaging along [011] axis has been carried out in collaboration with JSI on a probe Cs-corrected Jeol ARM CF (cold FEG) STEM operated at 200 kV. During analysis of the sample, HAADF and annular bright field (ABF) detectors were used simultaneously. HAADF and ABF images for position determination were taken as a 16-bit stack of 20 images; each frame was taken with pixel time of 1.6  $\mu$ s (2s per frame) using DigiScan STACK Acquisition digital micrograph script written by B. Schaffer. The scan rotation was set so that atom columns were parallel to the scanning direction. The sample drift during stack acquisition was minimized using Stack alignment digital micrograph script written by D.R.G. Mitchell. In HAADF images, atom column intensities depend on the sample thickness and the average atomic number. On the other hand, ABF images are less dependent on the average atomic number and as a result light elements are clearly resolvable in them. Software ImageJ, which was used for position and intensity determination works on images with bright objects on a dark background. As ABF images contain dark spots on bright background ABF images were inverted (negative image) ending with the images similar to HAADF. We refer to them as inverted ABF images. Coordinates of atomic column intensity were determined using 2D Gaussian fit by ImageJ software. The sample thickness of analyzed areas was estimated by electron energy loss spectroscopy (EELS) and was approximately 40 nm. Figure 7.3(a) and (b) present ABF and its inverted images respectively taken along [011] zone axis. As it is illustrated in both images, the atomic positions of A, B and O atoms are clearly visible. It is also seen that the structure of the unit cells is not cubic. Further analyses were performed on Figure 7.3(b). Atomic shifts of Ti and O atoms are calculated with respect to A-site (Figure 7.3(c)) and B-site (Figure 7.3(d)) sublattices. As shown in Figure 7.3(c), (d) and (e), magnitude,  $r$ , and angle,  $\theta$ , of Ti and O atoms displacements from their ideal cubic positions are determined using the following equations:

$$\begin{aligned}
 r &= \sqrt{(x_f - x_c)^2 + (y_f - y_c)^2} \\
 \theta &= \arccos\left(\frac{r}{x_f - x_c}\right) (y_f - y_c > 0) \\
 \theta &= \arccos\left(\frac{r}{x_f - x_c}\right) (y_f - y_c < 0)
 \end{aligned}
 \tag{7.1}$$

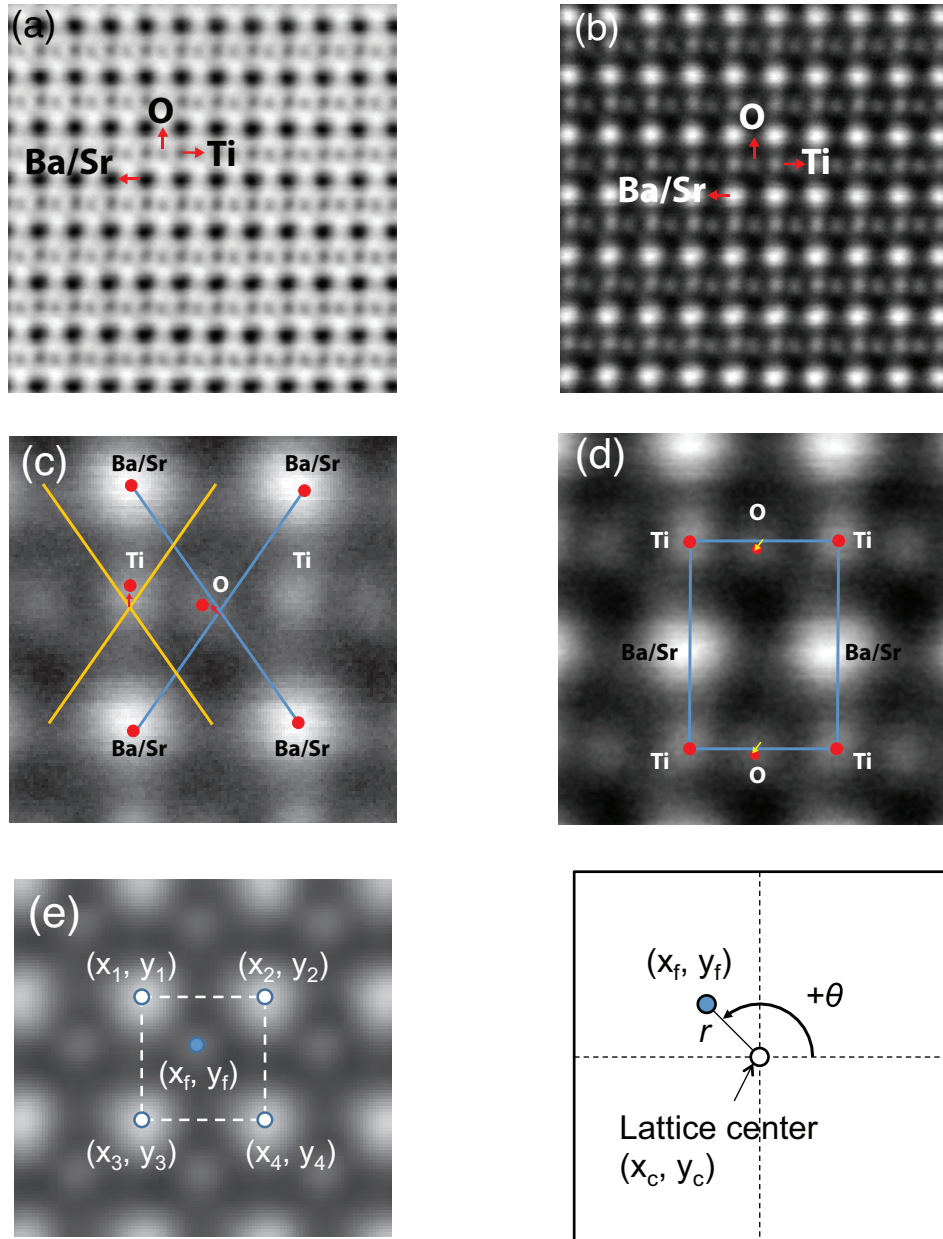


Figure 7.3 (a) ABF image of BST6040 along [011] zone axis; (b) Inverted ABF image; (c) schematic A-site sublattice for O (blue cross) and Ti atoms (yellow cross); and (d) schematic amplitude and angle of atomic shifts from ideal position. Courtesy of Andreja Bencan, JSI and Goran Drazic, NIC

Measured Ti and O atoms displacements regarding both A- and B-site sublattices are presented in Figure 7.4(a), (b) and (c) respectively. The majority of Ti atomic shifts are seem to be oriented in a single direction. To have a non-polar structure, O atoms should be displaced in exactly same direction with the same displacement's magnitude as Ti atoms. However, O atoms

distortions are almost perpendicular to Ti shifts and as a result, our data clearly demonstrate the polar nature of observed clusters.

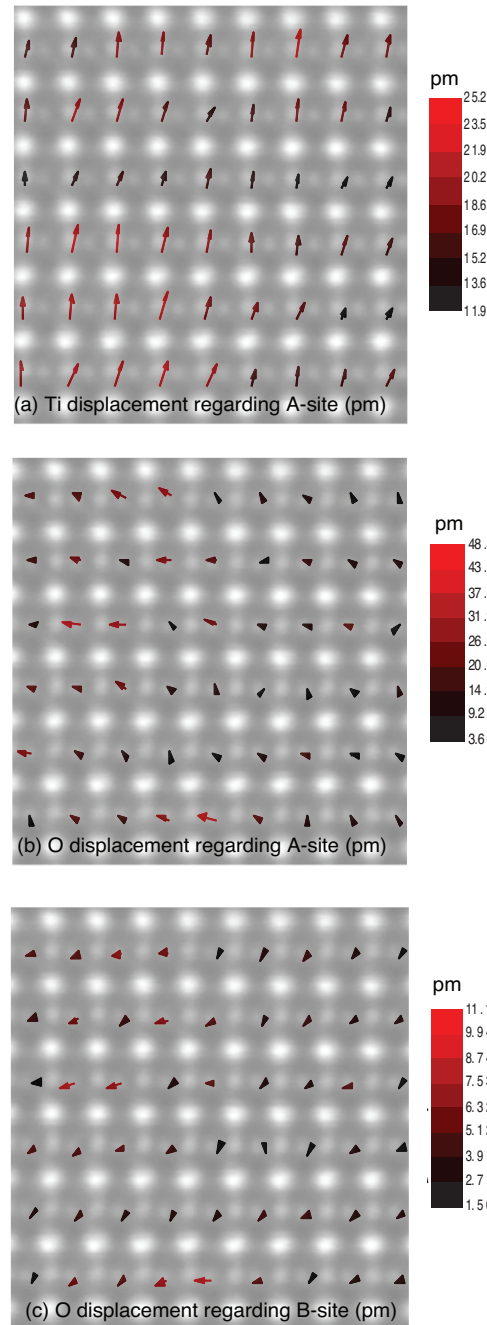


Figure 7.4 (a) Ti displacement regarding A-site sublattice. O displacement (b) regarding A-site and (c) regarding B-site sublattices. Courtesy of Andreja Bencan, JSI and Goran Drazic, NIC

BST compositions with more than 60% of Ba are ferroelectric and have the tetragonal structure at room temperature. One could claim that such clusters are ferroelectric packets with tetragonal distortions inside the paraelectric phase that are formed due to the chemical inhomogeneity of the lattice. If mentioned distortions were related to tetragonal transformation, O and Ti atoms should have shifted along the same axis. Thus, regardless of chemical analysis data and only by considering the directions of Ti and O atomic displacements it's possible to claim that the observed distortion from the cubic phase are not associate with pockets of (Ba,Sr)TiO<sub>3</sub> which are ferroelectric at room temperature. While the structure of the polar regions cannot be determined from the 2D images, it also does not appear to be rhombohedral or orthorhombic.

Atomic scale chemical analysis was performed to investigate the relation of the local stoichiometry of the A-site cations and presence of polar regions. Figure 7.5(a) shows the intensity distribution of Ba/Sr columns. The intensities were normalized to the average column intensity. Comparison between the O displacement contour maps (Figure 7.5(b) and (c)) and the intensity distribution maps suggest that atomic displacements could be associated with the chemical composition (Ba/Sr) fluctuations. However, presence of larger ionic displacement for Sr-rich regions compared to Ba-rich regions is an additional evidence to support that the local polarity does not originate from the chemical inhomogeneity and the crystal structure of ferroelectric (Ba,Sr)TiO<sub>3</sub> pockets in the material. If it were the case, one would expect less distortion from the cubic structure in Sr-rich parts and the tetragonal distortion in Ba-rich regions.

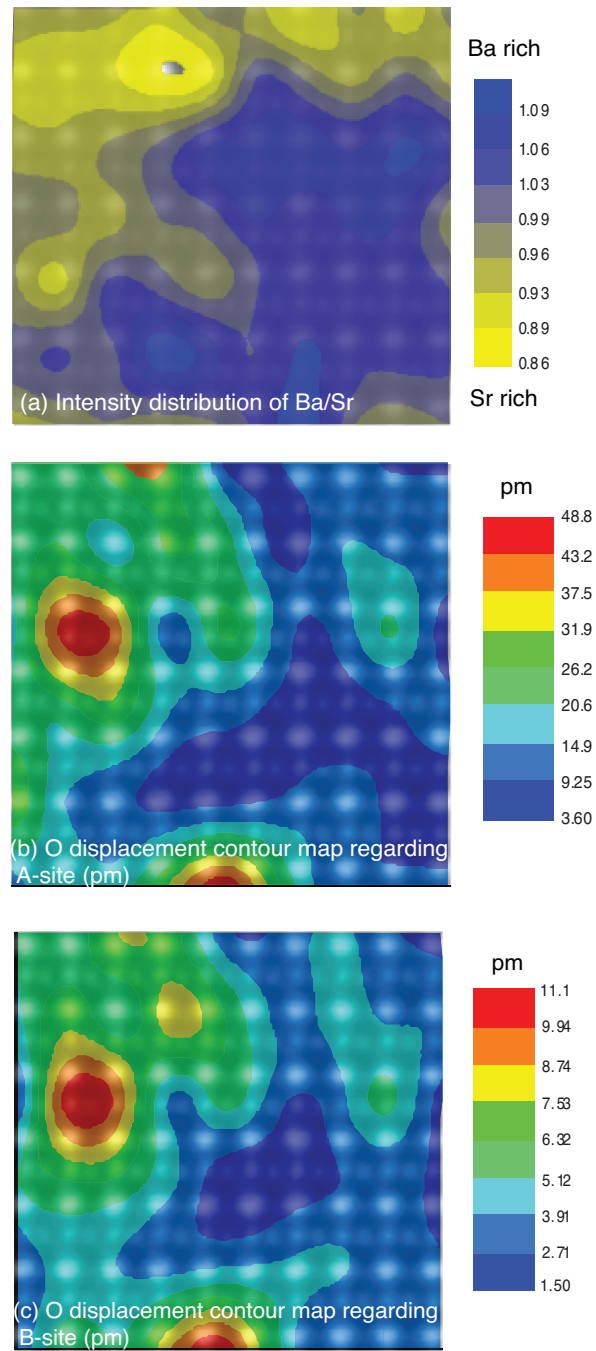


Figure 7.5 (a) Intensity distribution of Ba/Sr in A-site position superposed with its corresponding HAADF images. O displacement contour maps (b) regarding A-site and (c) regarding B-site sublattices. Courtesy of Andreja Bencan, JSI and Goran Drazic, NIC

### 7.3 Summary and conclusion

In summary, in this chapter we have presented results of the search for a direct evidence of the existence of polar regions above the  $T_C$  in ferroelectrics to understand their nature by investigating their atomic structure. Our result reveals the presence of distinct static clusters with the average size of a few nanometers in the lattice where A-site, B-site, and O atoms are displaced from their ideal cubic positions. From the technical point of view, we were able to resolve small shifts of atoms and image columns of O anions, which were used for demonstrating the polar nature of the distorted clusters. Finally, our chemical analysis eliminated the simple case of chemical non-homogeneity and ferroelectric nature of Ba-rich regions as the dominant mechanism for the formation of the polar regions. It is important to mention that the presence of macroscopic polarization cannot be proven from the nano-scale imaging. However our pyroelectric and thermally stimulated current measurement have proven the polar behavior of the samples in the macroscopic scale.



## Bibliography

- [1] K. Itoh, L. Zeng, E. Nakamura, and N. Mishima, "Crystal structure of BaTiO<sub>3</sub> in the cubic phase," *Ferroelectrics*, vol. 63, pp. 29-37, 1985.
- [2] T. Nakatani, A. Yoshiasa, A. Nakatsuka, T. Hiratoko, T. Mashimo, M. Okube, *et al.*, "Variable-temperature single-crystal X-ray diffraction study of tetragonal and cubic perovskite-type barium titanate phases," *Acta Crystallographica Section B: Structural Science, Crystal Engineering and Materials*, vol. 72, pp. 151-159, 2016.
- [3] R. Comes, "Solid State Comm., 6, 715 (1968); M. Lambert and R. Comes," *Solid State Comm*, vol. 7, p. 305, 1969.
- [4] R. Comes, M. Lambert, and A. Guinier, "The chain structure of BaTiO<sub>3</sub> and KNbO<sub>3</sub>," *Solid State Communications*, vol. 6, pp. 715-719, 1968.
- [5] R. Comes, M. Lambert, and A. Guinier, "Désordre linéaire dans les cristaux (cas du silicium, du quartz, et des pérovskites ferroélectriques)," *Acta Crystallographica Section A: Crystal Physics, Diffraction, Theoretical and General Crystallography*, vol. 26, pp. 244-254, 1970.
- [6] B. Ravel, E. Stern, R. Vedrinskii, and V. Kraizman, "Local structure and the phase transitions of BaTiO<sub>3</sub>," *Ferroelectrics*, vol. 206, pp. 407-430, 1998.
- [7] M. Takagi and T. Ishidate, "Anomalous birefringence of cubic BaTiO<sub>3</sub>," *Solid state communications*, vol. 113, pp. 423-426, 2000.
- [8] B. Zalar, V. V. Laguta, and R. Blinc, "NMR evidence for the coexistence of order-disorder and displacive components in barium titanate," *Physical review letters*, vol. 90, p. 037601, 2003.
- [9] B. Zalar, A. Lebar, J. Seliger, R. Blinc, V. V. Laguta, and M. Itoh, "NMR study of disorder in BaTiO<sub>3</sub> and SrTiO<sub>3</sub>," *Physical Review B*, vol. 71, p. 064107, 2005.
- [10] K. Namikawa, M. Kishimoto, K. Nasu, E. Matsushita, R. Tai, K. Sukegawa, *et al.*, "Direct observation of the critical relaxation of polarization clusters in BaTiO<sub>3</sub> using a pulsed x-ray laser technique," *Physical review letters*, vol. 103, p. 197401, 2009.
- [11] M. Bugnet, G. Radtke, S. Y. Woo, G.-z. Zhu, and G. A. Botton, "Temperature-dependent high energy-resolution EELS of ferroelectric and paraelectric BaTiO<sub>3</sub> phases," *Physical Review B*, vol. 93, p. 020102, 2016.
- [12] A. Pugachev, V. Kovalevskii, N. Surovtsev, S. Kojima, S. Prosandeev, I. Raevski, *et al.*, "Broken local symmetry in paraelectric BaTiO<sub>3</sub> proved by second harmonic generation," *Physical review letters*, vol. 108, p. 247601, 2012.
- [13] G. Burns and F. Dacol, "Glassy polarization behavior in ferroelectric compounds Pb(Mg<sub>1/3</sub>Nb<sub>2/3</sub>)O<sub>3</sub> and Pb(Zn<sub>1/3</sub>Nb<sub>2/3</sub>)O<sub>3</sub>," *Solid state communications*, vol. 48, pp. 853-856, 1983.
- [14] G. Burns and F. Dacol, "Crystalline ferroelectrics with glassy polarization behavior," *Physical Review B*, vol. 28, p. 2527, 1983.
- [15] J. Hlinka, T. Ostapchuk, D. Nuzhnyy, J. Petzelt, P. Kuzel, C. Kadlec, *et al.*, "Coexistence of the phonon and relaxation soft modes in the terahertz dielectric response of tetragonal BaTiO<sub>3</sub>," *Physical review letters*, vol. 101, p. 167402, 2008.



- [16] K. Tsuda and M. Tanaka, "Direct observation of the symmetry breaking of the nanometer-scale local structure in the paraelectric cubic phase of BaTiO<sub>3</sub> using convergent-beam electron diffraction," *Applied Physics Express*, vol. 9, p. 071501, 2016.
- [17] M. J. Burch, J. Li, L. Garten, X. Sang, J. Lebeau, S. Trolier-McKinstry, *et al.*, "Investigation of Local A-site Chemistry in Barium Strontium Titanate Using Aberration Corrected STEM, EELS and EDS," *Microscopy and Microanalysis*, vol. 20, pp. 1992-1993, 2014.
- [18] I. Levin, V. Krayzman, and J. C. Woicik, "Local structure in perovskite (Ba, Sr) TiO<sub>3</sub>: Reverse Monte Carlo refinements from multiple measurement techniques," *Physical Review B*, vol. 89, p. 024106, 2014.



## Chapter 8. Conclusions and perspectives

In this thesis, we investigated the origins and mechanism of symmetry breaking in paraelectric phase of BST ferroelectric ceramics (prepared by various processing techniques and conditions). The combination of dielectric, pyroelectric, elastic, thermally stimulated current and atomic resolution imaging studies enabled us to address different aspects of this emergent phenomena. The major experimental remarks of this research are as follows.

### 8.1. Symmetry breaking in hexagonal and cubic polymorphs of $\text{BaTiO}_3$

With the assumption that p- and h-BTO sample preparation with the same starting powder and almost the same sintering conditions results in similar strain gradient and charge defects in the two materials, we were able to isolate and suggest polar nano regions from other possible origins of symmetry breaking such as built-in flexoelectric polarization and inhomogeneous distribution of defects (e.g. ionic charges) [1]. According to our results and knowledge of symmetry of the h- and p-BTO it is possible to state that:

- Paraelectric phase of p-BTO shows local and global breaking of the nominal centrosymmetry and possesses microscopic and macroscopic polarization. These polarizations are likely associated with precursors of the ferroelectric phase known as polar regions. Global polarization of p-BTO could be related to macroscopic ordering of polar regions in this material. In analogy to  $(\text{Ba,Sr})\text{TiO}_3$  solid solution [2], the mechanism governing the alignment of polar regions in p-BTO could be strain gradient. Nevertheless, it is important to mention that Salje [3] has shown that even in absence of external aligning mechanism (such as strain gradient) it is unlikely that a collection of polar entities adopts perfectly random distribution and thus zero global polarization. This aspect should be explored further.
- Hexagonal phase of h-BTO probably contains precursors of the nonpolar paraelectric-ferroelastic phase (elastic "dipoles") and as a result does not possess microscopic and macroscopic polarization. Due to the non-polar nature of the paraelectric-ferroelastic precursors, even if precursors are preferentially oriented, one should not observe macroscopic pyroelectricity; however, TSC measurements have shown that macroscopic centric symmetry is broken in h-BTO. The origin of this symmetry breaking is still unknown. But, strain gradient could explain the symmetry breaking in h-BTO.
- Ferroelastic regions are elastically active in hexagonal h-BTO, while polar regions are both electrically and elastically mobile in the paraelectric phase of p-BTO.

We claim that all presented experimental results can be consistently explained by the strain gradient and its interaction with microscopic precursors of the ferroic states of two materials. The evidence of such gradient has been presented before for BST6040, and should be studied in a systematic fashion for other materials.

## 8.2 Origins of the symmetry breaking in (Ba,Sr)TiO<sub>3</sub> system

We have investigated effects of processing conditions, grain size and point defect concentration on evolution of forbidden pyroelectric response above Curie temperature for BST6040. Our results suggest that:

- The presence of polar behavior in BST6040 sample even after minimizing both gravitational and thermal gradient effects by continuous rotation of the sample during sintering excludes simple case of gravity or direction of thermal exposure as the possible origins of the symmetry breaking.
- Decreasing the amplitude of pyroelectric current density by reducing the grain size and dielectric permittivity in BST6040 could suggest that the magnitude of polarization in a polar cluster is reduced by the grain size effect. Nevertheless, Biancoli [4] did not observe same relation between grain size and pyroelectric current amplitude. Considering his result and the fact that different mechanisms could be responsible for magnitudes of dielectric permittivity and pyroelectric current, we can state that although the grain size could change the magnitude of pyroelectric current it is not the dominant mechanism governing the symmetry breaking.
- Suppression of the pyroelectric response in the BST6040 samples with higher concentration of point defects supports the idea that point defects are not the principal charged entities responsible for the symmetry breaking. If it was the case we would observe a larger response for doped and nonstoichiometric samples. The most likely origin of the global symmetry breaking is thus alignment of polar regions. The defects, such as oxygen vacancies, most likely break coherence of polarization within polar regions and thus reduce their polar response and consequently the global polarization.
- Presence of macroscopic symmetry breaking in BST samples prepared with very different powders and different sintering and densification techniques and also its presence in other compositions, such as  $\text{Pb}(\text{Mg}_{1/3}\text{Nb}_{2/3})\text{O}_3$  ceramics and single crystals of  $\text{K}(\text{Ta,Nb})\text{O}_3$  [2], indicate that the symmetry breaking in paraelectric phase of ferroelectrics is a general effect and it is not limited to one specific material or preparation procedure and is generally encountered in perovskite materials and broader. A systematic effort should be applied in investigating factors may reduce the polar response in nominally nonpolar phases.

## 8.3 Nonlinear behavior of polar entities in BST system

We studied the field dependence of the first harmonic of the amplitude and the third harmonic of the phase angle of the dielectric permittivity to identify mechanisms governing the dielectric nonlinearity in the BST system. Such information can directly reveal wheather nonlinear contributions exhibit hysteretic character or not. This is essential in clarifying mechanisms of the dynamics of polar regions. For example, evolution of the phase angle with the field is important to test for the presence of the Rayleigh-like (domain-wall-like) dynamics. The following are the remarks on the results of the dielectric nonlinear experiments carried out for BST system:

- For BST6040 samples, at weak fields, where polarization response is dominated by the contribution of polar entities, the permittivity usually increases with respect to the field amplitude, for example by "breathing" of polar regions. Thus, the initial increase of the permittivity with increasing field in our samples suggests presence of some kind of electrically active polar entities above the Curie temperature. The DMA measurements also suggest that they are elastically active.
- At higher fields, permittivity decrease with increasing the electric field for BST6040 samples, two mechanisms could explain this behavior: (i)"tunability" of the permittivity [5] and (ii) reorientation of polar entities followed by saturation of their response at high fields. We suggest that the observed evolution of the permittivity is most likely due to the saturation of the response of polar regions, which in saturated state no longer contribute to the dynamic permittivity.
- For BST6040 samples, the phase angle of 3<sup>rd</sup> harmonic globally approaches either  $\approx 0^\circ$  or  $\approx -180^\circ$ , meaning that the material response is anhysteretic and the amplitude of the out of phase component of the nonlinear polarization for this harmonic is close to zero. These effects agree well with the trend in the permittivity that increases at first and then decreases when  $\delta_3$  shifts towards zero with increasing field amplitude.
- In BST system, the Curie phase transition temperature shifts to lower temperatures by decreasing the barium content. At room temperature intensity and coupling effect of polar entities is expected to be less in compositions with a lower  $T_C$ . We observed that the nonlinearity decreases with increasing Sr content to the point that BST1090 response is similar to that of  $\text{SrTiO}_3$ . Transition of the phase angle from  $-180^\circ$  to  $0^\circ$  (both indicating an anhysteretic nonlinearity) is shifted to higher fields by decreasing the concentration and polarization strength of polar entities. We assume here that concentration and strength of polar entities decreases as temperature increases above the  $T_C$ , as suggested in ref [6] by Burns.
- Above  $T_C$  pure  $\text{BaTiO}_3$  samples exhibit nonlinear permittivity that increases with increasing field and the  $\delta_3$  rapidly evolves from  $\sim -180^\circ$  toward  $\sim 0^\circ$  at weak fields and then shows tendency to stabilize toward  $0^\circ$  at large fields similar to BST6040 and PMN. This suggests that the dynamic nonlinear behavior in BST is not solely due to the chemical inhomogeneity.
- Rayleigh equation, which describes dynamics of domain walls in a random pinning environment, requires  $\delta_3$  be close to  $-90^\circ$  is neither able to predict the evolution of the  $\delta_3$  nor the permittivity with the field amplitude. This behavior is similar to that previously suggested for PMN [7] and confirmed experimentally here.

These results suggest that the dynamics of polar entities in investigated materials cannot be well described by the domain-wall dynamics in a random system (Rayleigh-like relations that are otherwise valid for description of domain-wall contributions in soft ferroelectrics, such as donor-doped PZT).

## 8.4 Direct observation of polar entities in paraelectric phase of BST6040

The aberration-corrected scanning transmission electron microscopy (STEM) was used to search for a direct evidence of polar regions above the  $T_C$  and understand their structure and nature. We investigated the atomic structure of BST6040 ceramics at room temperature ( $T_C=273$  K).

- Imaging along [001] zone axis showed distinct static clusters with average size of few nanometers where A-site, B-site and O atoms are displaced from their ideal cubic positions (similar to what is expected for polar nano regions). Our data also suggest that off centering of Ti in cubic phase, which was proposed to be dynamic along  $\langle 111 \rangle$  direction [8], are practically static in our samples. It is possible that strain gradients or defects freeze dynamic displacement of Ti in a preferred direction. Alternatively, these distortions from the ideal cubic positions may be associated with Ba/Sr variation within the unit cell [9], which can also be biased through the sample by a strain gradient.
- Imaging along [011] zone axis helped us to confirm the polarity of observed clusters. Studying Ti and O atoms displacements regarding both A- and B-site sublattices illustrate that majority of Ti atomic shifts are seem to be oriented in one direction, O atoms distortions are almost perpendicular to Ti shifts. As a result our data clearly demonstrate that the gravity centers of positive ( $Ti^{+4}$ ) and negative ( $O^{-2}$ ) charges do not coincide with each other and form nonzero dipole moment in the lattice. This should be made quantitative in the future.
- Atomic scale chemical analysis was carried out to investigate the relation of local stoichiometry of A-site cations and polarity. Distribution maps suggest that atomic displacements could be associated with chemical composition (Ba/Sr) fluctuations. However, the presence of larger ionic displacement for Sr-rich regions compared to Ba-rich regions is an additional evidence to support that the local polarity does not originate only from the chemical inhomogeneity and the crystal structure of Ba-rich ferroelectric (Ba,Sr)TiO<sub>3</sub> pockets in the material. If it was the case, one would expect less distortion from the cubic structure in Sr-rich parts and tetragonal distortion in Ba-rich regions; this does not happen. All distorted regions possess symmetry, which is lower than rhombohedral, and in some cases distortions are larger in Sr-rich compositions.

## 8.5 Suggestions for future work

Based on the result of this thesis, several issues related to the mechanisms governing the symmetry breaking of perovskite oxides above their  $T_C$  can be identified as open. They are listed here:

- Williamson-Hall analysis of the X-ray diffraction (XRD) data showed presence of non-uniform microstrain across the sample thickness in BST6040, possibly developed by the small thermal gradient during the sintering [2]. We mentioned that this strain gradient could be the mechanism governing the alignment of polar regions. However, details of such alignment are not clear yet. We suggest performing 3D mapping of the strain within the samples using hard X-ray microscopy to correlate processing conditions and strain distribution in the material.
- We were not able to identify the exact driving force for retention of hexagonal phase of BTO at room temperature because no significant structural difference (i.e., presence of twins) was observed between the milled and unmilled powders. It's possible that the chosen grains for TEM study were the same in both powders. Studying more grains is needed to identify any possible structural difference. In addition, there are nano-sized grains containing Zr in the milled powder, which are absent in the non-milled powder. Zr is introduced during milling step by Zr milling balls. Milling BTO powders with alumina balls will be helpful to study any possible effect of Zr on retention of hexagonal phase at room temperature.
- More investigation is needed to study the mechanism of macroscopic symmetry breaking observed by thermally stimulated current in hexagonal barium titanate. In addition, atomic resolution study of h-BTO would be helpful to answer the question on hypothetical polarity of ferroelastic regions in hexagonal BTO.
- Based on our results, the mechanism of the negative dielectric nonlinearity at high electric fields in these systems is still unknown. It could be associated with the tunability and/or saturation of polar regions. Carrying out dielectric the nonlinear measurement as a function of frequency would enable us to address the origin of decreasing dielectric permittivity with the applied electric field.
- The appearance of forbidden polarization due to the chemical inhomogeneity in A-site of BST samples is still subject of debate in scientific community. Although our results support the idea that the local polarity does not originate only from the chemical inhomogeneity, atomic resolution study of pure BaTiO<sub>3</sub> above its Curie temperature would be helpful to address this issue.

## Bibliography

- [1] S. Hashemizadeh, A. Biancoli, and D. Damjanovic, "Symmetry breaking in hexagonal and cubic polymorphs of BaTiO<sub>3</sub>," *Journal of Applied Physics*, vol. 119, p. 094105, 2016.
- [2] A. Biancoli, C. M. Fancher, J. L. Jones, and D. Damjanovic, "Breaking of macroscopic centric symmetry in paraelectric phases of ferroelectric materials and implications for flexoelectricity," *Nature materials*, vol. 14, pp. 224-229, 2015.
- [3] E. K. Salje, S. Li, M. Stengel, P. Gumbsch, and X. Ding, "Flexoelectricity and the polarity of complex ferroelastic twin patterns," *Physical Review B*, vol. 94, p. 024114, 2016.
- [4] A. Biancoli, "Breaking of the macroscopic centric symmetry in Ba<sub>1-x</sub>Sr<sub>x</sub>TiO<sub>3</sub> ceramics and single crystals," 2014.
- [5] A. Tagantsev, V. Sherman, K. Astafiev, J. Venkatesh, and N. Setter, "Erratum: "Ferroelectric Materials for Microwave Tunable Applications" [J. Electroceram. 11, 5 (2003)]," *Journal of Electroceramics*, vol. 14, pp. 199-203, 2005.
- [6] G. Burns and F. Dacol, "Crystalline ferroelectrics with glassy polarization behavior," *Physical Review B*, vol. 28, p. 2527, 1983.
- [7] A. Glazounov and A. Tagantsev, "Crossover in a non-analytical behaviour of dielectric non-linearity in relaxor ferroelectric," *Journal of Physics: Condensed Matter*, vol. 10, p. 8863, 1998.
- [8] A. Pugachev, V. Kovalevskii, N. Surovtsev, S. Kojima, S. Prosandeev, I. Raevski, *et al.*, "Broken local symmetry in paraelectric BaTiO<sub>3</sub> proved by second harmonic generation," *Physical review letters*, vol. 108, p. 247601, 2012.
- [9] I. Levin, V. Krayzman, and J. C. Woicik, "Local structure in perovskite (Ba, Sr) TiO<sub>3</sub>: Reverse Monte Carlo refinements from multiple measurement techniques," *Physical Review B*, vol. 89, p. 024106, 2014.



## Appendix A. Symmetry elements and point groups

There are four types of macroscopic symmetry elements in crystals: center of symmetry, mirror plane, 1-, 2-, 3-, 4- or 6-fold rotation axes, and 1-, 2-, 3-, 4- or 6-fold inversion axes. The possible combinations of these symmetry elements are called point groups. Crystals are grouped into 32 crystal classes and seven crystal systems according to their point group. These seven crystal systems are: triclinic, monoclinic, orthorhombic, tetragonal, cubic, trigonal and hexagonal. Symmetry of polycrystalline and amorphous materials can be described by seven Curie group symmetries. They all have an  $\infty$ -fold rotation axis in common. Geometrically these groups are represented as spheres, cylinders and cones, with or without handedness. Table 1 and Table 2 shows 32 crystal classes and Curie groups respectively.

Table 1. Crystal systems and their crystal classes

Crystal system	Crystal class
Triclinic	$1, \bar{1}$
Monoclinic	$2, m, 2/m$
Orthorhombic	$222, mm2, mmm$
Trigonal	$3, \bar{3}, 32, 3m, \bar{3}m$
Tetragonal	$4, \bar{4}, 4/m, 422, 4mm, \bar{4}2m, 4/mmm$
Hexagonal	$6, \bar{6}, 6/m, 622, 6mm, \bar{6}m2, 6/mmm$
Cubic	$23, m\bar{3}, 432, \bar{4}3m, m\bar{3}m$

Table 2. Crystal systems and their crystal classes

Curie group	Symmetry operator
$\infty$	$\infty \parallel Z_3$
$\infty m$	$\infty \parallel Z_3, m \perp Z_1$
$\infty 2$	$\infty \parallel Z_3, 2 \parallel Z_1$
$\infty/m$	$\infty \parallel Z_3, m \perp Z_3$
$\infty/mmm$	$\infty \parallel Z_3, m \perp Z_3, m \perp Z_1$
$\infty\infty$	$\infty \parallel Z_3, \infty \parallel Z_1$
$\infty\infty m$	$\infty \parallel Z_3, \infty \parallel Z_1, m \perp Z_1$

## Appendix B. HAADF-STEM image of $\text{Ba}_{0.6}\text{Sr}_{0.4}\text{TiO}_3$

Streamlines show correlated shifts of A-site atoms (Ba or Sr) from their ideal cubic positions. Image 7.1(a) is cut from this image.



Figure 1 HAADF-STEM image of BST6040 along [001] zone axis superimposed with A-site atomic shifts from ideal cubic structure.

## Appendix C. XRD patterns for h-BTO, p-BTO and BST6040

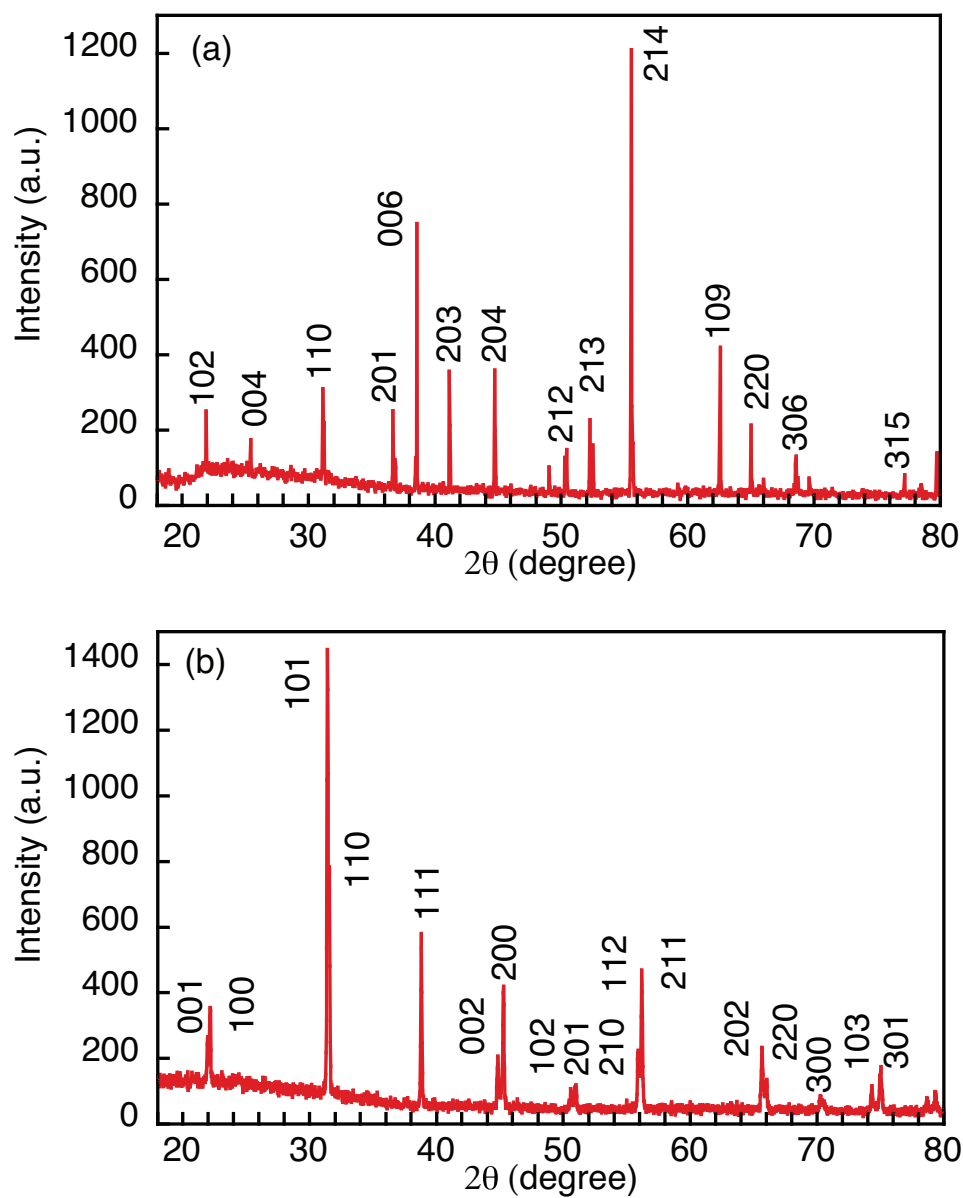


Figure 1 XRD patterns for a) h-BTO and b) p-BTO.

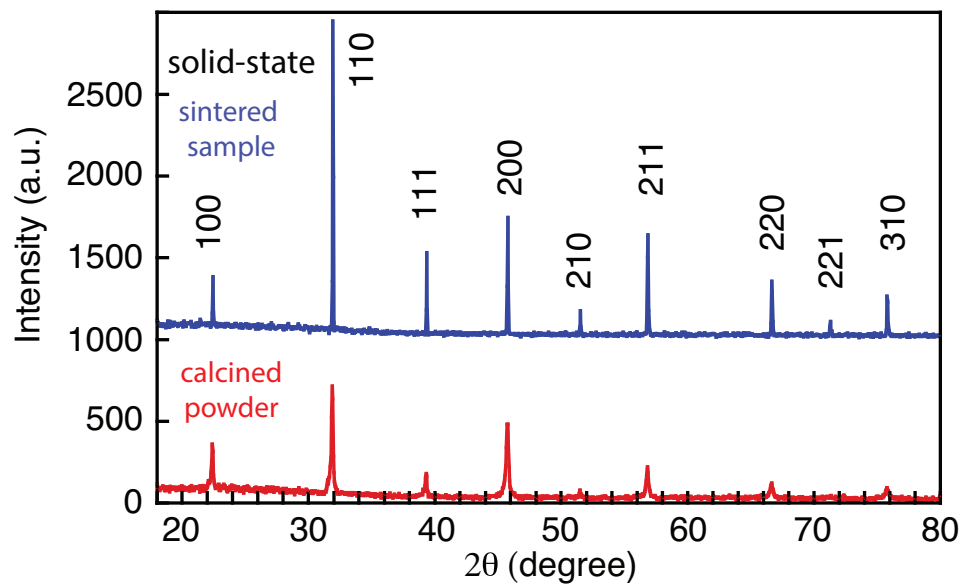


Figure 2 XRD spectra on the solid-state derived calcined powder and sintered sample of BST6040.

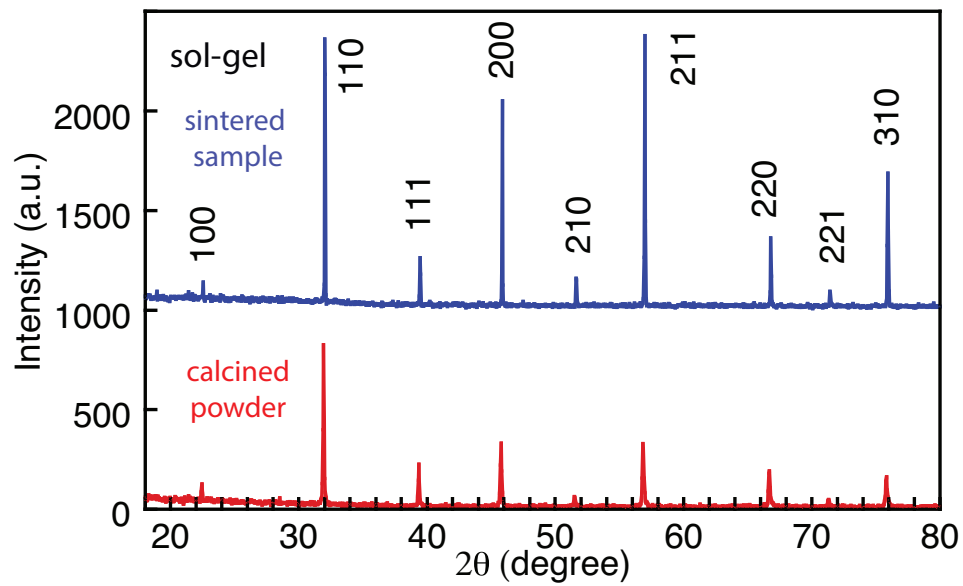


Figure 3 XRD spectra on the sol-gel derived calcined powder and sintered sample of BST6040.

## Curriculum vitae

Sina Hashemi Zadeh  
Avenue des figuiers 20  
1007 Lausanne, Switzerland  
E-mail: Sina.hashemizadeh@gmail.com  
Date of Birth: 24.07.1987

---

### Education

- Ecole Polytechnique Fédérale de Lausanne (EPFL) Aug. 2013-Aug. 2017  
Doctoral Assistant in Materials science and materials engineering  
PhD Thesis: Origins of the macroscopic symmetry breaking in centrosymmetric phases of perovskite oxides
  - Georgia Institute of Technology, Atlanta Sep. 2012-May 2013  
(George W. Woodruff School of Mechanical Engineering)  
Master Project: Flexoelectricity in patterned dielectric thin films
  - Ecole Polytechnique Fédérale de Lausanne (EPFL) Sep. 2010-Jul. 2012  
Masters in Material Science and Engineering  
Orientation: materials for microelectronics and micro engineering
  - University of Tehran, Faculty of Engineering Sep. 2005-Feb. 2010  
Bachelor of Science in Metallurgy and Materials Engineering
- 

### Publications

- S. Hashemizadeh and D. Damjanovic, "Nonlinear dynamics of polar regions in paraelectric phase of  $(\text{Ba}_{1-x}, \text{Sr}_x)\text{TiO}_3$  ceramics," *Applied Physics Letters*, vol. 110, p. 192905, 2017.
- S. Hashemizadeh, A. Biancoli, and D. Damjanovic. "Symmetry breaking in hexagonal and cubic polymorphs of  $\text{BaTiO}_3$ ," *Journal of Applied Physics*, 119.9 2016.
- M. Pourmajidian, R. Mahmudi, A. R. Geranmayeh, S. Hashemizadeh, and S. Gorgannejad. "Effect of Zn and Sb Additions on the Impression Creep Behavior of Lead-Free Sn-3.5Ag Solder Alloy" *Journal of ELECTRONIC MATERIALS*, Vol. 45, No. 1, 2016.
- R. Mahmudi, M. Pourmajidian, A.R. Geranmayeh, S. Gorgannejad, S. Hashemizadeh "Indentation creep of lead-free Sn-3.5Ag solder alloy: Effects of cooling rate and Zn/Sb addition" *Materials Science & Engineering A* 565 (2013) 236–242.

### Conference presentations

- “Origin of the macroscopic symmetry breaking in centrosymmetric phase of perovskite  $\text{BaTiO}_3$ ”, oral presentation, Electroceramics XV Conference, June 27-29, 2016 Limoges, France.
  - “Broken symmetry in paraelectric phase and polar nano regions”, oral presentation, Joint ISAF/ECAPD/PFM Conference, August 21-25, 2016 Darmstadt, Germany.
  - “Symmetry breaking and direct evidence of polar regions in paraelectric phase of  $\text{BaTiO}_3$ -based ferroelectrics”, oral presentation, Joint IEEE ISAF-IWATMD-PFM Conference, May 7-11, 2017, Atlanta, USA.
- 

### Computer skills

- Mathematica, LabView, AutoCAD, Illustrator, Microsoft office, Kaleidagraph
- 

### Honors and Awards

- Best poster award of ferroelectric workshop 2015 Leysin, Switzerland
  - Awarded IEEE travel grant for ISAF Conference 2016 in Darmstadt and 2017 in Atlanta
- 

### Language skills

- Persian: Mother tongue
- English: C2-Fluent, both speaking and writing
- French: B1-Intermediate

